Asymmetries in the decay of beauty

CERN-THESIS-2010-048
23/02/2010

Gabriël Ybeles Smit

Cover: ”Do physicists dream of magnetic penguins?” - by the author.
ISBN: 978-90-9025082-3
Printed by Ipskamp Drukkers.
Copyleft 2009 by G.V. Ybeles Smit. All rights reversed.

This work is part of the research programme of the ’Stichting voor Fundamenteel Onderzoek der Materie (FOM)’, which is financially supported by the ’Nederlandse Organisatie voor Wetenschappelijk Onderzoek (NWO)’

VRIJE UNIVERSITEIT

Asymmetries in the decay of beauty

ACADEMISCH PROEFSCHRIFT

ter verkrijging van de graad Doctor aan
de Vrije Universiteit Amsterdam,
op gezag van de rector magnificus
prof.dr. L.M. Bouter,
in het openbaar te verdedigen
ten overstaan van de promotiecommissie
van de faculteit der Exacte Wetenschappen
op dinsdag 23 februari 2010 om 13.45 uur
in de aula van de universiteit,
De Boelelaan 1105

door

Gabriël Valentijn Ybeles Smit

geboren te Amsterdam

promotoren:	prof.dr. M.H.M. Merk
	prof.dr.ing. J.F.J. van den Brand
copromotor:	dr. H.J. Bulten

C'è un'ape che se posa
su un bottone de rosa:
lo succhia e se ne va...
Tutto sommato, la felicità
è una piccola cosa

–Trilussa

Contents

Introduction

The advent of a relativistic quantum theory led Dirac in 1928 to the prediction of positive and negative energy states of the same elementary particle. When the antiparticle of the electron was indeed discovered in 1932 by Anderson, this was the first success of Diracs theory and the existence of antimatter had been verified.

When quantum field theory was developed as a relativistic quantum theory, it predicts, like Diracs theory, an equal amount of matter and antimatter when they are created from the vacuum. The discovery of more elementary particles led to the so-called standard model of particle physics. It made it clear that antiparticles are always produced in equal abundance of normal matter particles. However in the universe nearly only matter is observed. This apparent asymmetry is still one of the unsolved questions in present day particle physics.

Matter and antimatter are related by CP symmetry. Research by Cronin and Fitch led to the discovery in 1964 of CP violation in the Kaon system. Kaons contain a s-quark, they decay via the weak interaction to stable particles. A quark similar to the s-quark with a higher mass was found in 1977 at Fermilab, the b-quark. Mesons that contain a b-quark were found to also exibit violation of CP symmetry in several experiments, like Babar and Belle.

The standard model incorporates CP violation and has been very successful to explain almost all the experimental evidence in the quark sector. However, to explain the huge asymmetry between matter and antimatter in the visible universe, has to date not been possible. This is one reason to look for so-called new physics or physics beyond the standard model.

The fact that the mesons containing a b-quark are heavy compared to the binding energy can also be exploited to search for effects that occur relatively rarely. Theoretical models can be better understood in non-relativistic systems. Rare decays of B mesons involve heavy particles in quantum loops. New heavy particles can therefore be probed.

The LHCb experiment at the LHC collider in Geneva, Switzerland will measure CP violation with B-hadrons and explore rare decays of B mesons. At LHCb a yearly amount of 10^{12} $b\bar{b}$ pairs will be produced.

This thesis describes the search for new physics in the relatively rare decay $B^0 \to K^*\mu^+\mu^-$. The first chapter (1) describes the theory for the weak interaction and rare decays in the standard model. The observables for the decay $B^0 \to K^*\mu^+\mu^-$ are introduced. An angular analysis of the muons gives an asymmetry of events with a forward- or backward-going muon (A_{FB}) which depends on the dimuon invariant mass. The principle of detecting physics beyond the standard model with this forward-backward asymmetry is given in the last part of the chapter.

A description of the LHCb experiment and the accelerator facilities is given in chapter 2. The LHCb spectrometer, all its subdetectors, the trigger and the data acquisition system are described.

Chapter 3 provides an overview of the software framework in which the simulations and analyses described in this thesis are performed. Starting from the software framework, several auxiliary software parts are specified. After this the event data model and the tracking model are given. The event generation is described next, the detector simulation is briefly touched upon and the digitisation of the signals is mentioned. The software utilised for track reconstruction will be described next. It includes the reconstruction and fitting of tracks. Lastly a brief description of the physics analysis software is given.

The subject of chapter 4 is a pattern recognition algorithm that was written to provide tracks in a particular part of the LHCb spectrometer. The performance of the algorithm is subsequently investigated and the results are given in the last sections of this chapter.

For the analysis of the rare decay channel the selection of the experimental data is described in chapter 5. The selection steps used to obtain the event samples used to analyse the rare decay are given together with the projected annual event yields of signal and background events.

In chapter 6 the results are given of an investigation of the systematic effects of the selection steps. Effects are investigated in the observables and the forward-backward asymmetry. Also the effects on the distributions of a background sample are investigated.

An unbinned counting analysis of the decay products of the decay channel $B^0 \to K^*\mu^+\mu^-$ is performed and the results are given in chapter 7. The unbinned fit is compared to a traditional binned method. A robustness test on the fit methods is performed with Monte Carlo events. The stability and robustness of the fitting methods is tested. At last a sensitivity estimate for the LHCb experiment is extracted for several more realistic scenarios including background events. Henceforth a correction method for the background is applied. In the last section a sensitivity estimate for the asymmetry is given for a sample size equivalent to 1 year of events for the standard model and a new physics model.

1

Theory

The study of flavour-changing neutral interactions through rare decays yields observables sensitive to possible manifestations of physics beyond the standard model. The topic of interest in this thesis is the rare decay $B^0 \to K^{*0}\mu^+\mu^-$, which proceeds through a flavour-changing neutral interaction.

The theoretical motivation for this study as well as the analysis techniques are presented here. The analysis focusses on the angular distribution of the two final state muons in this flavour-changing neutral decay.

The motivation is presented in the first part of the chapter for the search for interactions that are not described by the standard model. Thereafter the effective theory for studying rare B-decays is outlined. This will lead to the description of observables that are of interest for the decay channel studied in this thesis.

The chapter will conclude with a definition of the forward-backward asymmetry of the muons and with theoretical predictions for this asymmetry in the standard model and some classes of supersymmetric models. These physics models have been implemented in the LHCb event generator software and from the simulated event distributions forward-backward asymmetries are made which are described at the end of this chapter.

1.1 Weak interaction

The flavour-changing weak interaction maximally violates parity [1]. This interaction is described by electroweak gauge theory, where it is mediated by the exchange of W gauge bosons. The coupling is purely described with a left-handed $V - A$ (vector minus axial vector) Lorentz structure. Violation of symmetries like parity hence affect the fundamental nature of interactions. Beside parity there are two more discrete symmetries that are important within a quantum field theory: Charge conjugation and time reversal.

1.1.1 Symmetries

If a physical system is invariant under a certain operation, this operation is called a symmetry of the system. In particle physics one can distinguish three fundamental discrete symmetry operators that are important to the standard model: C, P and T. The charge conjugation operator, C interchanges particles for antiparticles ($C\phi \rightarrow \bar{\phi}$). The parity operator P, reflects space points in the origin (for a Lorentz vector: $P(\vec{x}, t) \rightarrow (-\vec{x}, t)$). The time reversal operator, T, inverts the time co-ordinate ($T(\vec{x}, t) \rightarrow (\vec{x}, -t)$). In the standard model C and P are maximally broken as can be seen from the absence of a right-handed neutrino. The combined CP operation is related to the difference between matter and antimatter. Finally, CPT appears to be conserved and its violation would imply breaking of Lorentz invariance. The breaking of combined C and CP symmetries plays a fundamental role in the existence of a matter dominated universe.

1.1.2 Baryon asymmetry

One of the unsolved problems in contemporary physics is the existence of the baryon asymmetry in the universe. Locally a surplus of baryonic matter over antimatter is observed [2]. Also on a larger scale there is no evidence for amounts of antimatter consistent with primordial production [3]. From measurements of the cosmic microwave background (CMB) [4] an estimate can be made of the baryon asymmetry in the early universe. From primordial element abundances one can also estimate the fraction of baryons to photons [5]. Both methods yield an asymmetry of the number densities of baryons (n_B) and anti-bayons ($n_{\bar{B}}$) normalised to the photon number density n_γ of

$$\eta = \frac{n_B - n_{\bar{B}}}{n_\gamma} \sim 10^{-10}. \tag{1.1}$$

Sakharov showed [6] that for baryogenesis to take place, at least three conditions are necessary. First, baryon number should not be conserved. Second, C and CP symmetries should be violated. Last, baryogenesis should take place away from thermal equilibrium.

The standard model electroweak transition accomodates for all of the conditions, however not in sufficient amounts to explain the observed asymmetry[1]. This gives an incentive to search for processes beyond the standard model.

1.1.3 Flavour changing interactions

The standard model electroweak Lagrangian describes the electroweak interaction of fundamental fermions. It can be split as follows,

$$\mathcal{L}_{EW} = \mathcal{L}_D + \mathcal{L}_G + \mathcal{L}_H + \mathcal{L}_Y. \tag{1.2}$$

The free fermion fields are described by the Dirac lagrangian $\mathcal{L}_D$. The Dirac Lagrangian incorporates the SM gauge symmetry to Dirac particles and as such describes

[1]Calculated [7] to be around 10^{-18}.

the fundamental fermions and their interactions with the gauge bosons. For the weak interaction this results in,

$$\mathcal{L}_D = \bar{\psi}\gamma^\mu \partial_\mu \psi - J^\mu_\pm W^\pm_\mu - J^\mu_0 Z_\mu, \tag{1.3}$$

with the charged and neutral current interactions with the $W^\pm$ and Z written explicitly. The kinetic energy of the gauge fields are described by $\mathcal{L}_G$. The Higgs term of the Lagrangian, $\mathcal{L}_H$, describes the auxiliary field that is needed for spontaneous symmetry breaking.

The couplings between the fermion fields and the Higgs field are incorporated in the Yukawa part of the Lagrangian, $\mathcal{L}_Y$. Adding fermion mass terms to the Lagrangian by hand would break gauge invariance; the masses have to be added via spontaneous symmetry breaking.

The standard-model gauge group $SU(3)_c \times SU(2)_L \times U(1)_Y$ is spontaneously broken into $SU(3)_c \times U(1)_{EM}$ via the Higgs mechanism. To obtain gauge-invariant mass terms for the quarks Yukawa interactions are added to the Lagrangian. The Yukawa terms couple the left-handed $SU_L(2)$ quark doublets, $Q_L = \binom{U_L}{D_L} = \binom{u_L, c_L, t_L}{d_L, s_L, b_L}$ or lepton doublets $L_L = \binom{\nu_L}{l_L} = \binom{\nu_{eL}, \nu_{\mu L}, \nu_{\tau L}}{e_L, \mu_L, \tau_L}$ via the Higgs doublet $\phi = \binom{\phi^+}{\phi^0}$, to the corresponding right-handed quark singlets, $D_R = d_R, s_R, b_R$ or lepton singlets $l_R = e_R, \mu_R, \tau_R$ respectively.

After symmetry breaking the particles acquire a mass and the expression for the interaction currents become,

$$\begin{aligned} J^\mu_+ &= \frac{g}{2\sqrt{2}} \bar{\psi}\gamma^\mu (1-\gamma^5) V_{CKM} \psi, \\ J^\mu_0 &= \frac{g}{2\cos\theta_w} \bar{\psi}\gamma^\mu (G_V - G_A \gamma^5)\psi. \end{aligned} \tag{1.4}$$

Whereas at tree level the charged current changes the flavour of quarks by means of the CKM matrix V_{CKM}, the neutral current does not; there are no flavour-changing neutral currents at tree level. However, flavour-changing neutral transitions can occur via quantum loops.

1.2 Rare *B* decays

Rare B-meson decays due to flavour-changing neutral currents are a good testing ground for the standard model since they are forbidden at tree level. However as heavy particles are allowed in loop diagrams, processes beyond the standard model may be seen in these rare decays. Luckily, also non-perturbative effects are small in heavy ($m_{q_H} > \Lambda_{qcd}$) meson systems, which makes the study of these rare B-meson decays sensitive for the existence of new particles.

1.2.1 Exclusive versus inclusive decays

Studies of exclusive rare decays modes involve specific experimental signatures, making experimental selection easier and cleaner. Inclusive modes are experimentally more

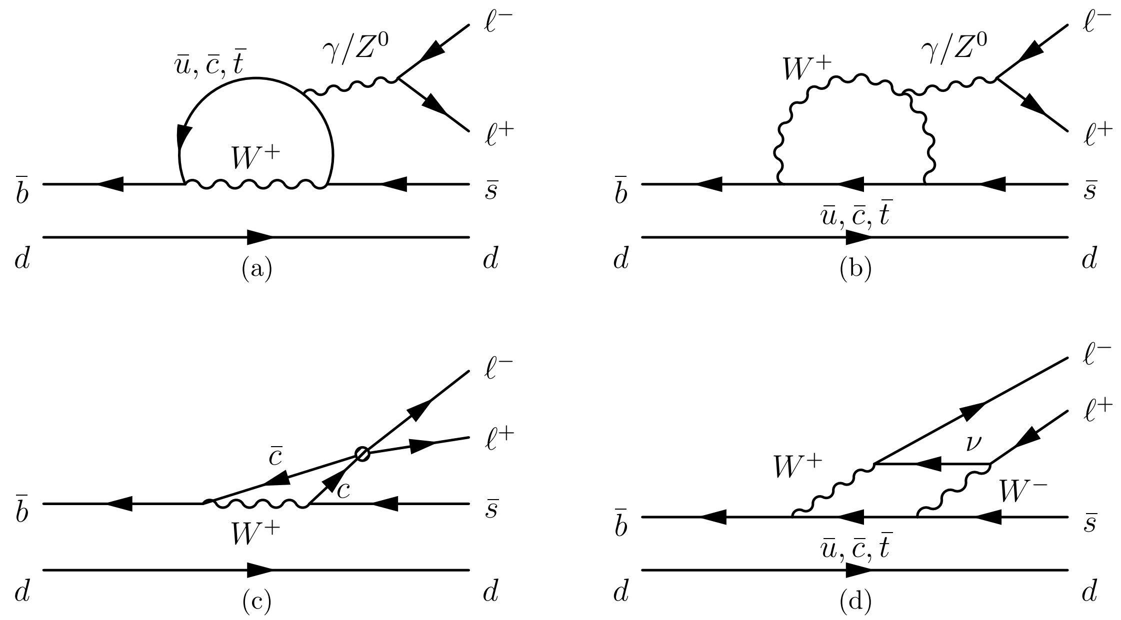

Figure 1.1: *Standard model Feynman diagrams for the decay $B^0 \to K^{*0}\ell^+\ell^-$ contributing most to the forward-backward asymmetry. Diagrams (a) and (b) are penguin diagrams, diagram (c) depicts the decay via a $c\bar{c}$ bound state, like $B \to J/\psi(\ell\ell)K^*$, and in diagram (d) an exchange via two W bosons is given.*

difficult due to the large background one has to reject. From a theoretical point of view it is harder to calculate exclusive cross-sections, while inclusive modes are cleaner and uncertainties can be well controlled by approximations in Heavy Quark Effective Theory (HQET) and Operator Product Expansion (OPE). When considering hadronic exclusive decays hadronic matrix elements are present which are usually not calculable due to non-perturbative QCD effects. The hadronic matrix elements involved in decays of heavy particles can, however, in some cases be estimated with heavy-quark symmetry [8].

The subject of this thesis is the semi-leptonic exclusive decay $B^0 \to K^{*0}\mu^+\mu^-$. In comparison to fully hadronic decays, semi-leptonic decays are considered theoretically cleaner due to the limited amount of hadrons involved.

The quark level sub-process $b \to s\ell^+\ell^-$ can be described by an effective theory which will be done in section 1.3. The uncertainties from hadronic form factors for the exclusive decay will be mentioned in section 1.4.1. The lowest order standard model Feynman diagrams relevant for this process are shown in Fig. 1.1.

The same final state can be reached via a resonant (real) $c\bar{c}$ intermediate state or non-resonant (virtual) $c\bar{c}$ states as shown in Fig. 1.1(c). These are difficult to calculate because long-distance effects play a role in the formation of the intermediate state. Usually in the analysis one omits the regions of invariant mass where the resonances dominate. The effects of the non-resonant states are incorporated in the constants of

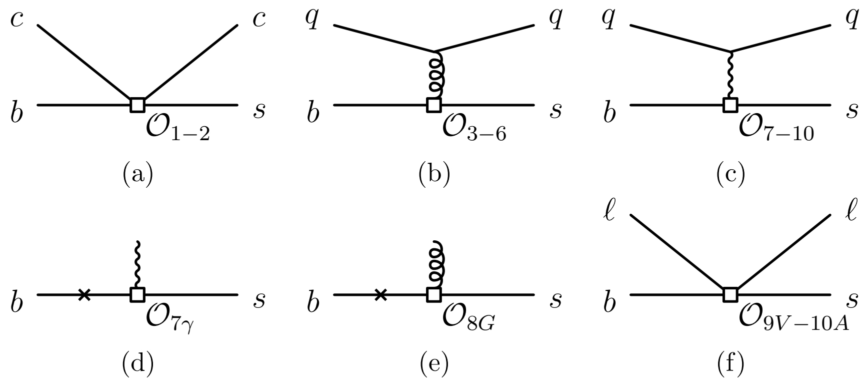

Figure 1.2: *Diagrams representing the terms in the OPE* (1.5) *where the small box signifies an insertion of a four-quark operator $\mathcal{O}_i$. The cross in Figs. (d) and (e) signifies a helicity flip.*

an effective theory [9] which is described next.

1.3 Effective theory for $B^0 \to K^*\ell^+\ell^-$

The flavour-changing neutral interactions are due to loop diagrams involving heavy virtual particles, the W-boson or heavy "beyond-SM" particles. These particles propagate over much shorter distances than $1/m_b$, and hence can be described by local operators. The two distance scales in the decay of a hadron can be separated at a particular scale μ by performing an operator product expansion (OPE): long-distance contributions (pertaining to soft momenta) are contained in local operator matrix elements and the short-distance parts (hard scattering) are described by coefficients. Wilson [10] proposed a way of writing the product of two local fields at different points, $A(x)$ and $B(y)$ as an expansion of a set of local fields at the same point $\mathcal{O}_n(x)$ using coefficients C_n such that, $A(x)B(y) = \sum_n C_n(x-y)\mathcal{O}_n(x)$.

For a $b \to s$ transition mediated with a top quark, the dynamics of the system are generally described by an effective Hamiltonian [11]:

$$H_{\text{eff}} = -\frac{G_F}{\sqrt{2}} V_{tb}V_{ts}^* \sum_i C_i(\mu, M_{heavy})\mathcal{O}_i(\mu). \tag{1.5}$$

The summation proceeds over all the local operators for a particular decay, $\mathcal{O}_i$, weighted with Wilson coefficients $C_i(\mu, M_{heavy})$. Both depend on the separation scale μ at which they are calculated, although the effective Hamiltonian should not.

The inclusive rare decay $B^0 \to X_s\ell^+\ell^-$ has been calculated with the help of OPE methods. The different terms do not strictly represent the various Feynman diagrams normally used in perturbation theory, but rather represent the Lorentz structure and colour structure of the $b \to s$ transition.

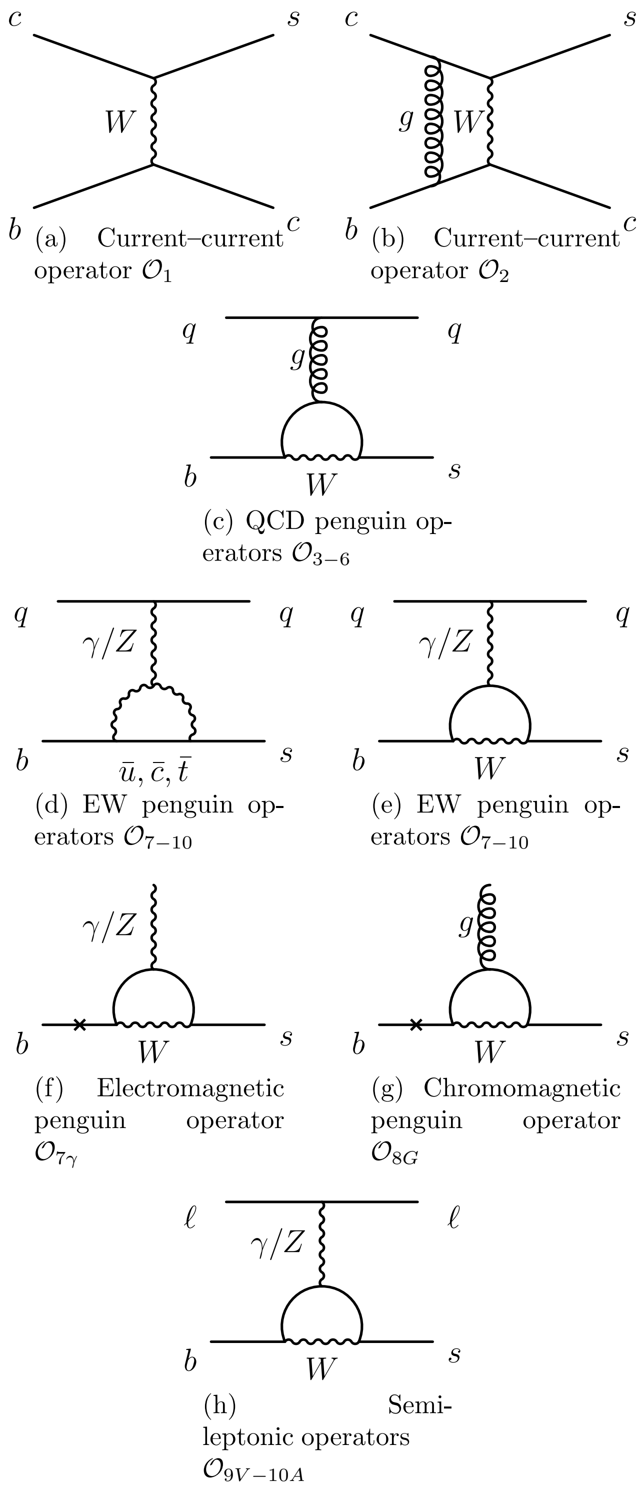

(a) Current–current operator $\mathcal{O}_1$

(b) Current–current operator $\mathcal{O}_2$

(c) QCD penguin operators $\mathcal{O}_{3-6}$

(d) EW penguin operators $\mathcal{O}_{7-10}$

(e) EW penguin operators $\mathcal{O}_{7-10}$

(f) Electromagnetic penguin operator $\mathcal{O}_{7\gamma}$

(g) Chromomagnetic penguin operator $\mathcal{O}_{8G}$

(h) Semi-leptonic operators $\mathcal{O}_{9V-10A}$

Figure 1.3: *Typical lower order Feynman diagrams corresponding to the operators in the effective theory. The cross in Figs. (f) and (g) indicates a helicity flip. Colour exchange diagrams are not shown for the operators except for* $\mathcal{O}_2$*.*

The allowed basis of operators (see [12]) upto mass dimension 6 is given by the following operators [13, 14, 15, 16, 17, 11], which are visualised in Fig. 1.2 while the corresponding Feynman diagrams belonging to the lowest orders are shown in Fig. 1.3.

Current–current operators:

$$\begin{aligned}
\mathcal{O}_1 &= (\bar{s}_\alpha \gamma_\mu P_L c_\alpha)(\bar{c}_\beta \gamma^\mu P_L b_\beta). \\
\mathcal{O}_2 &= (\bar{s}_\alpha \gamma_\mu P_L c_\beta)(\bar{c}_\beta \gamma^\mu P_L b_\alpha),
\end{aligned} \tag{1.6}$$

QCD penguin operators:

$$\begin{aligned}
\mathcal{O}_3 &= (\bar{s}_\alpha \gamma_\mu P_L b_\alpha) \sum_{q=u,d,s,c,b} (\bar{q}_\beta \gamma^\mu P_L q_\beta), \\
\mathcal{O}_4 &= (\bar{s}_\alpha \gamma_\mu P_L b_\beta) \sum_{q=u,d,s,c,b} (\bar{q}_\beta \gamma^\mu P_L q_\alpha), \\
\mathcal{O}_5 &= (\bar{s}_\alpha \gamma_\mu P_L b_\alpha) \sum_{q=u,d,s,c,b} (\bar{q}_\beta \gamma^\mu P_R q_\beta), \\
\mathcal{O}_6 &= (\bar{s}_\alpha \gamma_\mu P_L b_\beta) \sum_{q=u,d,s,c,b} (\bar{q}_\beta \gamma^\mu P_R q_\alpha).
\end{aligned} \tag{1.7}$$

EW penguin operators:

$$\begin{aligned}
\mathcal{O}_7 &= \frac{3}{2}(\bar{s}_\alpha \gamma_\mu P_L b_\alpha) \sum_{q=u,d,s,c,b} e_q (\bar{q}_\beta \gamma^\mu P_R q_\beta), \\
\mathcal{O}_8 &= \frac{3}{2}(\bar{s}_\alpha \gamma_\mu P_L b_\beta) \sum_{q=u,d,s,c,b} e_q (\bar{q}_\beta \gamma^\mu P_R q_\alpha), \\
\mathcal{O}_9 &= \frac{3}{2}(\bar{s}_\alpha \gamma_\mu P_L b_\alpha) \sum_{q=u,d,s,c,b} e_q (\bar{q}_\beta \gamma^\mu P_L q_\beta), \\
\mathcal{O}_{10} &= \frac{3}{2}(\bar{s}_\alpha \gamma_\mu P_L b_\beta) \sum_{q=u,d,s,c,b} e_q (\bar{q}_\beta \gamma^\mu P_L q_\alpha).
\end{aligned} \tag{1.8}$$

Electromagnetic and chromomagnetic penguin operators:

$$\begin{aligned}
\mathcal{O}_{7\gamma} &= \frac{e}{8\pi^2}\, \bar{s}_\alpha \sigma_{\mu\nu} \left(m_b P_R + m_s P_L\right) b_\alpha F^{\mu\nu}, \\
\mathcal{O}_{8G} &= \frac{g_s}{8\pi^2}\, \bar{s}_\alpha T^a_{\alpha\beta} \sigma_{\mu\nu} \left(m_b P_R + m_s P_L\right) b_\beta G^{a\mu\nu}.
\end{aligned} \tag{1.9}$$

Semi-leptonic operators:

$$\mathcal{O}_{9V} = \frac{e}{8\pi^2}\,(\bar{s}_\alpha \gamma^\mu P_L b_\alpha)\,(\bar{\ell}\gamma_\mu \ell),$$
$$\mathcal{O}_{10A} = \frac{e}{8\pi^2}\,(\bar{s}_\alpha \gamma^\mu P_L b_\alpha)\,(\bar{\ell}\gamma_\mu \gamma_5 \ell). \tag{1.10}$$

The indices α, β denote colour, a is an $SU_c(3)$ label on the gluon field tensors $G^{a\mu\nu}$, SU(3) color generator $T^a_{\alpha\beta}$ and $P_{L,R} = (1 \mp \gamma_5)/2$ are the chiral projectors. The quark fields for up, down, strange, charm and bottom are denoted respectively u, d, s, c and b. The generic quark field is denoted q and the lepton field is written as ℓ. The electromagnetic field tensor is $F^{\mu\nu}$ and the anti-symmetric tensor $\sigma^{\mu\nu} = \frac{i}{2}(\gamma^\mu\gamma^\nu - \gamma^\nu\gamma^\mu)$. The terms with a $\sigma^{\mu\nu}$ signify interactions that give rise to an anomalous magnetic moment of the quarks [12].

The semi-leptonic operators $\mathcal{O}_{9V}$ and $\mathcal{O}_{10A}$ and the electromagnetic penguin operator $\mathcal{O}_{7\gamma}$ are the dominant contributions for the $b \to s\ell\ell$ decays.

The effective Hamiltonian at the energy scale $\mu = m_b$ for the decay $b \to s\ell^+\ell^-$ can be split in two parts [18], where one part is the effective Hamiltonian for the radiative decay $b \to s\gamma$ containing only operator $\mathcal{O}_7$, and the other part encodes the contributions which have a leptonic coupling. The reason for splitting the Hamiltonian in this way is that the branching ratio measurement of the decay $b \to s\gamma$ constrains the absolute value of the Wilson coefficient $C_{7\gamma}$, as will be shown in Sec. 1.6. The effective Hamiltonian is written as

$$H_{\text{eff}}(b \to s\ell^+\ell^-) = H_{\text{eff}}(b \to s\gamma) + H_{\text{eff}}(b \to s\ell^+\ell^-)_{9,10} \tag{1.11}$$

with the effective Hamiltonian for the radiative decay [11]

$$H_{\text{eff}}(b \to s\gamma) = -\frac{G_F}{\sqrt{2}} V_{tb} V^*_{ts} \left[\sum_{i=1}^{6} C_i \mathcal{O}_i + C_{7\gamma L}\mathcal{O}_{7\gamma L} + C_{7\gamma R}\mathcal{O}_{7\gamma R} + C_{8G}\mathcal{O}_{8G}\right]. \tag{1.12}$$

Here the operator $\mathcal{O}_{7\gamma}$ is explicitly split in a chiral left-handed and right-handed part. Note that this operator requires a chirality flip which is suppressed by the mass of the down-type quark [19]. This leads to a right-handed b-quark in the coupling and therefore the left-handed component is helicity suppressed with a factor m_s/m_b. There are models for which the left-handed component is large [20]. The effective Hamiltonian for the leptonic couplings is written as

$$H_{\text{eff}}(b \to s\ell^+\ell^-)_{9,10} = -\frac{G_F}{\sqrt{2}} V_{tb} V^*_{ts} \frac{\alpha}{\pi}[C_{9V}\mathcal{O}_{9V} + C_{10A}\mathcal{O}_{10A}]. \tag{1.13}$$

The final states of the resonant and the non-resonant process are indistinguishable. In the region with the dilepton invariant mass around the J/ψ mass, the operators for the resonant process, $\mathcal{O}_1$ and $\mathcal{O}_2$, mix[2] with the non-resonant dilepton operator $\mathcal{O}_{9V}$. The Wilson coefficient C_{9V} will therefore be changed due to the long distance processes, giving rise to[3] C_9^{eff}.

[2]This is caused by renormalisation, in which at different scales μ, combinations of operators with the same quantum numbers result in new composite or *effective* operators.

[3]Henceforth we shall use C_9 to signify C_{9V} since the EW penguin operators $\mathcal{O}_{7-10}$ do not play a role in this decay [13].

1.3.1 Hadronic form factors

The exclusive decay $B^0 \to K^*\ell^+\ell^-$ is a transition of hadronic states in contrast to the transition of the quark states $b \to s\ell\ell$. As a consequence the operator matrix elements need to take into account hadronic form factors.

The introduction of hadronic states imposes model dependencies. The hadronic matrix elements contain q^2-dependent form factors which parameterise the transition amplitudes. The semileptonic decay $B^0 \to K^*\ell^+\ell^-$ is described by matrix elements containing 7 form factors described in the literature [18, 8]. In the following formulae the four-momenta p_B and p_K are the momenta of the B-meson and K^*-meson respectively, and $q = p_B - p_K$ is the four-momentum of the dilepton system. The K^* polarisation four-vector is denoted $\epsilon^{*\mu}$. The semi-leptonic form factors ($A_{1,2,3}$ and V) of the $(V - A)$ current are given in the matrix element:

$$\begin{aligned}\langle K^*(p_K)|\bar{s}(\gamma_\mu - \gamma_\mu\gamma_5)b|B(p_B)\rangle = &-i\epsilon^*_\mu(m_B + m_{K^*})A_1(s) \\ &+ i(p_B + p_K)_\mu(\epsilon^* p_B)\frac{A_2(s)}{(m_B + m_{K^*})} \\ &+ iq_\mu(\epsilon^* p_B)\frac{2m_{K^*}}{s}(A_3(s) - A_0(s)) \\ &+ \epsilon_{\mu\nu\rho\sigma}\epsilon^{*\nu}p_B^\rho p_K^\sigma\frac{2V(s)}{m_B + m_{K^*}}. \end{aligned} \tag{1.14}$$

with the relations

$$\begin{aligned} A_3(s) &= \frac{m_B + m_{K^*}}{2m_{K^*}}A_1(s) - \frac{m_B - m_{K^*}}{2m_{K^*}}A_2(s), \\ A_0(0) &= A_3(0). \end{aligned} \tag{1.15}$$

For the modes via a penguin diagram the tensor form factors $T_{1,2,3}$ in the following matrix element plays a role:

$$\begin{aligned}\langle K^*(p_K)|\bar{s}\sigma_{\mu\nu}q^\nu(1 + \gamma_5)b|B(p_B)\rangle = &\, i\epsilon_{\mu\nu\rho\sigma}\epsilon^{*\nu}p_B^\rho p_K^\sigma 2T_1(s) \\ &+ T_2(s)\big\{\epsilon^*_\mu(m_B^2 - m_{K^*}^2) - (\epsilon^* p_B)(p_B + p_K)_\mu\big\} \\ &+ T_3(s)(\epsilon^* p_B)\big\{q_\mu - \frac{s}{m_B^2 - m_{K^*}^2}(p_B + p_K)_\mu\big\}, \end{aligned} \tag{1.16}$$

where $\epsilon_{\mu\nu\rho\sigma}$ is the four dimensional Levi-Civita tensor.

The form factors listed in Table 1.1, $A_{1,2,3}$ and V and $T_{1,2,3}$ have been determined for zero momentum transfer. Each form factor will need to be evolved to the proper scale of $s = m_{ll}^2$. This is done with the emperically determined evolution formula:

$$F(\hat{s}) = F(0)e^{c_1\hat{s} + c_2\hat{s}^2}, \tag{1.17}$$

where $\hat{s} = s/m_B$. The evolution parameters are also reproduced in Table 1.1.

	A_1	A_2	A_0	V	T_1	T_2	T_3
$F_i(0)$	0.294	0.246	0.412	0.399	0.334	0.334	0.234
c_1	0.656	1.237	1.543	1.537	1.575	0.562	1.230
c_2	0.456	0.822	0.954	1.123	1.140	0.481	1.089

Table 1.1: *Form factors in zero momentum transfer and parameters for the momentum evolution [21].*

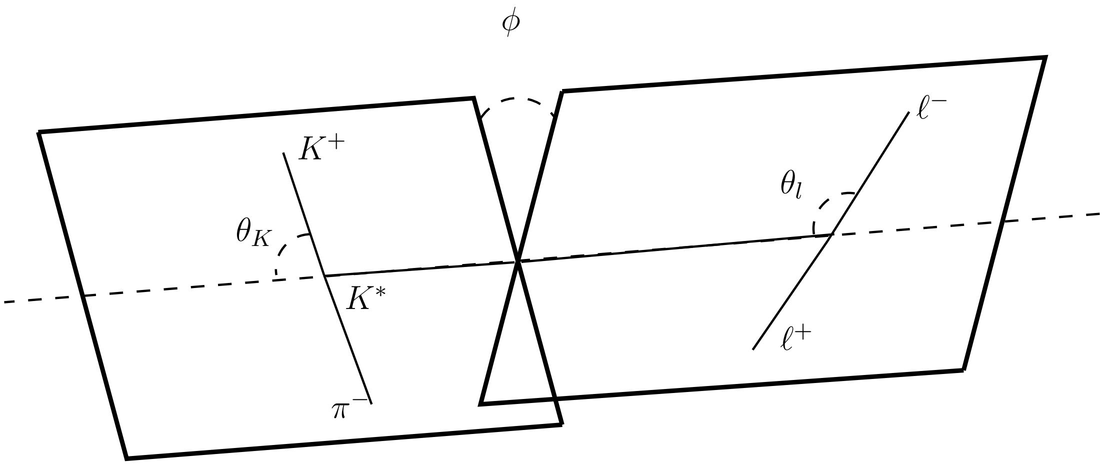

Figure 1.4: *Diagram showing the relative planar orientation of the decay products for $B^0 \to K^{*0}(K^+\pi^-)\ell^+\ell^-$ in the helicity framework. The definition of the angles is given in the text.*

1.4 Kinematics

1.4.1 1.4.1 Decay angles in $B^0 \to K^*\ell^+\ell^-$

The decay $B^0 \to K^*\ell^+\ell^-$ has a four-particle final state, consisting of $K^* \to K^+\pi^-$ together with two leptons. In order to describe the kinematic variables for the decay and to calculate the angular distributions, the relevant decay angles will be defined first. For the definitions of the decay angles Fig. 1.4 can be used as reference. The angle θ_K is the polar angle of the K momentum in the rest system of the K^* with respect to the helicity axis (direction of the K^* in the B-rest frame). The angle θ_l is the polar angle of the negative lepton in the dilepton rest frame with respect to the dilepton helicity axis. The azimuthal angle between the decay plane of $K^* \to K\pi$ and the $\ell^+\ell^-$ plane is denoted ϕ.

To formalise the definitions of the angles they can be defined as follows [22]: Let $\mathbf{p}$ denote a three-momentum vector in the B^0 rest frame, $\mathbf{q}$ a three-momentum vector in the dilepton rest frame, and $\mathbf{r}$ a three-momentum vector in the K^* rest frame. Three unit vectors are defined, denoting a coordinate basis:

$$\mathbf{e}_z = \frac{\mathbf{p}_{K^+} + \mathbf{p}_{\pi^-}}{|\mathbf{p}_{K^+} + \mathbf{p}_{\pi^-}|},\ \mathbf{e}_l = \frac{\mathbf{p}_{\ell^+} \times \mathbf{p}_{\ell^-}}{|\mathbf{p}_{\ell^+} \times \mathbf{p}_{\ell^-}|},\ \mathbf{e}_K = \frac{\mathbf{p}_{K^+} \times \mathbf{p}_{\pi^-}}{|\mathbf{p}_{K^+} \times \mathbf{p}_{\pi^-}|}. \tag{1.18}$$

The angles then get the following definitions:

$$\cos\theta_l = \frac{\mathbf{q}_{\ell^+} \cdot \mathbf{e}_z}{|\mathbf{q}_{\ell^+}|}, \tag{1.19}$$

$$\cos\theta_K = \frac{\mathbf{r}_{K^+} \cdot \mathbf{e}_z}{|\mathbf{r}_{K^+}|}, \tag{1.20}$$

$$\sin\phi = (\mathbf{e}_l \times \mathbf{e}_K) \cdot \mathbf{e}_z,\ \cos\phi = \mathbf{e}_K \cdot \mathbf{e}_l. \tag{1.21}$$

For the $\bar{B}^0$ meson the charged-conjugate decay is defined with the same angles defined with all the charges conjugated. The angles θ_l and θ_K are defined on the interval $[0, \pi]$.

1.4.2 Dimuon invariant mass distribution

The kinematically allowed region for the dilepton invariant mass squared (s) is

$$4m_l^2 \leq s \leq (m_B - m_{K^*})^2. \tag{1.22}$$

The differential cross-section versus the squared dilepton-mass for the process $B^0 \to K^{*0}\mu^+\mu^-$ is shown in Fig. 1.5 for several physics models in which the Wilson coefficients are scaled with a factor r with respect to their standard model values.

As was mentioned already in section 1.3 the resonant and non-resonant parts of the decay both contribute. A source of background in $B^0 \to K^{*0}\mu^+\mu^-$ arises from the sub-process $b \to sc\bar{c} \to s\mu^+\mu^-$. The resonant part of the $c\bar{c}$ in the form of J/ψ and $\psi(2S)$ is restricted to narrow mass windows around the resonances, as is shown in Fig. 1.5.

The uncertainty of the form factors and the long-distance calculations contribute significantly to the differential cross-section as is shown by the shaded region. The low invariant mass region is the most interesting because perturbation theory together with power corrections is expected to yield a reliable result below the resonance regions [24]. By measuring angular distributions one can extract asymmetries that are based on ratios of amplitudes in which the uncertainties due to the form factors and the long-distance effects are minimised. Such measurements are more sensitive to new physics and well suited to distinguish different models, as will be shown in the following section.

1.5 Angular decay distributions and forward-backward asymmetry

1.5.1 Helicity basis for $B^0 \to K^{*0}\mu^+\mu^-$

Due to helicity conservation the two decay products in a 2-prong decay of the pseudo-scalar B^0-meson must have the same helicity in the rest frame of the B^0-meson. Hence

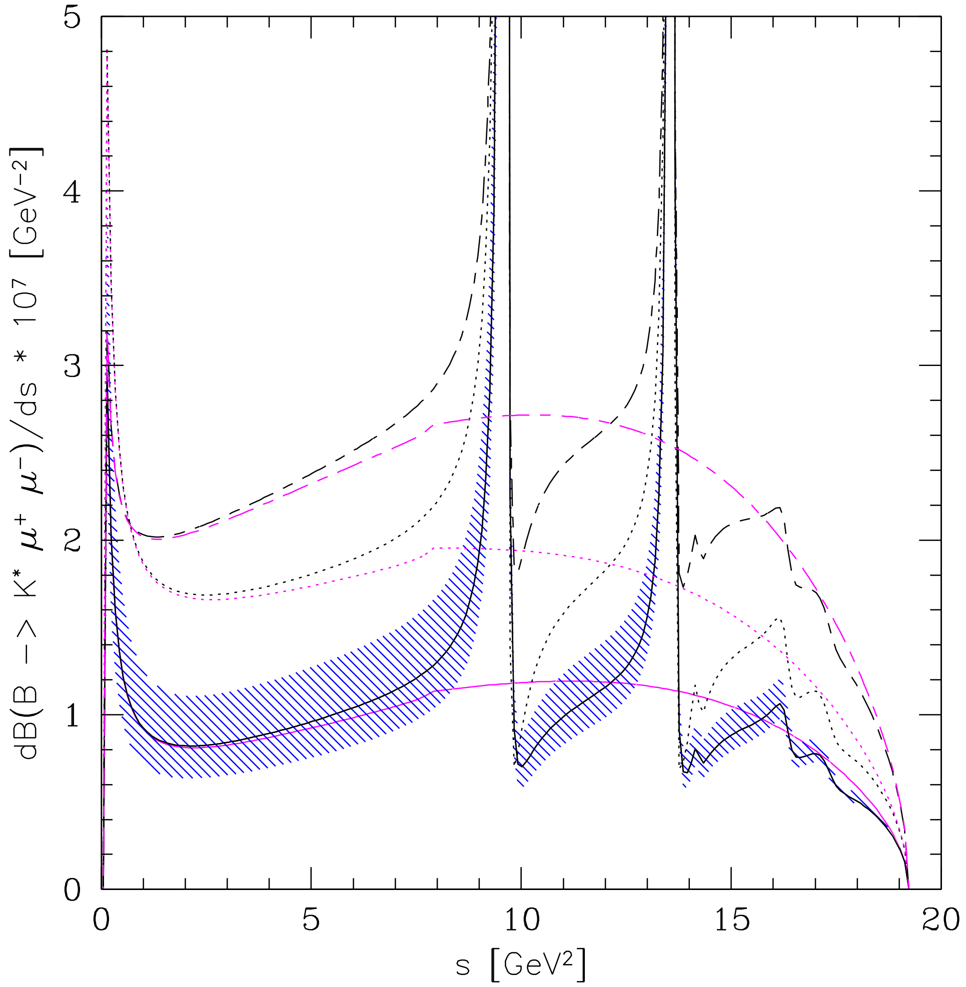

Figure 1.5: *The differential decay rate* $\mathrm{d}\Gamma/\mathrm{d}s$ *in* $B^0 \to K^{*0}\mu^+\mu^-$ *decays, using the form factors as a function of* s*, the invariant mass squared of the dimuon system. All resonant* $c\bar{c}$ *states are parametrized as in [23]. The solid line represents the SM and the shaded area depicts the form factor related uncertainties. The dotted line corresponds to a SUGRA model with* $r_7 = -1.2$*,* $r_9 = 1.03$ *and* $r_{10} = 1$*. The long-short dashed lines correspond to an allowed point in the parameter space of a particular SUSY model, given by* $r_7 = -0.83$*,* $r_9 = 0.92$ *and* $r_{10} = 1.61$*. The corresponding pure short-distance spectra are represented by the lighter lines. Figure taken from [24].*

the helicity of the K^{*0} is equal to that of the dimuon system. The helicity of the vector meson K^{*0} can be either -1, 0 or +1. The differential decay rate can be expressed in terms of helicity amplitudes H_λ: $H_{-1,0,+1}$. The helicity amplitudes can be split into a chiral right-handed and a left-handed part, H^L_λ and H^R_λ. Using these chiral parts the differential cross-section for the process $B^0 \to K^{*0}\mu^+\mu^-$ has been calculated in [18] to be

$$\frac{\mathrm{d}^5\Gamma}{\mathrm{d}p_K^2 \mathrm{d}s \mathrm{d}\cos\theta_K \mathrm{d}\cos\theta_+ \mathrm{d}\phi} = \Phi \sum_{i=1}^{9} I_i A_i, \tag{1.23}$$

with I_i functions of the helicity amplitudes and A_i are functions of the decay angles, θ_K, θ_+ and ϕ, defined in section 1.4.1. The factor Φ is a phase space factor, consisting of momenta and CKM matrix elements.

In terms of helicity amplitudes, H_i, the helicity functions I_i are

$$\begin{aligned}
I_1 &= |H_0^R|^2 + |H_0^L|^2\\
I_2 &= |H_{+1}^L|^2 + |H_{-1}^L|^2 + |H_{+1}^R|^2 + |H_{-1}^R|^2,\\
I_3 &= \cos\alpha_R H_{+1}^R H_{-1}^R + \cos\alpha_L H_{+1}^L H_{-1}^L,\\
I_4 &= \sin\alpha_R H_{+1}^R H_{-1}^R + \sin\alpha_L H_{+1}^L H_{-1}^L,\\
I_5 &= \cos\beta_R H_{+1}^R H_0^R + \cos\gamma_R H_{-1}^R H_0^R) + \cos\beta_L H_{+1}^L H_0^L + \cos\gamma_L H_{-1}^L H_0^L,\\
I_6 &= \sin\beta_R H_{+1}^R H_0^R - \sin\gamma_R H_{-1}^R H_0^R + \sin\beta_L H_{+1}^L H_0^L - \sin\gamma_L H_{-1}^L H_0^L,\\
I_7 &= |H_{+1}^R|^2 - |H_{-1}^R|^2 - |H_{+1}^L|^2 + |H_{-1}^L|^2,\\
I_8 &= \cos\beta_R H_{+1}^R H_0^R - \cos\gamma_R H_{-1}^R H_0^R - \cos\beta_L H_{+1}^L H_0^L + \cos\gamma_L H_{-1}^L H_0^L,\\
I_9 &= \sin\beta_R H_{+1}^R H_0^R - \sin\gamma_R H_{-1}^R H_0^R - \sin\beta_L H_{+1}^L H_0^L - \sin\gamma_L H_{-1}^L H_0^L.
\end{aligned} \tag{1.24}$$

The labels R and L represent the right- and left-handed helicities respectively. In the above equations α denotes the phase between the helicity amplitudes H_{+1} and H_{-1}, β is the phase between amplitudes H_{+1} and H_0 while the phase between amplitudes H_{-1} and H_0 is written as γ.

The functions of the kinematical angles are written as

$$\begin{aligned}
A_1 &= +4\cos^2\theta_K \sin^2\theta_l,\\
A_2 &= +\sin^2\theta_K(1+\cos^2\theta_l),\\
A_3 &= -2\sin^2\theta_K \sin^2\theta_l \cos 2\phi,\\
A_4 &= +2\sin^2\theta_K \sin^2\theta_l \sin 2\phi,\\
A_5 &= -\sin 2\theta_K \sin 2\theta_l \cos\phi,\\
A_6 &= +\sin 2\theta_K \sin 2\theta_l \sin\phi,\\
A_7 &= -2\sin^2\theta_K \cos\theta_l,\\
A_8 &= +2\sin\theta_l \sin 2\theta_K \cos\phi,\\
A_9 &= -2\sin\theta_l \sin 2\theta_K \sin\phi,
\end{aligned} \tag{1.25}$$

with the angles are defined in (1.19), (1.20) and (1.21).

The helicity amplitudes H_i can be expressed in the massless lepton limit in terms of Wilson coefficients and hadronic form factors, and are calculated in *e.g.* [18]. In the standard model, due to the V-A coupling, the negative (positive) helicity states of the K^* ($\bar{K}^*$) are suppressed. In the next section this is explained in the naive parton model.

1.5.2 Forward-backward lepton asymmetry

The differential decay rates as a function of the angles θ_l, θ_K and ϕ depend on the form factors mentioned in Tab. 1.1. The form factors have theoretical uncertainties of the order of 10% [18] and therefore the hadronic uncertainties propagate to the angular distributions. One way of suppressing the effects of the form factors is to calculate asymmetries. One of these quantities is the forward-backward lepton asymmetry.

In the dilepton rest frame, the angle θ_l between the negative lepton and the B-meson is used to define[4] a forward-backward asymmetry:

$$\begin{aligned} A_{FB}(s) &= \frac{\left(\frac{\mathrm{d}\Gamma}{\mathrm{d}s}\right)_F - \left(\frac{\mathrm{d}\Gamma}{\mathrm{d}s}\right)_B}{\left(\frac{\mathrm{d}\Gamma}{\mathrm{d}s}\right)_F + \left(\frac{\mathrm{d}\Gamma}{\mathrm{d}s}\right)_B} \\ &= \frac{\int_0^1 \mathrm{d}\cos\theta_l \frac{\mathrm{d}^2\Gamma}{\mathrm{d}s\,\mathrm{d}\cos\theta_l} - \int_{-1}^0 \mathrm{d}\cos\theta_l \frac{\mathrm{d}^2\Gamma}{\mathrm{d}s\,\mathrm{d}\cos\theta_l}}{\int_0^1 \mathrm{d}\cos\theta_l \frac{\mathrm{d}^2\Gamma}{\mathrm{d}s\,\mathrm{d}\cos\theta_l} + \int_{-1}^0 \mathrm{d}\cos\theta_l \frac{\mathrm{d}^2\Gamma}{\mathrm{d}s\,\mathrm{d}\cos\theta_l}}. \end{aligned} \tag{1.26}$$

The forward direction (F) is denoted by $|\theta_l| < \pi/2$, while the backward direction (B) is denoted $|\theta_l| > \pi/2$. For the charge-conjugate decay mode A_{FB} is defined with θ_l the angle between the charge conjugate lepton and B-meson.

The origin of the forward-backward asymmetry comes from parity violation of the weak current. The standard model behaviour of the A_{FB} of the process $b \to s\mu\mu$ can be explained using a partonic interpretation.

At small values of s the muon pair is produced by a photon, but for sufficiently large values of s the contribution of the Z and W bosons becomes noticeable as parity violating effects [25, 26, 27]. The diagrams in Fig. 1.6(a) and (b) show the possible helicity states of the mesons and the dimuon system for the $\bar{B} \to \bar{K}^*\mu\mu$. Since the s quark is light and the weak current couples only to left-handed chirality, it tends to be polarized in a left-handed helicity state, *i.e.* $\lambda = -1/2$. This means that combined with the spectator quark the $\bar{K}^*$ meson can have a helicity of 0 or -1.

In the rest frame of the $\bar{B}^0$ meson (scalar) the helicity of the $\bar{K}^*$ and the dimuon system are equal. The possible helicity states are sketched in Fig. 1.6(a) and (b). For the case that the $\bar{K}^*$ helicity is 0, depicted in diagram (a), the dimuon in its rest frame is produced with the same helicity. This means that both muons should be created either in a left-handed or right-handed state. However, the weak interaction prefers to create left-handed (helicity) particles and right-handed (helicity) antiparticles. Hence this diagram is dominant in a parity conserving interaction. Since the muons have both the same helicity state there is no preferential direction and thus no A_{FB}[5].

For the case that the $\bar{K}^*$ is produced in a helicity -1 state the diagram depicted in (b) is relevant. The muons in the dimuon rest frame have the opposite helicity $\lambda = +1/2$ and

[4] In this thesis the adopted variable definition [22] for the charge conjugate decay, $\bar{B}_d \to \bar{K}^*\ell^-\ell^+$ that θ_l is the angle between the *positive* lepton and the $\bar{B}$-meson. Hence we assume any CP-violation in this channel to be negligible. This definition can change in literature.

[5] This is also the case for a pseudo-scalar $\bar{K}$ in the decay $\bar{B} \to \bar{K}\mu\mu$ in which the helicity of the Kaon is 0.

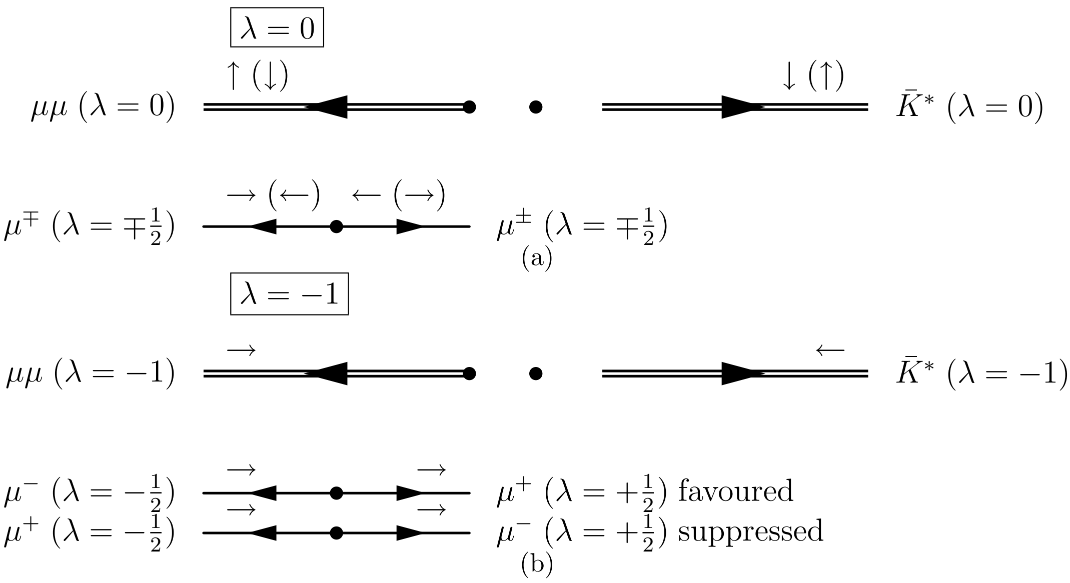

Figure 1.6: *Helicity flow diagrams are shown in (a) and (b), where arrows in the lines indicate momentum flow, arrows over the lines indicate the z component of the spin. The indicated helicity flow is in the $\bar{B}$ rest frame between the dimuon and the $\bar{K}^*$ and the helicity flow in the dimuon rest frame between the muons.*

$\lambda = -1/2$. However when the diagrams with W-exchange and Z-exchange become more important (at higher values of dimuon invariant mass), this weak interaction causes a preference for left-handed helicity for particle (μ^-) and right-handed antiparticle (μ^+). The preference in helicity reflects itself in the preferred direction of the muons with respect to the $\bar{K}^*$ direction (helicity axis). And at higher values of dimuon invariant mass $s \gg s_0$ there will be more μ^+ (*i.e.* with a helicity $\lambda = +1/2$) travelling in the direction of the $\bar{K}^*$, see Fig. 1.6(b).

Comparing to Fig. 1.4 (and keeping in mind this is the charge conjugate decay) this means that there are more events in which there is a backward-going negative lepton ($|\theta_l| > \pi/2$) in $B \to K^*\mu\mu$ and hence, according to the definition of the forward-backward asymmetry in (1.26), the A_{FB} will become negative[6] for higher values of s, see Fig. 1.7.

The numerator of the forward-backward asymmetry is expressed in terms of the helicity amplitudes as [28, 29],

$$F(s) - B(s) \equiv \frac{\mathrm{d}\Gamma^F}{\mathrm{d}s} - \frac{\mathrm{d}\Gamma^B}{\mathrm{d}s} \sim \left[(|H_+^L|^2 - |H_-^L|^2) - (|H_+^R|^2 - |H_-^R|^2)\right] . \tag{1.27}$$

[6]When one takes the charge conjugate decay the arguments result in the same observation.

In the effective theory this can be expressed in terms of the Wilson coefficients as [24]:

$$\begin{aligned} \mathrm{d}A_{FB} = &\frac{G_F^2\alpha^2 m_B^2}{2^8\pi^5}|V_{ts}^* V_{tb}|^2 \hat{s}\lambda(1-4\frac{\hat{m}_\ell^2}{\hat{s}}) \\ &\times C_{10}\left[\mathrm{Re}(C_9^{\mathrm{eff}})VA_1 + \frac{\hat{m}_b}{\hat{s}}C_7^{\mathrm{eff}}(VT_2(1-\hat{m}_K^*) + A_1T_1(1+\hat{m}_K^*))\right], \end{aligned} \tag{1.28}$$

where the hat again denotes division by m_B (or m_B^2), to obtain a dimensionless variable and the Källén (triangle) function $\lambda \equiv \lambda(1, \hat{m}_{K^*}^2, \hat{s}) = 1 + \hat{m}_{K^*}^4 + \hat{s}^2 - 2\hat{s} - s\hat{m}_{K^*}^2(1+\hat{s})$. The label "eff" denotes an effective Wilson coefficient due to operator mixing of $\mathcal{O}_1$ and $\mathcal{O}_9$ or any right-handed contributions to $\mathcal{O}_{7\gamma}$.

The value of s at which A_{FB} vanishes has been shown to be largely insensitive to uncertainties in the hadronic form factors [9]. This makes the zero-crossing point a powerful observable for the search of new physics in the $B^0 \to K^{*0}\mu^+\mu^-$ decay channel.

1.6 SM predictions

The position of the zero-crossing of the asymmetry as a function of the invariant dilepton-mass at leading order is expressed in terms of effective Wilson coefficients[7] as [9]

$$s_0 \simeq \frac{m_B^2 + m_{K^*}^2(2C_{7\gamma}^{\mathrm{eff}}/C_9^{\mathrm{eff}} - 1)}{1 - C_9^{\mathrm{eff}}/2C_{7\gamma}^{\mathrm{eff}}}, \tag{1.29}$$

where the effective Wilson coefficients are calculated at the scale $\mu = m_b$.

The size of $C_{7\gamma}(\mu)$ is constrained from measurements of the $B \to X_s\gamma$ branching ratio in [30]. The inclusive $b \to s\gamma$ branching ratio is calculated with [31, 18]

$$\mathcal{B}(B \to X_s\gamma) = \frac{G_F^2\alpha_{em}^2 m_b^5}{32\pi^4}|V_{ts}^* V_{tb}|^2\left(|C_{7\gamma R}|^2 + |C_{7\gamma L}|^2\right). \tag{1.30}$$

The phase of Wilson coefficient $C_{7\gamma}$ can not be determined by looking at the radiative decay $B \to X_s\gamma$. With a semileptonic decay $B \to X_s\ell^+\ell^-$ the sign can be extracted.

The value for the combined coefficients has been determined from the branching fraction, $\mathcal{B}(B \to X_s\gamma) = (3.15 \pm 0.35 \pm 0.32 \pm 0.26) \times 10^{-4}$, to be [18],

$$|C_{7\gamma L}(m_b)|^2 + |C_{7\gamma R}(m_b)|^2 = 0.081 \pm 0.014.$$

This translates in a bound on $|C_{7\gamma}|$ to

$$0.259 \leq |C_{7\gamma}(\mu = m_b)| \leq 0.308. \tag{1.31}$$

The Wilson coefficients in the standard model case are calculated numerically in [18] and [32] assuming a top mass of 175 GeV, a b-quark mass of $m_b = 4.8$ GeV, a c-quark mass of $m_c = 1.4$ GeV and $\Lambda_{QCD} = 214$ MeV. This yields a value for $C_{10A}(\mu = m_b) =$

[7] Including the use of heavy-quark symmetry to calculate form factor relations.

-4.546. The coefficient C_{9V} is altered due to operator mixing. The effective coefficient in next-to-leading order becomes

$$C_{9V}^{\text{eff}}(\mu = m_b) = 4.153 + 0.381\, g(m_c/m_b, \hat{s}) + 0.033\, g(1, \hat{s}) + 0.032\, g(0, \hat{s}). \tag{1.32}$$

The function $g(z, \hat{s})$ is given in [32]

$$\begin{aligned} g(z,\hat{s}) &= -\frac{8}{9}\ln z + \frac{8}{27} + \frac{4}{9}x \\ &- \frac{2}{9}(2+x)\sqrt{|1-x|}\begin{cases} \ln\left|\frac{\sqrt{1-x}+1}{\sqrt{1-x}-1}\right| + i\pi, & \text{for } x \equiv 4z^2/\hat{s} < 1 \\ 2\arctan(1/\sqrt{x-1}), & \text{for } x \equiv 4z^2/\hat{s} > 1, \end{cases} \end{aligned} \tag{1.33}$$

where $z = m_c/m_b$.

Theoretical predictions of the zero crossing [33] from leading order calculations yield $s_0 = 3.25$ GeV^2. The article [33] makes a conservative estimate for the zero of the asymmetry of

$$s_0 = 4.2 \pm 0.6 \text{ GeV}^2. \tag{1.34}$$

The A_{FB} has been calculated in [24] the standard model and several other models by modifying the Wilson coefficients. The results are plotted in Fig. 1.7. The different behaviour of the asymmetry as a function of s for some of the models is clearly visible.

1.6.1 Modified Wilson coefficients

In case new particles contribute to the loop diagrams, the change of the Wilson coefficients is usually parametrised with r_i, where the coefficients C_i^{SM} are multiplied by factors r_i:

$$r_i = \frac{C_i^{NP} + C_i^{SM}}{C_i^{SM}} = \frac{C_i}{C_i^{SM}}. \tag{1.35}$$

In total five different physics models have been investigated; the SM and four new physics models. They will be briefly highlighted below.

1.7 New physics models

1.7.1 Supersymmetry

One of the possible extensions of the standard model is supersymmetry. Supersymmetric models impose an extra symmetry between fermions and bosons, such that for every fermion there exists a supersymmetric scalar partner known as a sfermion and for every boson there exists a supersymmetric spin-1/2 particle, known as a gaugino. They include at least two scalar Higgs bosons, together with their spin-1/2 counterparts, the higgsinos. At the energy scales that are currently observed, supersymmetry is broken. The ratio between the vacuum expectation values of the two Higgs bosons is $\tan\beta = \frac{\langle h_2^0 \rangle}{\langle h_1^0 \rangle}$. In the

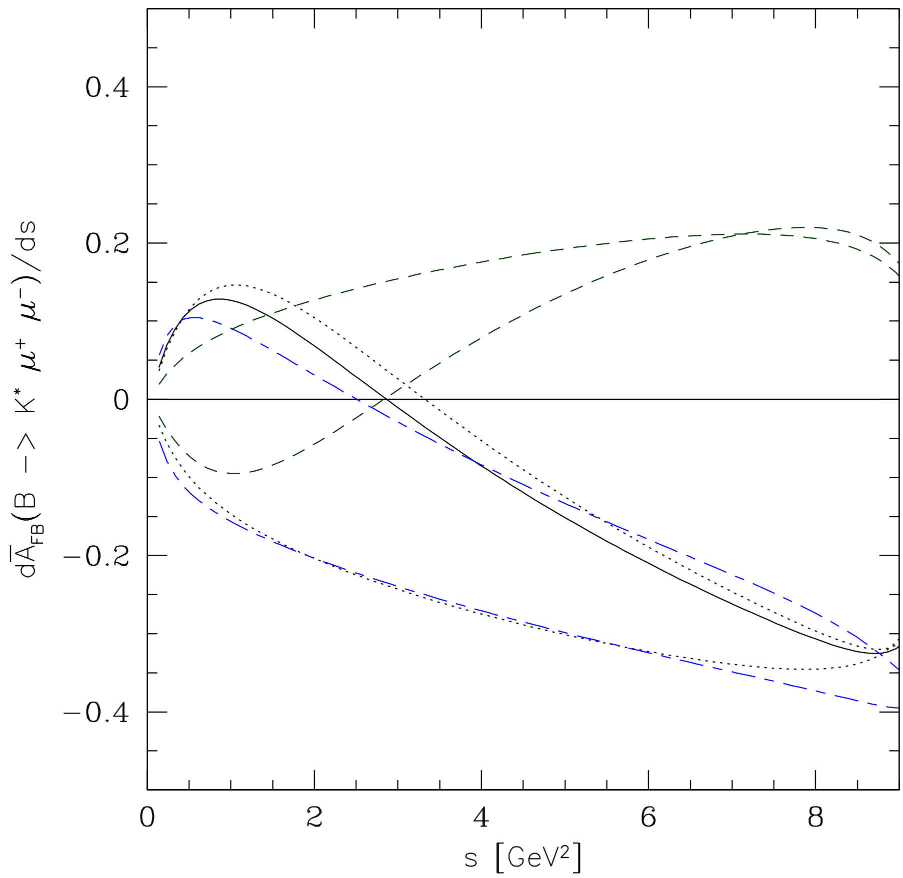

Figure 1.7: *The normalized forward-backward asymmetry* (1.26) *in* $B^0 \to K^{*0}\mu^+\mu^-$ *decay as a function of* s*. All resonant* $c\bar{c}$ *states are parametrized as in [23]. The solid line denotes the SM prediction. The dotted (long-short dashed) lines correspond to a SUGRA (a SUSY) model, using* $r_7 = \pm 1.2$, $r_9 = 1.03$, $r_{10} = 1.0$ *(*$r_7 = \pm 0.83$, $r_9 = 0.92$, $r_{10} = 1.61$*) with the upper and lower curves representing the* $C_{7,eff} < 0$ *and* $C_{7,eff} > 0$ *case, respectively. The dashed curves indicating a positive asymmetry for large* s *correspond to a SUSY model using* $r_7 = \pm 0.83$, $r_9 = 0.79$, $r_{10} = +0.38$*. Figure taken from [24].*

minimal supersymmetric extension to the standard model (MSSM) there are 124 free parameters. To restrict this number several assumptions can be made in specific types of supersymmetric models like MIA-SUSY and SUGRA models, which will be mentioned below. The forward-backward asymmetry is a sensitive observable to distinguish various models, as is shown in Fig. 1.7. The models shown in the figure are described below.

MIA-SUSY

One of the models that are investigated are the minimal insertion approach SUSY models (MIA-SUSY). For the extended flavour structure of supersymmetric models one can

Model	$r_{7\gamma}$	r_{9V}	r_{10A}
SM	1	1	1
SUSY1	0.83	0.92	1.61
SUSY2	-0.83	0.92	1.61
SUGRA1	1.2	1.03	1
SUGRA2	-1.2	1.03	1

Table 1.2: *Wilson-coefficient modification factors relative to the Standard Model. The standard model, two particular SUSY models and two particular SUGRA models were used in the generation of the MC.*

write Yukawa matrices analogous to the Yukawa matrices in the standard model, in the so-called super-CKM (SCKM) basis, including both quarks and squarks. Due to this extended structure new sources of flavour violation can appear. To reduce the contribution of flavour violation to the experimental limits, the squark-quark mixing should be almost flavour diagonal. The mass insertion approximation adds off-diagonal elements to the squark mass matrices to tune the amount of flavour violation. The Wilson coefficients for the effective couplings for two particular type of MIA-SUSY models were calculated in [24]. These models are labeled "SUSY" in this thesis.

SUGRA

A SUGRA model is a supersymmetric (SUSY) model where the breaking of the symmetry is mediated by gravity. In supersymmetry models the masses of the superpartners are taken to have a universal structure at the GUT scale, then evolved to lower scales.

In this thesis Wilson coefficients have been used for a so-called relaxed SUGRA (rSUGRA) model. This is a supergravity model (SUGRA) where the universality condition at the GUT scale has been relaxed. The SUGRA model is described in [34, 35] where the Wilson coefficients were calculated for value of $\tan\beta = 30$ ($C_7 > 0$) and $\tan\beta < 10$ ($C_7 < 0$). These models are labeled "SUGRA" in this thesis.

The models which are used in the generation of events are based on Wilson-coefficient modifications reproduced from [24]. The values of the modification factors r_i for the different models can be found in Table 1.2. These models have been implemented in the LHCb Monte Carlo code and from the event generator distributions have been created. The forward-backward asymmetry calculated from these distributions is depicted in Fig. 1.8. The models which have a zero crossing are SM, SUSY1 and SUGRA1. The two models without a zero crossing that are not shown in the figure are SUSY2 and SUGRA2.

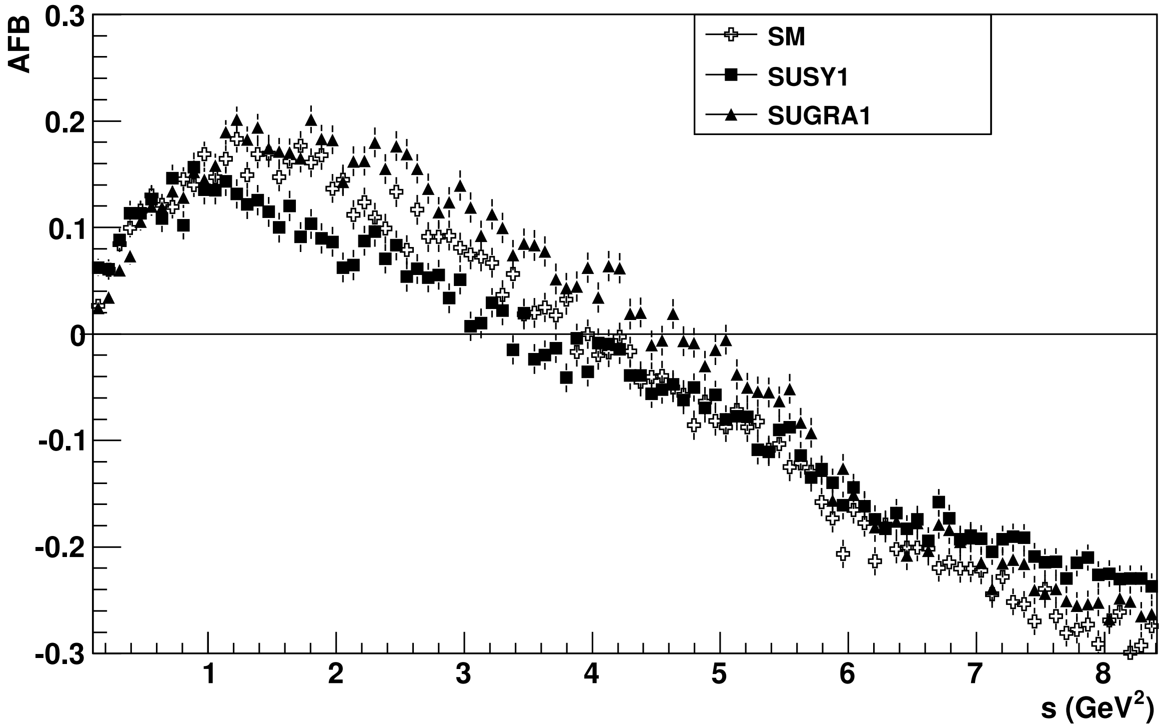

Figure 1.8: *Asymmetries from the models with a zero-crossing point that are used in the fitting procedure described in chapter 7.*

2

The LHCb experiment

In this chapter an overview is given of the LHCb experiment located at the LHC accelerator. The accelerator and its design parameters are described in the first section. Next, the LHCb experiment and its subdetectors are reviewed. Lastly, the trigger and data acquisition system are described.

The LHCb experiment is dedicated to measuring CP violation in the B-meson system and to exploring rare B-decays. These measurements will precisely determine the CKM angles, in particular γ, and possibly expose new physics in flavour-changing neutral currents [36].

2.1 Large hadron collider

The Large Hadron Collider (LHC) is a circular proton-proton collider that will be in operation at CERN. At the LHC there are four main experiments as displayed in Fig. 2.1. The designed centre of mass (COM) energy is $\sqrt{s} = 14$ TeV. To reach this energy the protons pass through several pre-accelerators. From an initial linear accelerator LINAC), the protons are subsequently fed through the Proton Synchroton Booster (PSB), the Proton Synchrotron (PS), and the Super Proton Synchroton (SPS) from which they are injected into the LHC at an energy of 450 GeV. In the LHC the beams are accelerated to the final energy of 7 TeV.

The particles are kept in orbit around the 27 km accelerator ring by superconducting dipole magnets. At the final energy of 7 TeV the magnetic field reaches 8.33 T. To accomodate both beam lines, two coils are built in one magnet body. A cryostat is used to keep the coils at a temperature of 1.9 K.

The beams cross in the interaction point of the LHCb experiment with a half crossing angle of 200 μrad [37]. The particles in each beam are concentrated in bunches. The bunch frequency of the LHC is $f_{LHC} = 40$ MHz, corresponding to a bunch crossing every 25 ns.

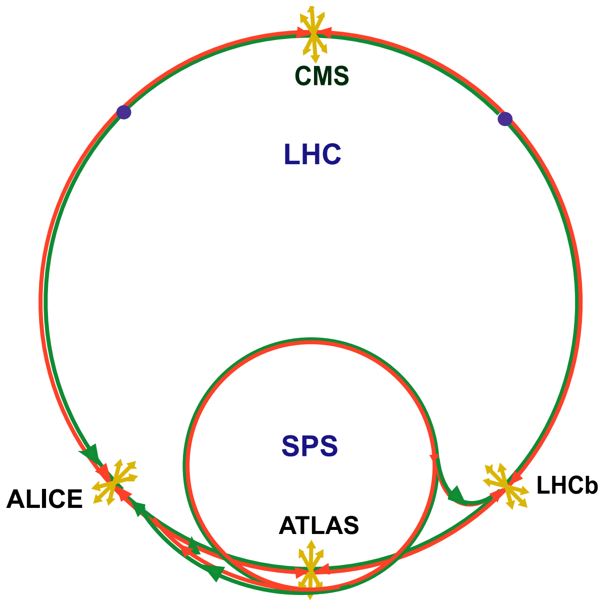

Figure 2.1: *Schematic representation of the LHC accelerator and the location of the main experiments. Also shown is the last pre-accelerator, the SPS.*

LHC parameter	Value
COM energy	14 TeV
Circumference	26.7 km
f_{LHC}	40 MHz
Dipole field	8.3 T
Bunch slots	3564
Filled bunches	2808
Particles per bunch	1.15×10^{11}
Nominal luminosity[1]	$1 \times 10^{34}\text{cm}^{-2}\text{s}^{-1}$
Luminosity lifetime	10 h

Table 2.1: *Design parameters of the LHC.*

In the LHC beams there are 3564 bunch slots available. As a result of the injection routine used by the pre-accelerators, only 2808 slots are filled. Relative to the Atlas and CMS experiments, the LHC beam at the LHCb experiment is 1/8 cycle out of phase plus 3 additional bunch periods due to the position of the interaction point. As a consequence not all bunch crossings are between filled bunches. At the interaction point of LHCb the LHC has 2649 bunch crossings with both bunches filled. Thus the fraction of filled bunches equals $R_{fill} = \frac{2649}{3564} \approx 0.74$ [36]. More design parameters of the LHC are summarised in Table 2.1.

[1]This denotes the design luminosity at Atlas and CMS.

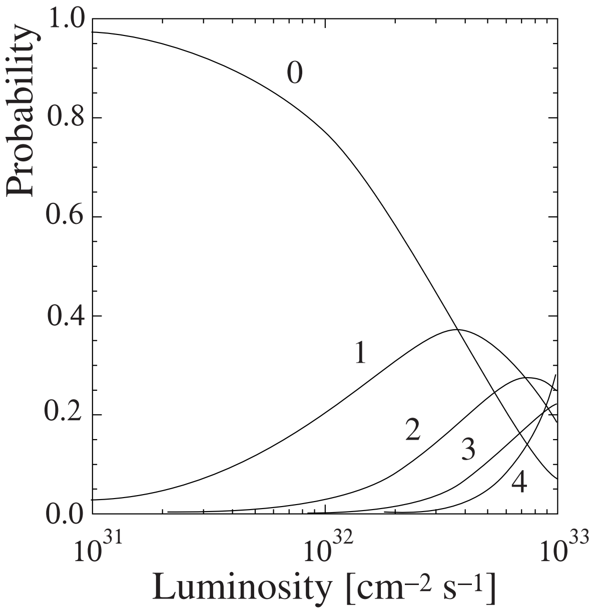

Figure 2.2: *Probability of pp interactions as a function of luminosity. Curves are shown for 0,1,2,3 and 4 pp interactions [36].*

The number of *pp* interactions that occur in a single bunch crossing is distributed according to Poisson statistics. The probability $P(n, \mu)$ of having n interactions with a mean of μ, is given by

$$P(n, \mu) = \frac{\mu^n}{n!} e^{-\mu}. \tag{2.1}$$

The average number of interactions, μ, is determined by the luminosity $\mathcal{L}$,

$$\mu = \frac{\sigma_{inel} \mathcal{L}}{R_{fill} f_{LHC}}. \tag{2.2}$$

The inelastic *pp* scattering (also referred to as *minimum bias*) cross section at $\sqrt{s} = 14$ TeV is assumed to be 80 mb [36].

Fig. 2.2 shows the probability for a number of interactions as a function of the luminosity. The occurance of multiple interactions per bunch crossing is called *pile-up*. In order to limit the effect of overlapping events as well as ageing effects due to irradiation, the nominal luminosity at the LHCb interaction point is tuned to 2×10^{32} cm^{-2}s^{-1} [36]. At the same time the subdetectors, trigger and data acquisition system are designed to handle a maximal luminosity of 5×10^{32}cm^{-2}s^{-1}. Assuming a $b\bar{b}$ cross section in *pp* collisions of 500 μb [38] at $\sqrt{s} = 14$ TeV, the yearly (10^7 s) yield of produced $b\bar{b}$ pairs will be 10^{12}.

The kinematical distribution of the produced B hadrons depends among others on the production process. Simulations with Pythia predict that B hadrons containing the quarks from a $b\bar{b}$ pair occuring in *pp* collisions show a correlated azimuth angle (θ) distribution. This can be seen in Fig 2.3a. The pseudo-rapidity ($\eta = -\ln(\tan\theta/2)$)

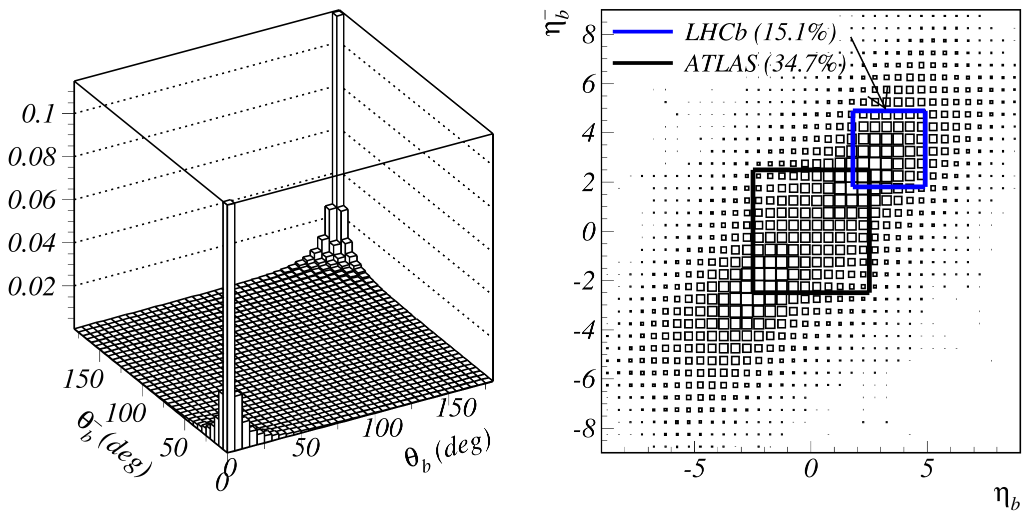

Figure 2.3: *(a) Distribution of the azimuth angle between the two B hadrons in the LHCb detector. (b) Pseudo-rapidity distribution of two b-hadrons. The acceptances of LHCb and ATLAS are superimposed. Figures from [39].*

distribution of the B hadrons is shown in Fig. 2.3b. Although the acceptance of the LHCb detector covers only $1.8 < \eta < 4.9$, 15% of the $b\bar{b}$ events have both B-hadrons in the acceptance. These kinds of simulations were a motivation to build the LHCb spectrometer with a forward acceptance.

2.2 LHCb spectrometer

The spectrometer consists of a single arm tracking system with a dipole magnet and subdetectors as displayed in Fig. 2.4. In the (horizontal) bending plane of the magnet the outer angular acceptance ranges from -300 mrad to 300 mrad. In the vertical plane the outer angular acceptance ranges from -250 mrad to 250 mrad. In the horizontal plane a region from -15 mrad to 15 mrad is excluded due to the beam pipe, while in the vertical direction the exluded region ranges from -15 mrad to 15 mrad.

A right handed co-ordinate system has been adopted with the z direction along the beamline. The direction of increasing z is called *downstream*, the opposite direction is denoted *upstream*.

The spectrometer has been optimised for triggering on $b\bar{b}$ events and reconstruction of B-decays. The vertex detector has a typical proper time resolution of 40 fs [36]. This is sufficient to measure time dependent B_s oscillations with an oscillation period of about 370 fs [40].

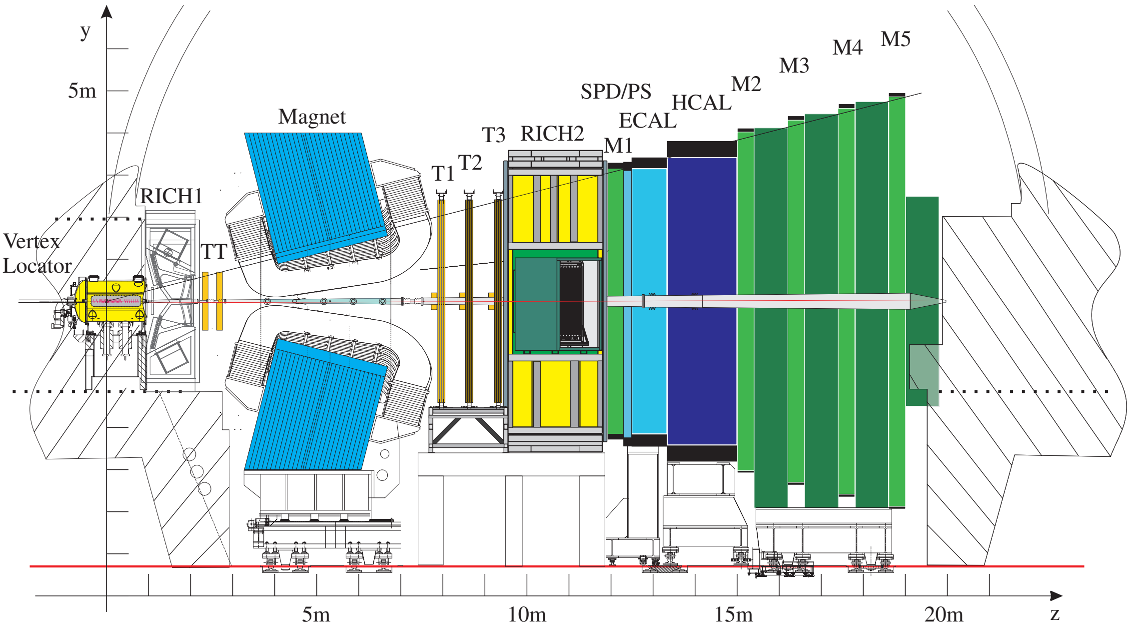

Figure 2.4: *Schematical side view of the LHCb spectrometer. The subdetectors visible are explained in the text.*

The complete tracking system is expected to have a momentum resolution of $\delta p/p \approx 0.4\%$ for momenta from 5 to 200 GeV [41]. This allows for a precise measurement of the invariant mass of B candidates.

Particle identification is facilitated by two Ring Imaging Čerenkov Hodoscopes (RICH), yielding π/K separation over a momentum range from 2 GeV to 100 GeV.

The calorimeter system, consisting of electromagnetic (ECAL) and hadronic (HCAL) calorimeters, is used to trigger on high E_T photons, electrons and hadrons. The preshower detector enables longitudinal segmentation of the ECAL.

Identification of muons is obtained by using 5 separate stations at the end of the spectrometer.

Because of the high interaction rate and the low branching ratio of interesting B-decay processes, an efficient rejection of the data needs to take place. For this purpose a two-part trigger system is built, consisting of a hardware based trigger (Level 0) and a pure software based trigger (High-Level Trigger).

In what follows each part of the spectrometer and the trigger system are described more extensively.

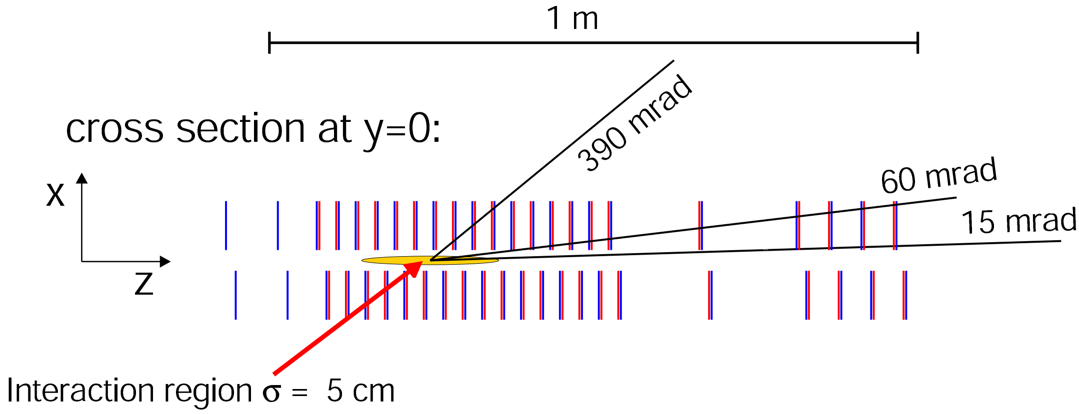

Figure 2.5: *Schematical top-view of the Vertex Locator, with superimposed acceptance limits explained in the text.*

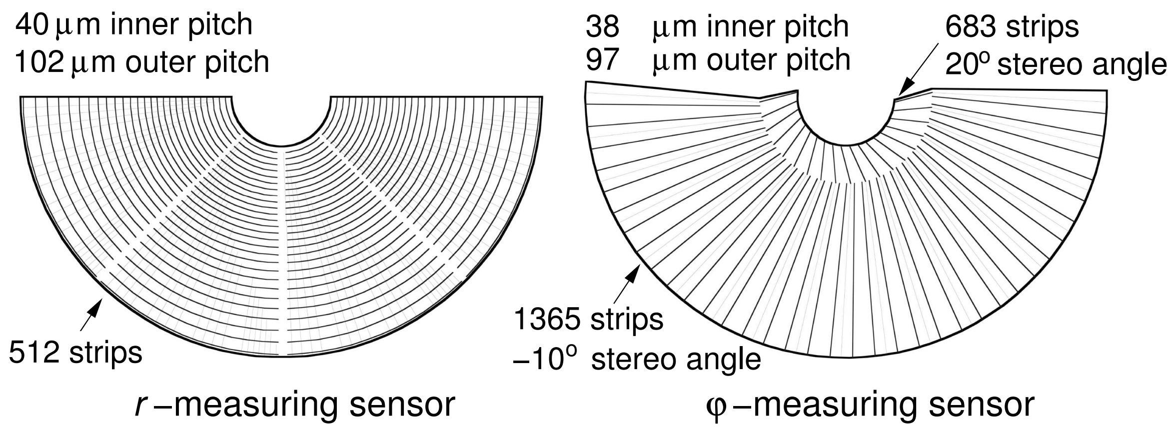

Figure 2.6: *Schematical view of the Vertex Locator r-type and ϕ-type sensors.*

2.3 Tracking system

2.3.1 Vertex Locator

To reconstruct the position of the primary and secondary vertices of the particles, a silicon strip detector, the *Vertex Locator* (VELO) is used. The VELO comprises 23 stations with two measurement layers each. A schematical top-view of the VELO can be seen in Fig. 2.5. The stations close to the interaction point enable to reconstruct tracks with angles up to 390 mrad. The downstream stations allow reconstruction of tracks down to 15 mrad. One of the measurement layers provides the radial co-ordinate (r) and the other the azimuthal co-ordinate (ϕ). The sensors for the azimuthal co-ordinate have a stereo angle of $-10°$ (and $+20°$ in the inner regions) to optimise pattern recognition. The layout of the two sensor types is shown in Fig. 2.6. Two of the 23 stations have a special purpose. These r-type sensors are located upstream from the

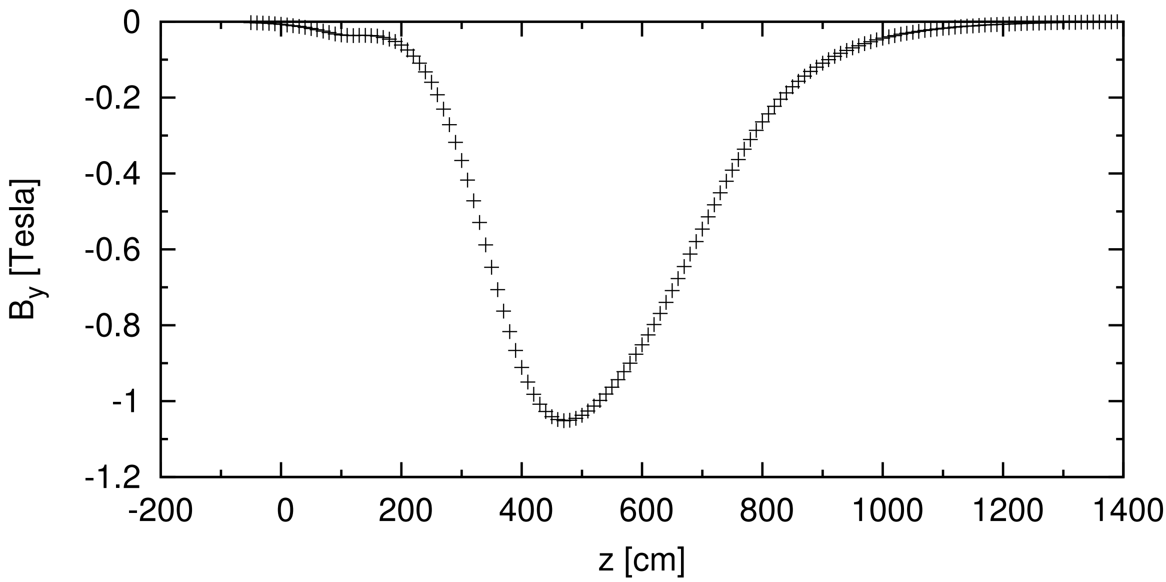

Figure 2.7: *The main field component (B_y) of the LHCb dipole magnet along the z-axis ($x = 0$, $y = 0$) in version 4.7 of the software parametrisation. The markers do not denote any errors.*

interaction point. Their purpose is to provide the Level 0 trigger with information on multiple *pp* interactions.

The sensors are mounted in left and right VELO half detector boxes. These two boxes are placed inside the primary vacuum around the interaction point. During normal operation the inner boundary of the active silicon is just 8 mm from the beamline. To allow safe injection of the beam the two halves of the VELO are retracted to a position 3 cm away from the beam until stable conditions are achieved.

The detector halves are packed in RF shielding boxes to prevent RF pick-up from the passing particle bunches. The shielding box also acts as a border between the primary (beam) and secondary (detector) vacuum. [42]

The sensors are made of n-type strips on n-bulk silicon with a thickness of 300 μm. The strip pitch is adjusted to the expected particle fluxes with a smaller pitch on the inside of the wafers. The r-type sensors have a strip pitch ranging between 40 μm on the inside and 103 μm on the outside, while the pitch of the ϕ type sensors varies between 38 μm on the inside to 97 μm on the outside [43].

2.3.2 Magnet

To measure the momentum of charged particles they are tracked across a dipole magnet. In the LHCb spectrometer a warm magnet is used with the main component in the y direction. In Fig. 2.7 this component is shown along the z axis on the line $x = 0$, $y = 0$. The total integrated field is on average 4 Tm (for 10 metre tracks) with a deviation of 5% depending on the path through the magnet [44]. To minimise systematic effects due

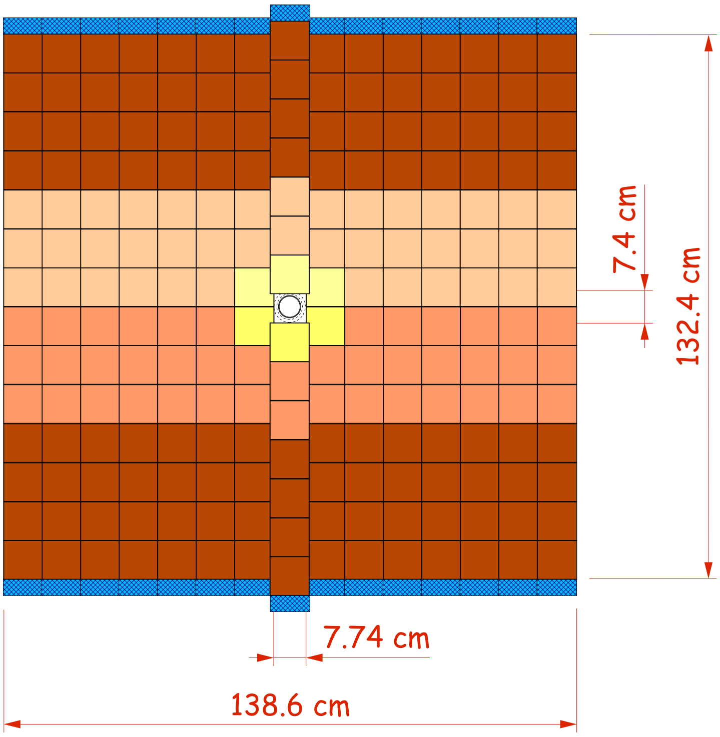

Figure 2.8: *Layout of the upstream x-layer in the silicon tracker station TTa. The strips on sensors with equal shading are connected in series in vertical direction to a single readout channel.*

to a detector asymmetry, the field polarity will be alternated periodically.

With an angular acceptance of 300 mrad in the horizontal plane and 250 mrad in the vertical plane, the magnet adheres to the main LHCb acceptance. The momentum resolution that can be obtained assuming a spatial resolution of the tracker of 200 μm, is better than 0.5% for momenta up to 150 GeV [44].

2.3.3 Silicon tracker

At the upstream side of the magnet a silicon tracker is located between the VELO and the magnet: the Tracker Turicensis (TT). The TT and VELO provide information for a crude momentum estimate which can be used at an early stage of a trigger algorithm. Furthermore, the TT provides a precise measurement of a trajectory at the entrance of the B-field and improves the final momentum measurement. Another objective of the TT is to reconstruct long-lived neutral particles that decay outside the acceptance of the VELO.

The TT is composed of two stations (TTa and TTb) each comprising two layers. The first and the fourth layer have strips oriented vertically, measuring the x co-ordinate. In the second, u, and the third, v, layer the strips are oriented with an angle of $+5°$ and

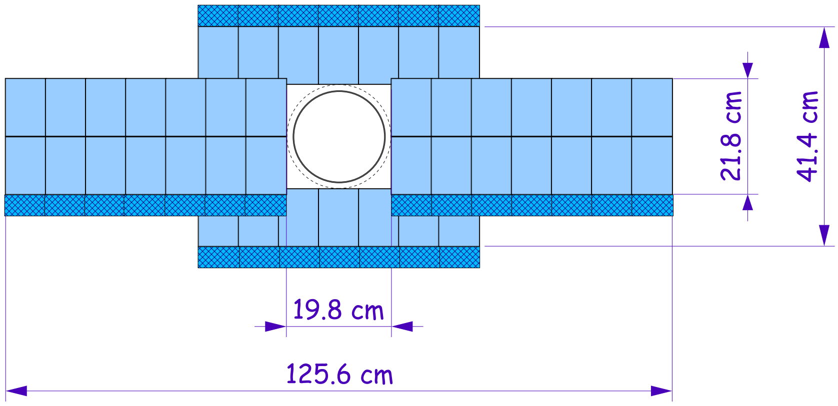

Figure 2.9: *Layout of the inner tracker sensors in one x-layer. The sensors are located in four boxes around the beampipe in the middle.*

$-5°$ perpendicular to the yz plane[1]. The layer pairs xu and vx are separated by a gap of 30 cm.

The p$^+$-on-n silicon sensors are grouped into ladders which are placed around the beampipe as shown in Fig 2.8. The microstrip sensors themselves have dimensions 96 $\times$ 94 mm^2 and contain 512 strips with a pitch of 183 μm.

The strips of neighbouring sensors on a ladder are connected to share a single read-out. Connecting many sensors increases the capacitance per read-out channel leading to an increase of noise. To ensure a high signal-to-noise ratio silicon with a thickness of 500 μm is used [41].

2.3.4 Inner tracker

Due to the forward production of B mesons the highest flux densities will occur in the region close to the beam pipe. To ensure good pattern recognition the occupancy[2] must be kept low. Hence there is a need for a fine-grained detector in this region provided by a silicon detector; the Inner Tracker (IT).

The IT consists of silicon micro-strip sensors which are contained in four boxes placed in a cross-shape around the beam pipe, as can be seen in Fig. 2.9. Each box contains four layers of silicon sensors ordered in similar ($xuvx$) fashion as TT.

The silicon sensors of the IT are interconnected like the sensors of the TT. However since the length of the ladders in the IT is much smaller the signal to noise ratio is larger. This means that where 500 μm silicon sensors are used in the TT, the IT detectors single-sensor ladders have a thickness of 320 μm and those on double-sensor ladders have a thickness of 410 μm.

[1]A positive rotation means viewing in the direction of positive z (downstream) an anti-clockwise rotation, which is positive in a mathematical sense.

[2]Occupancy is defined as the ratio of the number of hit detection channels and total number of channels.

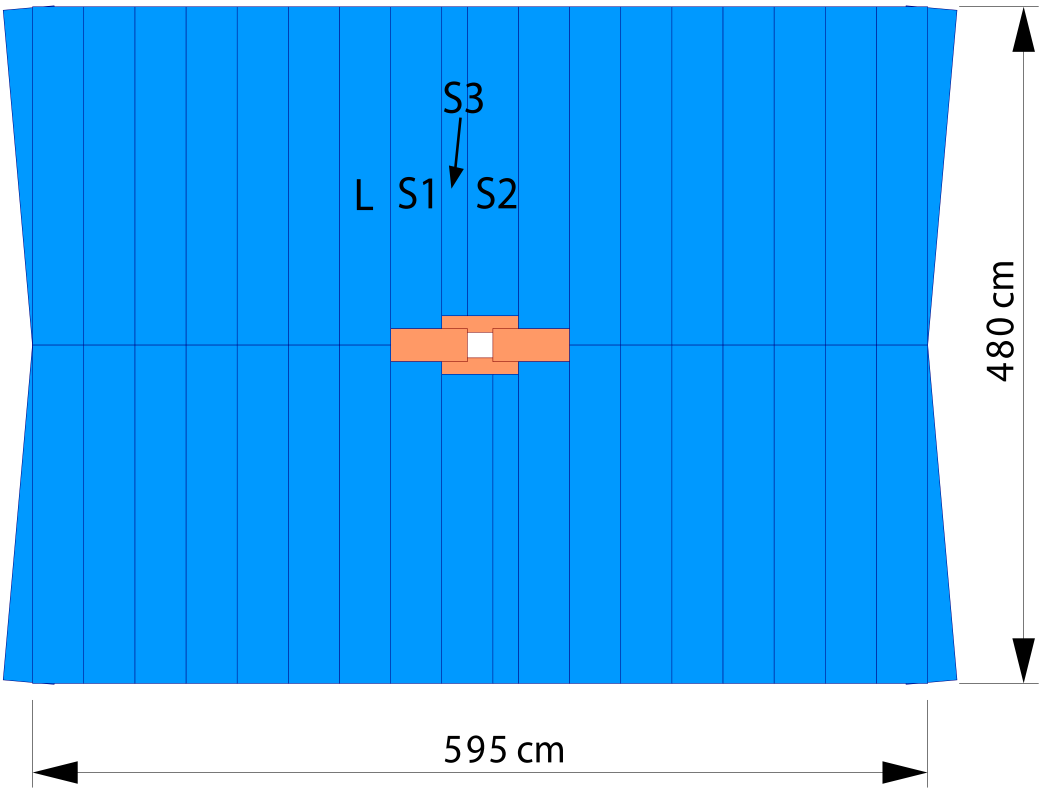

Figure 2.10: *Layout of the outer tracker modules inside one station. Different types of modules (L, S1, S2 and S3) were used to accomodate for the IT (displayed with a lighter colour) and the beampipe opening.*

The ladders are staggered in the z direction with a small overlap between neighbouring sensors. The sensors themselves are divided in strips with a 200 μm pitch. Charge sharing allows a nominal resolution of 55 μm[45].

2.3.5 Outer tracker

The outer tracker (OT) is located behind the magnet and consists of drift tubes assembled in modules. The OT covers 99% of the detector area used for tracking in this region.

One outer tracker module consists of four double-layers of straw tubes. A double-layer is built up of overlapping staggered straws as is depicted in Fig. 2.11 to avoid insensitive areas in the detector. Similar to TT and IT the four double-layers are assembled in an $xuvx$ ordering in downstream direction. A number of 128 straws are grouped into individual modules which are placed adjacently to one another, taking into account an opening for the IT and the beam pipe. Fig. 2.10 shows the module layout in an outer tracker station.

A drift tube of the outer tracker is assembled with a high carbon loaded polyimide

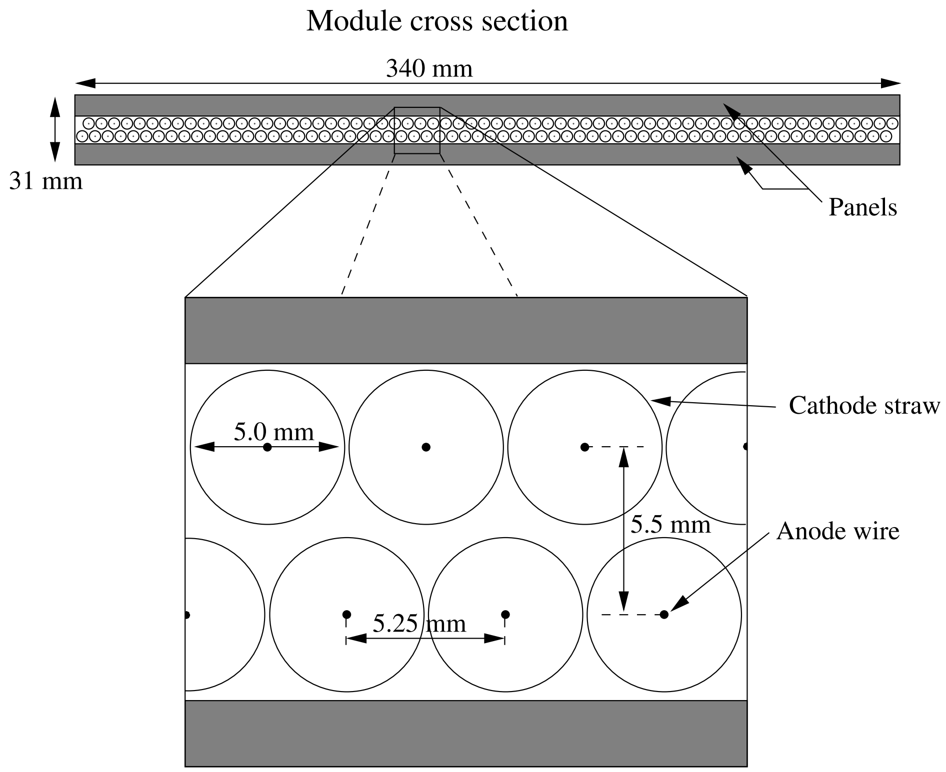

Figure 2.11: *Staggering of straws within one layer of the OT.*

film (Kapton® XC) wrapped with aluminium as the shell of the straw tube. The aluminium acts as a shielding between neighbouring channels. The central wire is a gold plated tungsten anode with a diameter of 25μm. The tubes itself have an inner diameter of 5.00 mm and are placed with a pitch of 5.25 mm in the modules.

The drift gas used in the straws is a mixture of 70% Argon and 30% CO_2. There is an option to add a different mixture if this turns out to be desirable. The drift-time spectrum in this gas mixture has a width of 42 ns, as measured in a test beam experiment [46]. As the time between bunch crossings at the LHC is 25 ns, this means that there is an overlap in the drift-time spectra of previous and next events, the *spill-over*. In a 75 ns readout window, the average spill-over contribution in a $b\bar{b}$ event due to N_{so} spill-over hits in an event with N_{cur} hits due to the current interaction is $f_{\mathrm{so}} = N_{\mathrm{so}}/(N_{\mathrm{cur}} + N_{\mathrm{so}}) \approx 29\%$ [47].

A time-to-digital converter (TDC) readout provides drift-times with a precision corresponding to a spatial cell resolution of around 200 μm [46] and leads to a momentum resolution of about 0.4%.

The efficiency of a single straw tube depends on the ionisation properties of the gas, the HV settings and the discriminator threshold in the read-out electronics. One can parametrise the single cell efficiency as [48]:

$$\eta(l) = \eta_0(1 - e^{-\rho l}), \tag{2.3}$$

where l is the path length of the particle traversing the straw $l = 2\sqrt{R^2 - r^2}$, R is the inner radius of the straw, and r is the shortest distance between particle trajectory and anode wire. The parameter ρ is an effective ionisation density, and η_0 denotes an overall efficiency factor. Test beam data have provided values $\rho = 1.47\text{mm}^{-1}$ and $\eta_0 = 0.99$, representing an average cell resolution of 97% [48].

2.4 Particle identification

Particle identification (PID) is used in the LHCb experiment to distinguish different B-decays with identical topology. Examples are $B \to \pi\pi$ versus $B \to K\pi$, or $B \to D_s\pi$ versus $B \to D_sK$. These events are topologically almost identical, although they give access to different physics parameters due to the different quark content of the decay products. PID information is used in the trigger to identify different final states and this information is also used in the flavour tagging algorithms.

Several detector systems contribute to particle identification. Two Ring Imaging Čerenkov Hodoscopes (RICH) are installed in the spectrometer; one in front and one behind the dipole magnet. RICH 1 is located in front of the magnet to identify pions and kaons with low momentum ranging from 2 GeV to 50 GeV. RICH 2 is located behind the magnet and is used to identify higher momentum pions and kaons in the momentum range 4.4 GeV up to 100 GeV. Both detectors are depicted in Figs. 2.12(a) and 2.12(b). The calorimeters extend the PID information by identifying electrons, hadrons and photons, while muons are primarily identified using the muon chambers.

2.4.1 RICH system

A RICH detector works by virtue of the Čerenkov effect. A charged particle radiates photons when traversing a dielectric medium at a speed higher than the macroscopic light speed in that medium. The charged particle emits radiation in a cone at a specific polar angle, the Čerenkov angle:

$$\cos\theta_c = \frac{1}{\beta n}. \tag{2.4}$$

Here θ_c is the Čerenkov angle, β is the ratio of the velocity of the particle to the speed of light and n is the index of refraction of the medium. (2.4) illustrates that only particles with velocities above a certain threshold $\beta_t > 1/n$ will radiate. Hence to cover a wide velocity (momentum) range there is a need for multiple radiator materials with different indices of refraction.

LHCb uses two RICH detectors with different radiators to obtain sensitivity in a large momentum range. The first Čerenkov counter (RICH1) uses silica aerogel and C_4F_{10}. The second RICH uses CF_4. Table 2.2 gives the relevant parameters of the radiators used in the RICH detectors.

At high velocities β approaches 1 and the Čerenkov angle becomes saturated to $\cos\theta_{max} = 1/n$. As a consequence for high momenta all particle types radiate with the same Čerenkov angle and particle separation is no longer possible.

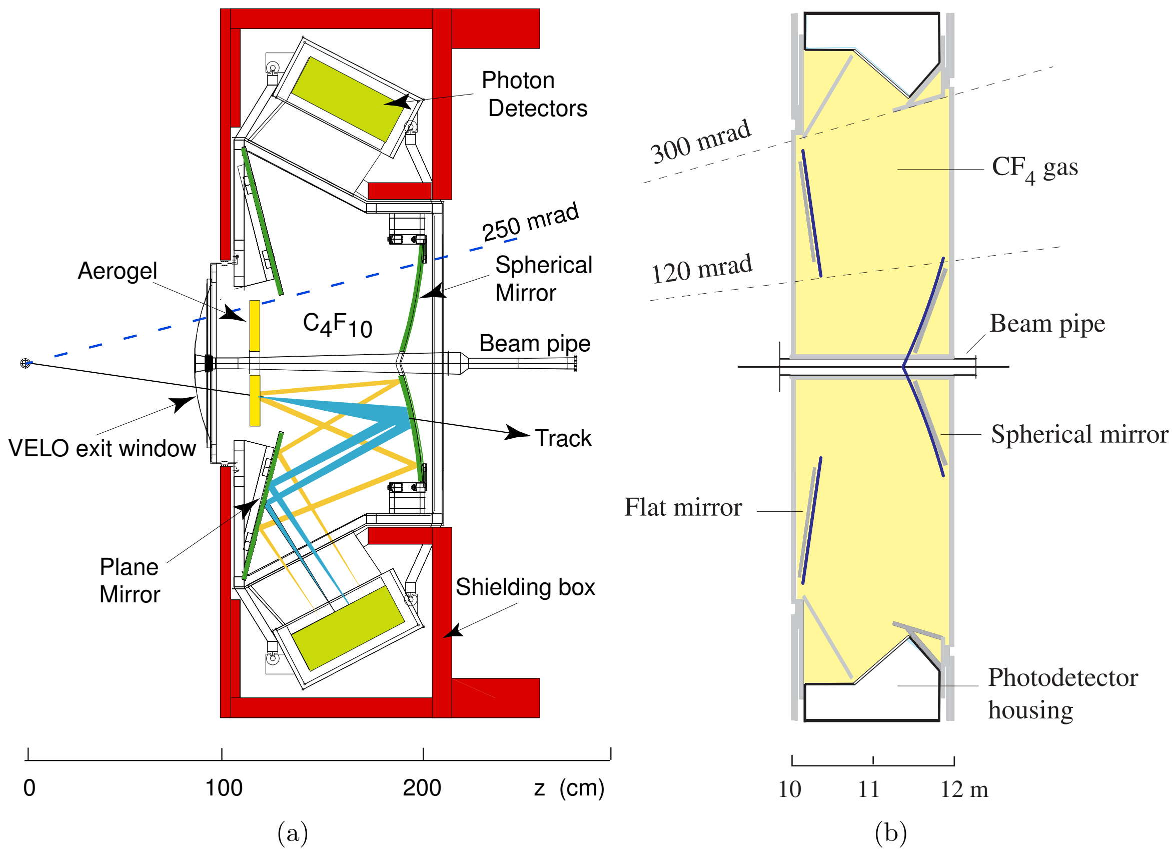

Figure 2.12: *(a) Layout of RICH 1 located before the magnet. (b) Layout of RICH 2 located behind the magnet.*

Radiator	n	$p_{\rm th}(\pi)$(GeV)	$p_{\rm th}(K)$(GeV)	$p_{3\sigma}$(GeV)
Aerogel	1.03	0.6	2.0	10
C_4F_{10}	1.0014	2.6	9.3	50
CF_4	1.0005	4.4	15.6	$\sim$ 100

Table 2.2: *Radiator properties of the RICH detectors [49]. The rows indicate the type of radiator. The threshold momenta p_{th} for which a π or K starts to radiate is given in columns three and four. The last column indicates the highest momentum for which separation of kaons and pions can still be achieved to 3σ.*

RICH1 allows for positive kaon identification for momenta above 2 GeV and 3σ K/π separation up to about 50 GeV [41]. RICH2 can achieve a 3σ K/π separation up to momenta of 100 GeV [49].

2.4.2 Calorimeters

Hadrons, electrons and photons are identified by measuring their deposited energy and impact position in the calorimeter system. Calorimeter signals of high transverse-energy hadrons, electrons and photons are used in the Level-0 trigger. Electron identification is used in tagging semileptonic decays. The electromagnetic calorimeter has been optimised for the ability to identify prompt photons and photons from a neutral pion, by requiring a clear separation of the two photon showers from the pion [50]. A fast and efficient response is needed for the inclusion in the L0 trigger.

A calorimeter detects an incident particle by absorbing all of its energy. The energy is lost via various processes. Photons and electrons interact via electromagnetic processes. Hadrons interact via nuclear interaction processes.

The calorimeter system consists of an electromagnetic calorimeter (ECAL) followed by a hadron calorimeter (HCAL). In addition a preshower detector (PS) and scintillator pad detector (SPD) are located in front of the calorimeters providing longitudinal segmentation for the ECAL. This aids separation of electrons and pions.

Both the SPD and PS consist of 15 mm thick scintillating pads. The SPD and the PS are separated by a 12 mm thick lead wall. Collection of light in the scintillators is facilitated by wavelength-shifting fibers which carry the light to photomultiplier tubes. Electron/pion separation is based on the fact that electrons produce a shower that starts in the lead absorber with a bulk of secondary particles leaving the lead and reaching the scintillator of the PS, thus inducing a signal that is much larger than a typical signal from a minimum ionising hadron [51].

The ECAL has a 'shashlik' structure in which 2 mm lead sheats are interleaved with 4 mm thick scintillator plates perpendicular to the beam. The scintillation light is collected by wavelength shifting fibres that lead it to photomultiplier tubes. The ECAL has an energy resolution[3] of $\sigma(E)/E = 9.5\%/\sqrt{E} \oplus 1\%$ [51].

The HCAL has a similar structure, only the plates are parallel to the beam axis. Instead of lead, iron plates are used with a thickness of 16 mm with an average 4 mm of scintillator in between. For the HCAL the energy resolution obtained is $\sigma(E)/E = (79.2 \pm 2.9)\%/\sqrt{E} \oplus (10.11 \pm 0.45)\%$ [51].

The ECAL has a thickness[4] of 25 X_0. The HCAL has a thickness[5] of 5.6 λ_I, with the addition that the ECAL in front of it has a nuclear interaction length of $1.2\lambda_I$ [51]. Both calorimeters have a lateral segmentation shown in Fig. 2.13 which is optimised for the expected particle flux density distributions [51].

2.4.3 Muon chambers

Muons are present in the final states of several possibly CP violating decays, among which $B^0 \to J/\Psi(\mu^+\mu^-)K_S$, $B^0 \to J/\Psi\phi$ as well as rare decays such as $B_s \to \mu^+\mu^-$and $B^0 \to K^*\mu^+\mu^-$. In addition, muons of semi-leptonic B-decays can be used as a flavour

[3]Here $\oplus$ designates addition in quadrature.
[4]X_0 is the radiation length of the material.
[5]λ_I is the nuclear interaction length of the material.

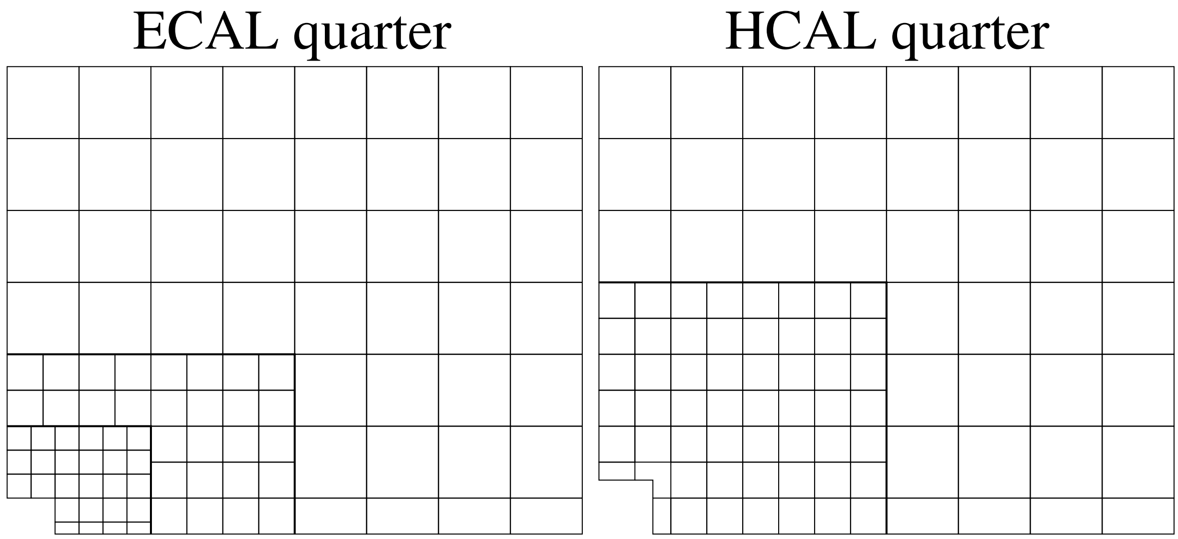

(a) (b)

Figure 2.13: *Lateral segmentation of the (a) ECAL and (b) HCAL to accomodate the flux density distributions. One quarter of the detector front face is shown. The ECAL properties: Inner section with 40.4 mm cells and 1472 channels, middle section with 60.6 mm cells and 1792 channels and outer section with 121.2 mm cells and 2688 channels. The HCAL properties: Inner section with 131.3 mm cells and 806 channels and outer section with 262.6 mm cells and 608 channels.*

tag, providing the initial flavour of neutral B mesons. As the muon information is used in the Level-0 trigger, a fast response is mandatory.

Five tracking stations are positioned at the downstream end of the spectrometer to identify the muons. The first muon station, M1, is placed before the preshower detector of the calorimeter to provide a large lever arm for a transverse momentum measurement of a muon track. To attenuate hadrons, electrons and photons, the four remaining muon stations are interspersed with thick sheets of iron, the so-called muon filters [52].

Due to the fluence rate distribution in the muon chambers, a tracking chamber consists of four different regions. For most regions the rates are sufficiently low to have multi-wire proportional chambers (MWPCs) [53]. For the inner region of M1 with the highest charged particle flux densities around 460 kHz/cm^2, triple gas-electron multiplier (GEMs) detectors have been opted for [54]. Furthermore the segmentation in regions, sectors, channels and logical pads of a muon station is optimised for expected particle fluxes, as is visible in Fig. 2.14. The x dimensions of the logical pads in stations M1 to M3 are determined primarily by the precision required to obtain good muon p_T resolution for the Level-0 trigger. The y dimensions of the pads in all five stations are required by rejection of background triggers which do not point to the interaction region [52].

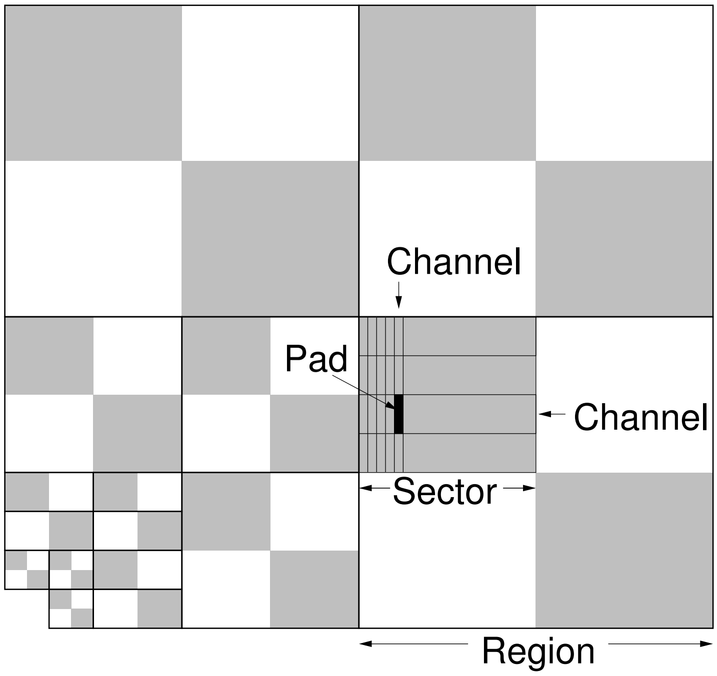

Figure 2.14: *Lateral segmentation of one quadrant of muon station M2 to accomodate the flux density distributions. Regions (indicated by thicker lines) are subdivided in sectors (depicted in different shades), which contain horizontal and vertical strips corresponding to logical channels. Intersecting channels form logical pads. The sizes of the structures can be found in [52] and differ per muon station. The size of a muon station ranges from 7.7×6.4 m^2 to 11.9×9.9 m^2 (M1 to M5).*

2.5 Trigger and DAQ

At a luminosity of 2×10^{32} cm^{-2}s^{-1} at a bunch crossing frequency of 40 MHz only 10 MHz of crossings will have visible interactions. The trigger reduces the event rate down to 2 kHz.

The trigger is based on a two-part system. The first level, trigger Level-0 (L0) is implemented in hardware. It incorporates limited information from the subdetectors to select particles with large transverse momenta above about 1-2 GeV. The event rate reduces from 10 MHz to 1 MHz. The separate L0 triggers listed below are combined in the L0 decision unit (L0DU).

After a positive decision by the L0DU, the data from the subdetectors is collected by the data acquisition system (DAQ). Zero-suppressed data from the front-end electronics of each of the detectors is collected and assembled into complete events. This data is subsequently used in the HLT [55].

The high level trigger (HLT) is implemented in software that runs on an event-filter farm. The output of the HLT is sent at an event rate of 2 kHz to mass storage for offline analysis [56].

2.5.1 Level 0 trigger

The Level-0 trigger has three main goals: Firstly the selection of high E_T particles (hadrons, electrons, photons, neutral pions and muons), secondly, the trigger should reject complex or busy events which take longer to reconstruct, thirdly, L0 should reject beam-halo events.

The level-0 pile-up veto system

The pile-up veto of the VELO detector consists of two silicon planes positioned upstream from the nominal interaction point. It provides rejection of events by identifying bunch crossings with multiple primary vertices. Two global event variables are output to the L0DU: the number of tracks from the second vertex in the event and the hit multiplicity in the pile-up detectors.

The level-0 calorimeter trigger

The calorimeter system provides candidate hadrons, electrons, photons and neutral pions with high transverse energy. The transverse energy is measured in the ECAL and HCAL from energy deposits in clusters of 2×2 cells. SPD and PS deliver charge information of the clusters. The calorimeter system provides the L0DU with highest E_T hadron, electron, photon and π^0 candidates, the total HCAL E_T and the hit multiplicity in the SPD. The π^0 trigger has two thresholds: a "local" threshold which sums the energy in an 8×4 calorimeter cell area and a "global" threshold where an area of double size is used [57].

The level-0 muon trigger

Muons are searched for in each quadrant of the muon stations. The L0 algorithms for the muon trigger estimate the transverse momentum assuming the candidates originate in the primary vertex. The two highest p_T muon candidates from each quadrant are sent to the L0DU.

L0 Decision Unit

Data is collected from all the subdetectors. The thresholds for the sub-triggers are given in Table 2.3. The event is accepted if any threshold in Table 2.3 is passed and if the event passes all the global event thresholds listed in Table 2.4. If the sum of transverse momenta of the two highest p_T muons (Σp_T^{μ}) exceeds 1.3 GeV the event is accepted ignoring any global threshold. The Level-0 trigger is foreseen to have a fixed latency of 4 μs [57].

2.5.2 High level trigger

The events that are accepted in the L0 trigger pass to the high level trigger at a rate of 1 MHz. The HLT includes a dedicated set of algorithms combined into *alleys* that refine

Particle	E_T Threshold (GeV)
hadron	3.6
electron	2.8
photon	2.6
π^0 local	4.5
π^0 global	4.0
muon	1.1
$\Sigma p_{\mathrm{T}}^{\mu}$	1.3

Table 2.3: *Level-0 trigger thresholds for various particles [57].*

Threshold type	Global threshold
Tracks in 2$^{\text{nd}}$ vertex	≥ 3
Pile-Up Multiplicity	< 112 hits
SPD Multiplicity	< 280 hits
Total E_T in HCAL	≥ 5.0 GeV

Table 2.4: *List of Level-0 trigger restrictions for global event variables [57].*

the L0 trigger information using subdetector data. The HLT features a muon alley, a muon plus hadron alley, a hadron alley and electromagnetic lines. This is visualised in Fig. 2.15. The different HLT alleys can be triggered by a specific L0 algorithm or by a previous HLT alley. In the trigger alleys, a partial event reconstruction is performed. The full reconstruction is done only at the end of the alleys. In what follows the HLT alleys are briefly described, more extensive descriptions can be found in [56] and [58]. A new HLT structure is being set up which splits the HLT in two parts and instead of alleys uses HLTLines [59]. This evolution of the trigger was done mostly after the time of writing of this thesis and is hence not included here.

Muon alley

Events that have been accepted by the L0 muon trigger pass on to the HLT. Here a better momentum resolution close to 1% is obtained by including the most downstream T tracking stations. VELO detector information is used to determine an impact parameter.

If two muon candidates are found with an invariant mass above 2.5 GeV the event is sent to storage. Furthermore if the invariant mass is above 0.5 GeV and the impact parameter is above 100 μm the event is accepted. Events with a single muon pass the muon alley if $p_T > 3.0$ GeV and an impact parameter significance $\mathrm{IP}/\sigma_{IP} > 3$ [56].

Muon and hadron alley

When the L0 trigger has been activated by a muon candidate but the HLT muon alley has not accepted the event, it is run through the muon and hadron alley. The strategy is to select events with a muon and a hadron track with a high impact parameter and high p_T, and the muon by itself does not have enough transverse momentum to trigger the muon alley.

Hadron alley

The hadron alley is triggered by a hadron event in L0. The HLT will reconstruct straight line VELO tracks and select them if the impact parameter is larger than 150 μm. A

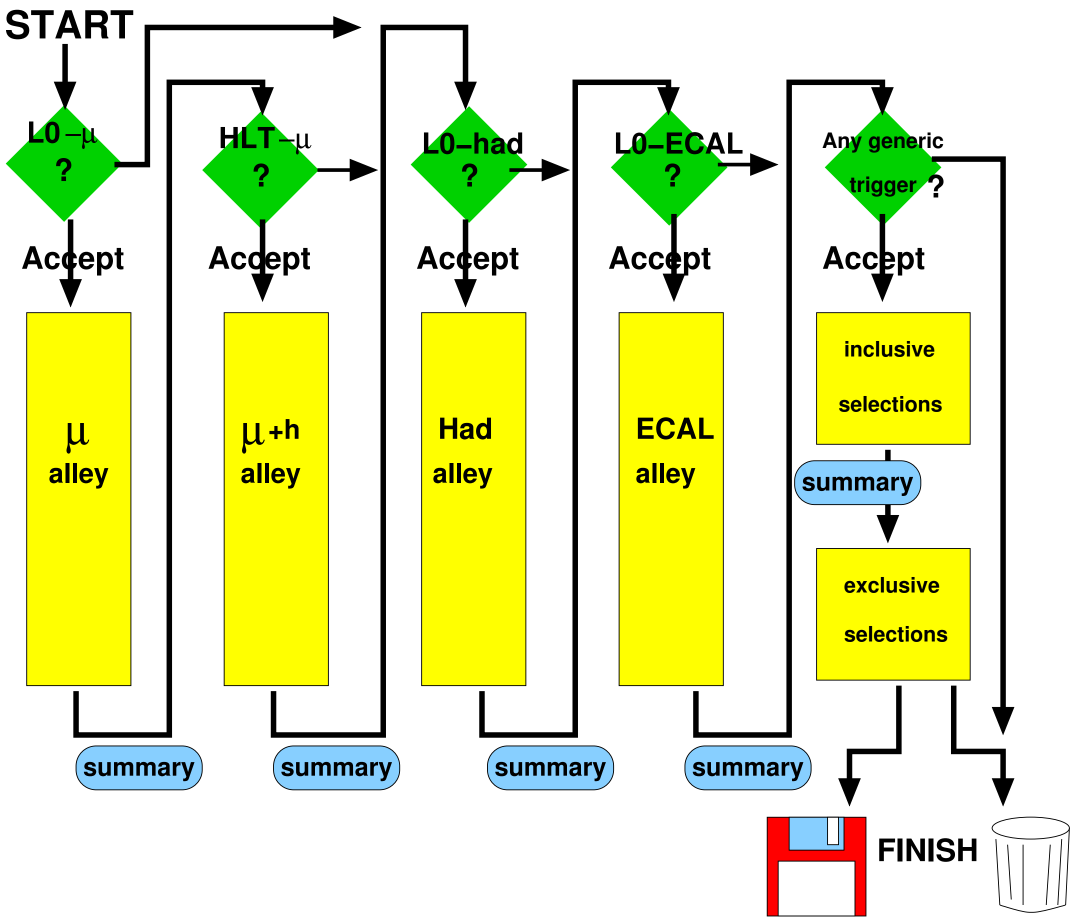

Figure 2.15: *Alley structure of the high level trigger. The text explains the whole structure and the separate alleys.*

momentum estimate is made with hits from the TT station. A minimum p_T of 2.5 GeV is required for a single hadron.

Electromagnetic alley

Level-0 electron and photon candidates are first confirmed in this stage. For the photon candidate, it is foreseen to demand in addition a high-p_T hadron with a large impact parameter in the same event.

Inclusive and exclusive selections

The combined output rate of all the alleys is less than 10 kHz which is low enough to perform a reconstruction of the remaining tracks. Hence the inclusive and exclusive reconstruction algorithms are run at the end of the alley structure.

Several tracks are selected with very loose restrictions on their momentum and impact parameter and subsequently composite particles are constructed.

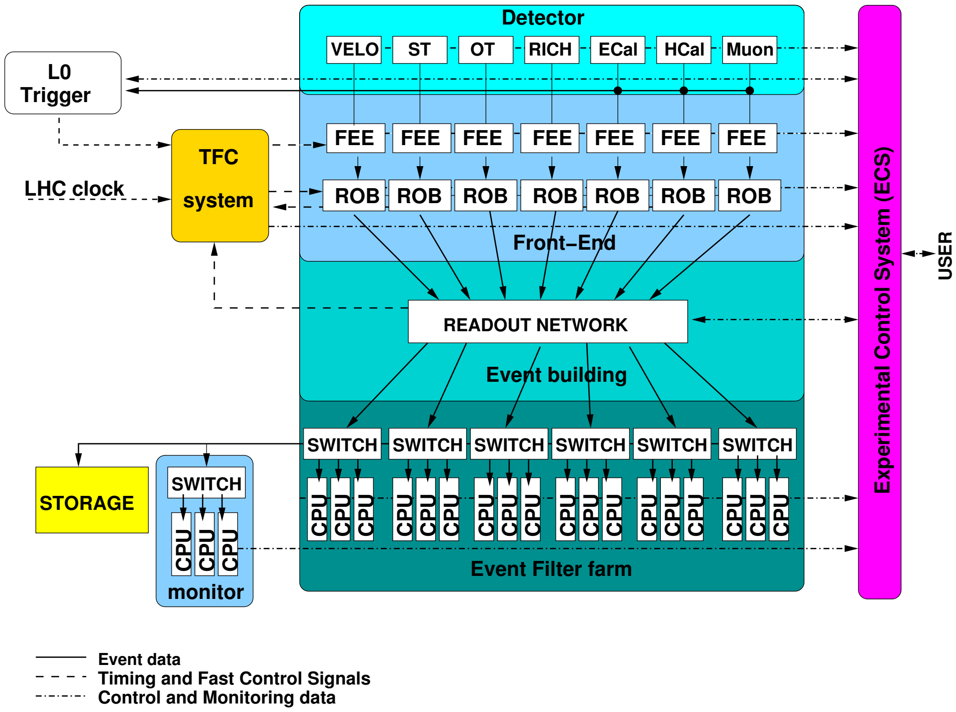

Figure 2.16: *A general overview of the data acquisition system. The detector data runs from the subdetectors to the front-end electronics (FEE) to the readout boards (ROB) and is built to events which are distributed by a readout network to the event filter farm.*

After the inclusive triggers a few exclusive selections are also run to select specific B-meson decays to reduce the output event rate. An example of an exclusive reconstruction is $B \to \pi^+\pi^-$. Here two tracks are selected requiring a good vertex and an invariant mass in a range around the B mass. The output event rate of the exclusive selections is projected to amount to 200 Hz. The total HLT output rate is expected to be 2 kHz at which the data is written to storage.

2.5.3 Data acquisition system

To collect the data from the front-end (FE) electronics of each subdetector as well as monitor the experimental systems an online data acquisition (DAQ) and experiment control system (ECS) has been developed [55]. A overview of the DAQ system is shown in Fig. 2.16.

After a L0 trigger the DAQ should provide the data from the electronics to the HLT running on the processor farm. The collection of data from the FE electronics to the farm is done by a dataflow subsystem. It consists of a *readout unit* which multiplexes the data from the FE links and passes them to a *readout network*. This network routes the event fragments to an event builder on a sub-farm, after which they are transmitted to the main CPU farm which runs the HLT algoritms.

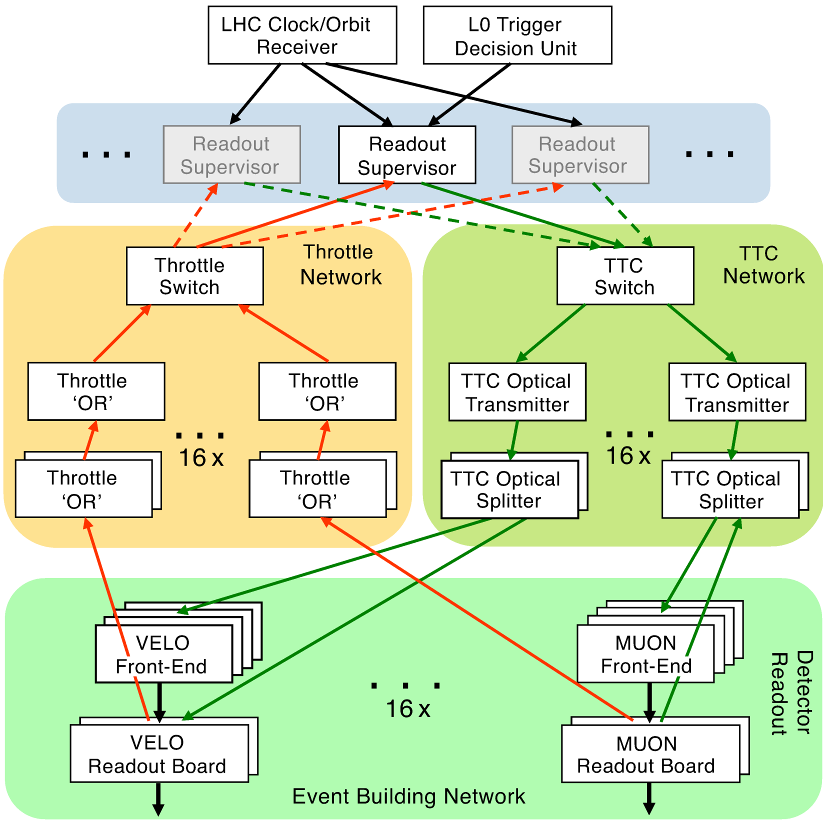

Figure 2.17: *The Timing and Fast Control system used to distribute trigger and clock signals.*

The distribution of the trigger and clock signals is achieved by a timing and fast control (TFC) system which is shown in Fig 2.17. The data from the detectors is stored synchronously in derandomizer buffers (not shown), to account for minor differences in trigger times. The TFC is controlled by a readout supervisor which receives the LHC bunch clock and the L0 triggers. When the buffers should overflow the readout supervisor can send a throttle signal to reject trigger signals. To ensure a fully synchronous dataflow, event identifiers accompany the trigger decisions.

The experiment control system (ECS) controls, configures and monitors the detector hardware. It receives status information from the accelerator, safetly system and technical services. It sends information about the detector to a conditions database. To enable a safe running detector data is also transmitted to the safety system and accelerator services. Detectors can be configured by the operator through the ECS.

3

Software environment

Since LHCb is not yet operational, all the events are produced via Monte Carlo simulations. The simulations were used in the detector design phase to give insight in what the performance of LHCb will be. Furthermore they are an important tool for the development of tracking algorithms and the study of parameter sensitivities of each analysis technique.

There are several stages in simulating the data. All the stages are written in C++. Except for the event generation, the programs rely on a common framework, GAUDI. GAUDI provides the basis for several user made *algorithms* and *tools* that use common *services* to produce and analyse data in LHCb. In this chapter the programs that are involved in event generation, detector simulation, hit digitisation, track reconstruction and event analysis will be described.

3.1 Gaudi framework

The GAUDI framework provides features that enable flexible processing of data. GAUDI decouples the objects describing the data and the algorithms that act on it [60]. The data objects are described in the LHCb event model. The actual data transformations are performed by tools and algorithms. These run in the various applications for event generation and detector simulation (GAUSS), digitisation (BOOLE), reconstruction (BRUNEL) and analysis (DAVINCI).

In a task of event simulation, reconstruction and analysis the manipulation of data objects such as momenta, clusters, matrices and tracks is done by algorithms. In these tasks a natural distinction between data and code is made. For this reason in the GAUDI framework this distinction is also made with data objects, and algorithms and tools. The algorithms and tools are configured through job options, which can be set at run-time.

3.1.1 Data

The data objects which are used during a reconstruction or analysis job will usually be used among different algorithms and tools. Only at the end of the job will the data be processed in a final format. GAUDI discerns data which is used between the algorithms and tools, the *transient data* and the data which is written to disk at the end of the job which is *persistent*.

Three distinct uses of transient data are available in the GAUDI framework. *Event data* which is obtained in (real or simulated) collisions. *Detector data* which describes the detector materials and their positions. Then, there is the *Histogram data*, which can be any statistical data that can be collected during a job. All three types of transient data are stored in different memory locations which have a different lifetime in the job.

The *Transient Event Store (TES)* stores data valid only for the duration of one event. The *Transient Detector Store* contains information like alignment and thus usually has a lifetime of many events. The *Transient Histogram Store* contains statistical data collected during a complete job, hence exists to the end of the job.

The data stores are organised in a tree-like structure so navigation is made easy grouping similar data. Any data in the transient store can be made persistent through a special *service*.

3.1.2 Algorithms and tools

The way data is manipulated in GAUDI is done via an *algorithm*. Usually an algorithm is part of a larger sequence of algorithms which are called in the job through an *application manager*. This way an algorithm can work on the output of a previous one.

Several algorithms might use a common operator on their data. The commonality of an algorithm can be re-used and implemented as a *tool*. Each tool is in essence a light-weight algorithm which can be executed with different frequency inside an other *tool* or *algorithm*.

3.1.3 Services

Common to all GAUDI software are the *services* that provide basic functionality. To parse information to the algorithms a *Job Options Service* is used. Furthermore there is a *Message Service* for the streaming of messages from the applications. The *Event Data Service* allows retrieval and storage of data. Uniformly generated random numbers are provided by the *Random Number Generator Service*. To make transient data persistent a *Conversion Service* can be used. There is a *Histogram Service* to accumulate statistical data. A *Detector Description Service* communicates the structure and geometry of the detector to the algorithms.

3.1.4 Event data model

The LHCb event data model describes the event data and the relationships between reconstructed data and Monte Carlo data.

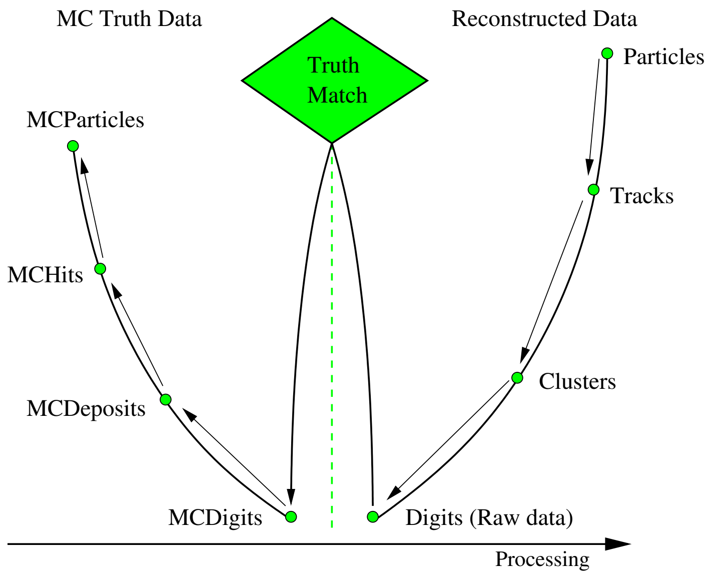

Figure 3.1: *Monte Carlo relations in the Event Data Model [60]*

A particle generates a response signal in the detectors which is digitised. A clustering algorithm determines the digits that belong together and calculates a centre of gravity for each group. The pattern recognition algorithms find the clusters that belong to each other and makes a track.

The Monte Carlo truth information for the tracks can be accessed via the digits which make up a certain track. Event data like particles, tracks, clusters and digits and their Monte Carlo counterparts like MCDigits, MCDeposits, MCHits and MCParticles are connected. The relation between these objects is descibed by *linkers* and *relations*. This description is general for all the detectors. One can see in Fig 3.1 that at the lowest level the digits and MCDigits are directly connected.

3.1.5 Track event model

For the tracking part of the LHCb algorithms there is an additional description to the Event Data Model. The Track Event Model (TEM) describes how tracking information is organised and processed.

The TEM is used in the pattern recognition algorithms and the track fitting. The objects and relations described by the TEM will now be described.

A particle needs to be reconstructed from detector measurements as follows. The pattern recognition delivers a five-dimensional vector (*trackstate*) at several z-positions in the experiment. There are 18 such positions. A state vector can be seen as a straight track segment, it consists of a x and y position, x and y slopes and a momentum estimate. A pattern recognition algorithm also delivers clusters of hits belonging to a track segment, the *measurements*.

To acquire an accurate representation of a track, it will be fitted and processed through a Kalman filter to incorporate multiple scattering. The fitting stage provides *nodes* which link track states to measurements.

A generic way of describing particle tracks, detector elements and their mutual positions is currently being developed in the form of so-called trajectories. However these are not implemented in the TEM that is used in this thesis.

3.2 Event generation: Gauss

The simulation of the spectrometer consists of two phases, the event generation and the detector simulation. The first phase consists of event generation where the standard pythia generator [61] is used in LHCb to simulate the pp collisions. To simulate B hadron mixing and decay a specialised package for b-decays, EvtGen, is used. Both programs are steered through the Gaudi application Gauss. Furthermore Gauss implements the physics of the running conditions such as luminosity changes with the fill lifetime and the smearing of the interaction region due to the sizes of the particle bunches. The luminosity change influences the probability of single to multiple pp collisions, this is also simulated.

In the second phase of the simulation the particles are tracked through the spectrometer. The Monte Carlo history about vertices, decays and scattering is stored. The interaction of the particles with the detector material is simulated with Geant4. Information to and from Geant4 is interfaced by LHCb interfaces (GiGa).

3.2.1 Pythia

Making use of parameterised parton density functions of the proton, pp scattering is simulated. First of all the hard-scattering cross section is calculated. Pythia implements over 300 hard-scattering processes, mainly for 2 to 2 or 2 to 1 parton processes. Parton distributions are parameterised through parton-density functions that have been extracted from experiment as well as some theoretical models. Initial and final state radiation are calculated for pp-interactions mainly through a parton shower algorithm. This is only an approximate way, calculating the shower evolution through the DGLAP equations[1]. Pile-up from multiple interactions is modelled with multiple hard scatterings. The quark fragmentation and hadronisation are calculated by default through the Lund string model: The strong force between the quarks is modelled with a linear dependence on the distance between them in a colour flux tube. A maximal stress is imposed on the flux tube and at the point where it breaks a new pair of particles is produced. The momentum of the initial parton is divided between the two products, $(1-z)$ for one and z for the other, where z is the momentum fraction. This sets the transverse momentum scales for the produced particles. Heavy flavours ($m_q > m_s$) can only be produced in the hard scattering and not in the fragmentation. The decay of the formed state is modelled according to known branching fractions.

[1]DGLAP equations give the splitting probability as a function of initial four momemtum Q^2 of the parton.

The kinematics of the collision are completely taken into account. Heavy flavour production is incoporated in Pythia by three main processes [38]. First, production by the hard scattering. The leading order parton fusion processes are: $q\bar{q} \to b\bar{b}$ and $gg \to b\bar{b}$. Second, flavour excitations $Qg \to Qg$, $Qq \to Qg$ where a heavy quark $Q = b, \bar{b}$ in the sea is brought on mass shell by an other parton. Finally gluon splitting $gg \to gg$ in initial or final state radiation can contibute to heavy quarks. The process $g \to b\bar{b}$ does not occur in the hard scattering, however, it can lead to flavour excitation. At LHC energies flavour excitation and gluon splitting become dominant.

In LHCb there are three general ways of obtaining events with specific beauty hadrons. First a plain pythia can generate events until a correct hadron is found. In addition, *forced fragmentation* and *repeated hadronisation* can be used. The former method uses events where a b-quark is forced to fragment with an associated u,d or s-quark to form the hadron of interest. The alternative, which is preferred since it consumes less time, is repeated hadronisation. In this case the correct signal B-hadron is filtered out of many repeated instances of the b-quark hadronising.

3.2.2 EvtGen

EvtGen is an event generator for the simulation of the physics of B-decays. In contrast to the pythia generator, no kinematical factors and cross-sections have been taken into account[2]. The evolution of the B-mesons is calculated using expressions for mixing and the decay. Specifically EvtGen uses different decay models which can be specified by the user. Each decay product is then subjected to another decay model if necessary. Thus the physics of the decay is simulated by EvtGen upto the final decay products.

The user has to set a specific decay model in which one can incorporate mixing and CP violation. The best way on how to do this is not yet clear. There are several models that describe the mixing, decay, angular distribution and CP violation separately, but a way to combine them is not easy.

Semileptonic decays are also implemented in EvtGen, with the form factors described by several different models. This will be of interest for the semileptonic channel which is investigated in this thesis.

3.3 Detector simulation

The interaction of particles with the detector material is calculated by Geant4. In addition to these processes particle decay in flight is incorporated. There are many different processes that contribute to the interaction of particles with matter. Roughly one can divide them into electromagnetic and hadronic interactions. For a complete overview see the Geant4 physics reference manual [62]. One of the physical effects important for the tracking is multiple scattering. In multiple scattering a particle has multiple coulomb interactions with the nuclei in the detector matter. Multiple scattering in Boole is incorporated via Lewis theory, which is a extention to the Molière-Bethe

[2]Although EvtGen has the possibility to simulate kinematics.

theory on scattering. It models the spatial and angular distributions of the scattered particle.

3.4 Digitisation: Boole

Responses of the detectors are simulated in the digitisation program BOOLE. It uses output files from GAUSS containing events of a specific nature, e.g. minimum bias or specific decay channels.

The detector response, the read-out electronics and the L0 trigger hardware are simulated in this step. Specific for each detector the pulse shape and timing are produced from a simulated particle traversing the active detector material. During the simulation of a particular sub-detector the noise, cross-talk and dead channels are included.

Digits corresponding to the output of the front-end electronics are zero-suppressed and partitioned in banks before going to the data acquisition system (DAQ). The banks are concatenated by the event builder of the DAQ. The resultant buffer is used as input for the HLT trigger. The HLT trigger applications are then run on the zero-suppressed data.

From this point on the MC and the measured data will be treated in the same fashion. The output data can be used to reconstruct tracks.

3.5 Track and PID reconstruction: Brunel

BRUNEL is the reconstruction application of LHCb. The track reconstruction is made using hit-data from the detectors. The input for BRUNEL is the buffer from the DAQ. Track reconstruction can be seen on two levels. First the pattern recognition is used to find the particle tracks. Secondly a track fit is made to determine the track parameters with a good accuracy. The output files in the DST format are used for further physics analysis or event stripping to select specific events. The reconstruction of Monte Carlo data is identical to real data.

The reconstruction proceeds in several phases. First the clustering algorithms are run to produce clusters from the detector digits. These algorithms are specific for each subdetector. Next pattern recognition is performed using the clusters. Then a Kalman filter is used to fit the tracks. Last, a clone killer will remove tracks which share clusters. In the testing of the reconstruction Monte Carlo truth information is used in a checking phase. One can also instantiate a monitoring phase in which statistical data can be gathered in histograms. The final BRUNEL stage outputs an object which has track information but multiple PID information, these objects are called *protoparticles*. In the physics analysis the user can construct one or multiple *particle* objects from a protoparticle by selecting which PID information to use.

3.5.1 Pattern recognition

An important type of Brunel algorithm is a pattern recognition. From the cluster patterns in the subdetectors the tracks are reconstructed. Most pattern recognition algorithms are written specifically for one subdetector or a combination of subdetectors. Both the pattern recognition and the track fit adhere to the Track Event Model. A dedicated track pattern recognition algorithm will be described in chapter 4.

3.5.2 Track fitting

To get the most accurate parameters of a track it must be fitted. The fitting phase also proceeds in Brunel. The fitting procedure consists of a Kalman filter. A Kalman filter [63] is a recursive method for estimating a dynamic state of a system. For a track, consisting of measurements, this means that each measurement is used to update the trackstate. From this state a new prediction is made for the trajectory. At the end of the track the filter procedure is reversed from the last to the first measurement, this is the smoothing step. LHCb uses an extended Kalman filter to linearise any non-linear behaviour of the trajectories due to multiple scattering.

3.5.3 Checking

The checking phase is an important part of the reconstruction. To make sure the pattern recognition is performing well, the results must be checked against the Monte Carlo information. The Event Data Model specifies the relation between Monte Carlo objects and real-world objects. A criterion of a good match is generally accepted as being 70% of the clusters originating from the same MCParticle.

3.6 Physics analysis: DaVinci

To perform event selection and physics analysis, the DaVinci program is used. In DaVinci vertices will be reconstructed and the protoparticles from Brunel are assigned a PID hypothesis using subdetector information. How the vertices are reconstructed from the tracks and which PID information needs to be used, is controlled by the user.

Beside providing tools for a selection of tracks, DaVinci can also provide Monte Carlo truth information to assess whether the reconstruction and selection was efficient.

The selection and analysis algorithms that are written for DaVinci are completely configurable by option files. In this way the user benefits from the flexibility of the selection without having to modify the source code.

The tools used in the selection and analysis are designed to be used on both online and offline data. This allows the same algorithms to run offline as well as in the HLT. This transparency allows the user to rerun an online selection in an offline environment for example with a tampered buffer.

A DaVinci algorithm will write the output in an Analysis Object Data (ntuple) file which can be opened for analysis. One can also opt for a reduced DST file to be produced, which can be subsequently used for further processing.

4

T station pattern recognition

4.1 Introduction

Particles traversing an active detector volume leave information about their trajectory in the form of energy deposits in interactions with the detector material, the *hits*. It is the task of pattern recognition algorithms to link the hits belonging to the same particle into tracks. After the track finding pattern recognition the kinematical properties of the particle are reconstructed by a track fitting algorithm.

Two main approaches to pattern recognition exist. The first approach treats all detector hits in a democratic way, independent of any starting point or processing order. This approach is referred to as a *global* algorithm and an example of such an approach is a Hough transform used in an online algorithm for the T stations [64].

The second approach, used in this thesis, starts from small subsamples of hits called *seeds*, in order to find track candidates. This can be done via extrapolation or interpolation, as is illustrated in Fig. 4.1 for an example with multiple detection layers.

In the extrapolating method seeds are constructed by combining hits in neighbouring layers. Due to the small lever arm, the angular precision of the initial track candidates is low, however the fake rate of wrong combinations may be relatively low since most wrong combinations give a slope that is too steep for a physical track and can be discarded immediately. In the other method seeds are formed by interpolating two hits from the most distant layers. Such seeds have a higher angular precision, but require a larger number of combinations to be made. This costs more processing time, and if the material introduces much multiple scattering the gain in precision can be limited [65].

In the LHCb software repository two more T Seeding algorithms are available. These algorithms [66, 67] both use extrapolation by linking nearby hits to find a complete track candidate. In this chapter a pattern recognition algorithm named *T Seeding* is described that uses interpolation. It is based on a FORTRAN Seeding algorithm [68, 69] and rewritten in an object oriented way. This algorithm is developed to find tracks from hits

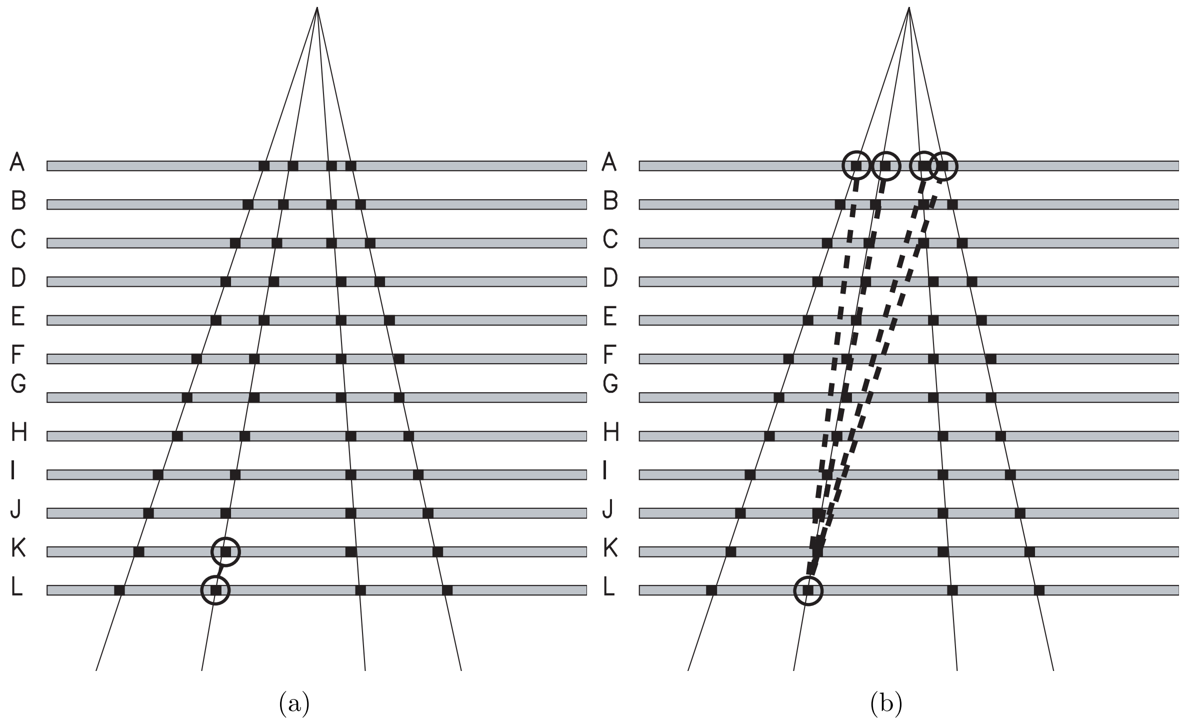

Figure 4.1: *Tracks can either be found by (a) extrapolating tracks from two close hits and (b) interpolating between two hits separated by a larger distance. The letters denote the individual measurement layers. (From [65]).*

in the T stations. It delivers track candidates that are used as seeds by other pattern recognition or by track fitting algorithms. The algorithm is no longer being used.

The chapter is ordered as follows. First an overview is given of the track types that are used in LHCb. Then a description is given of the *T Seeding* algorithm. In the last sections the performance of the implemented algorithm is presented.

4.2 Track types in LHCb

The tracking system in LHCb can be divided in an upstream and downstream region (See Fig. 2.4). The trackfinding makes use of the following detectors: the VELO and the TT stations (upstream) and the TT and T stations (downstream). Different tracktypes are defined depending on their location in the spectrometer; these are depicted in Fig. 4.2.

T tracks are reconstructed from hits in the T stations. These tracks are used by other algorithms to form longer track types: the long tracks and downstream tracks. Those that are not used as such are used for pattern recognition of RICH2.

Downstream tracks are found in the downstream region. They contain hits in the TT stations and T stations. Particles that exclusively leave hits in these detectors are often associated to charged particles from decays of longer living neutral particles, such

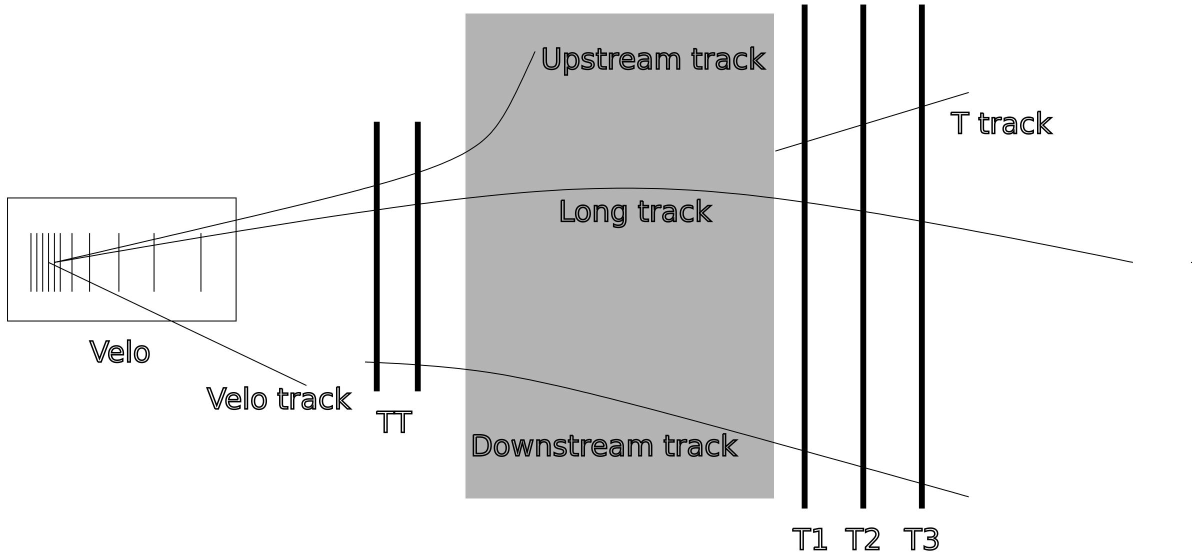

Figure 4.2: *The track types that are distinguished in LHCb track finding together with the subdetectors that are used. The shaded area indicates the location of the main magnetic field.*

as K_s-mesons and Λ-baryons.

VELO tracks are formed from hits in the VELO. A fraction of these are used in the contruction of upstream tracks and long tracks. These are related to particles that are produced in the forward acceptance. Those tracks that have a large polar angle or travel in the backward direction remain VELO tracks. They are mainly used in the determination of primary vertices.

Upstream tracks are found with hits from the VELO and the TT stations. Low momentum particles that are ejected from the acceptance by the magnet are associated to these kinds of tracks, *e.g.* soft pions from the decay $D^{*\pm} \to D^0\pi^{\pm}$.

Long tracks are found from hits in all tracking detectors produced by particles traversing the whole spectrometer. These tracks will have a precisely reconstructed momentum and impact parameter and are usually associated to minimum ionising particles as charged pions, muons and kaons. Also electrons are found this way, although the efficiency is somewhat lower due to bremsstrahlung.

To evaluate the performance of the reconstruction "true" Monte Carlo particles are used. Their trajectories are defined by linking all the hits they caused: the so-called *ideal reconstruction*. As such the MC particles are also divided in T Station, Downstream, VELO, Upstream, and Long categories.

4.3 Seeding Algorithm for the T stations

4.3.1 Overview

The Seeding algorithm for the T stations is part of the LHCb pattern recognition. The algorithm described here is based on a previous idea described in [69]. The algorithm creates T tracks using interpolation of hits. The output of the algorithm are tracks consisting of one trackstate at a z-position in the centre of the T stations ($z = 8700$) and the list of measurements, which are derived from the hits in the detector.

The trackstate contains 5 parameters; the x and y position of the track, a slope in the xz plane, s, a slope in the yz plane, t, and a momentum estimate q/p from the curvature of the track.

A small, but non-negligible, magnetic field is present in the region of the T stations. This field causes the charged particle trajectories to deviate from a straight line. In the track finding process this field is taken into account.

The tracks are initiated by taking hits in the x-layers of the outermost stations T1 and T3. Using interpolation hits are added in a search window around a parabola in the xz plane. The curvature term of a parabolic fit is used as an initial momentum estimate.

The hits in the yz layers[1] are added using a linear interpolation. The magnetic field component perpendicular to this plane is sufficiently low that the tracks can be assumed to be straight lines in this projection. After a 3-dimensional track candidate is reconstructed a likelihood based track rejection method is applied, and the remaining tracks are stored. In the next three sections the individual steps of the algorithm will be set forth.

The T stations are divided into an upper part and a lower part. Due to the magnetic field a particle will not be deflected in the vertical plane parallel to the beam. Therefore the lower and upper halves of the detector are disconnected in the track finding process. Furthermore, the seeds are divided into three different categories; tracks that traverse only the OT (*OT tracks*), tracks that traverse only the IT (*IT tracks*) and tracks that traverse both detectors (*cross tracks*).

Due to the fact that the IT uses silicon planar detection layers and the OT uses drift tubes, there is a difference in the way hits are treated. The outer tracker cells have an isochrone or drift ring due to the cell symmetry. Whether the particle traversed on the lefthand side or the righthand side of the wire cannot be determined from the hit information itself. This aspect is called the left-right ambiguity. These ambiguities are resolved by fitting the track and the determination of the best track is calculated with the likelihood method which is described in section 4.3.4. This process is illustrated in Fig. 4.3.

[1] The y-co-ordinate is calculated from the u,v and x co-ordinates, this will be explained in Sec. 4.3.3.

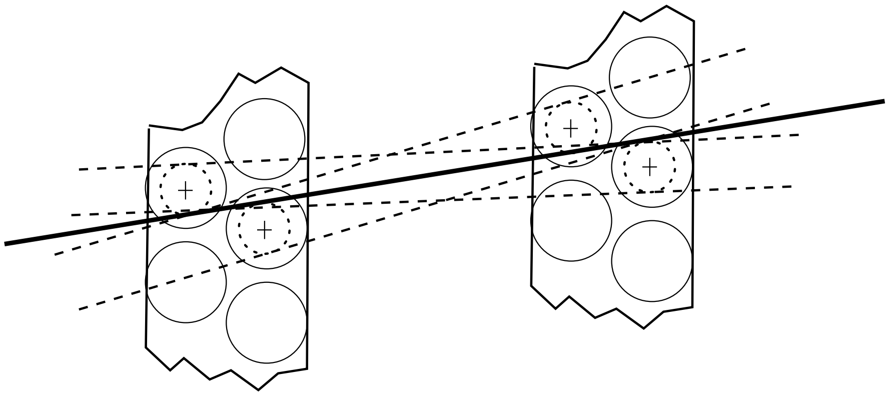

Figure 4.3: *The ambguities of the isochrones are resolved by choosing the best fit when they are more than two hits assigned to the track.*

track category	OT track	IT track	cross track
$s_{\max}$	1.5	0.4	1.0
x_{max} (cm)	250	80	80
$\Delta x_{1,3}$ (cm)	1.0	0.1	0.7
Δx_2 (cm)	1.5	0.5	1.3
$nx_{\min}$	7	4	5
$nx2_{\min}$	8	4	6
δx (cm)	0.1	0.04	0.1

Table 4.1: *Parameters used to restrict the pattern tracks in the xz plane depending on the track category. The parameters are introduced in the text. The values of the parameters are optimised to obtain high efficiency while reducing the number of false combinations.*

4.3.2 X projection and 2D search

Prototrack search

Initial track candidates are created from x hits in the outer most stations T1 and T3. At first ignoring the drift-time information the centres of the hits are connected by a straight line and a prototrack is formed.

Tracks with a very large slope, defined as $s = \frac{x_{T3}-x_{T1}}{z_{T3}-z_{T1}}$, are generally associated with a low momentum. Such low momentum particles typically can not originate from the primary vertex due to the bending power of the magnet. Hence the choice for the restriction on the slope is a compromise between reducing many false hit combinations and finding less tracks with a genuinely low momentum that reach the T stations. The restrictions on the slopes are listed in Table 4.1.

Due to the finite size of the tracker stations, the slopes of tracks at the edge of the first T station are on average different than the slopes at the centre of the station. Depending on the position in station T1, x_{T1}, the slope s is compared to a maximum

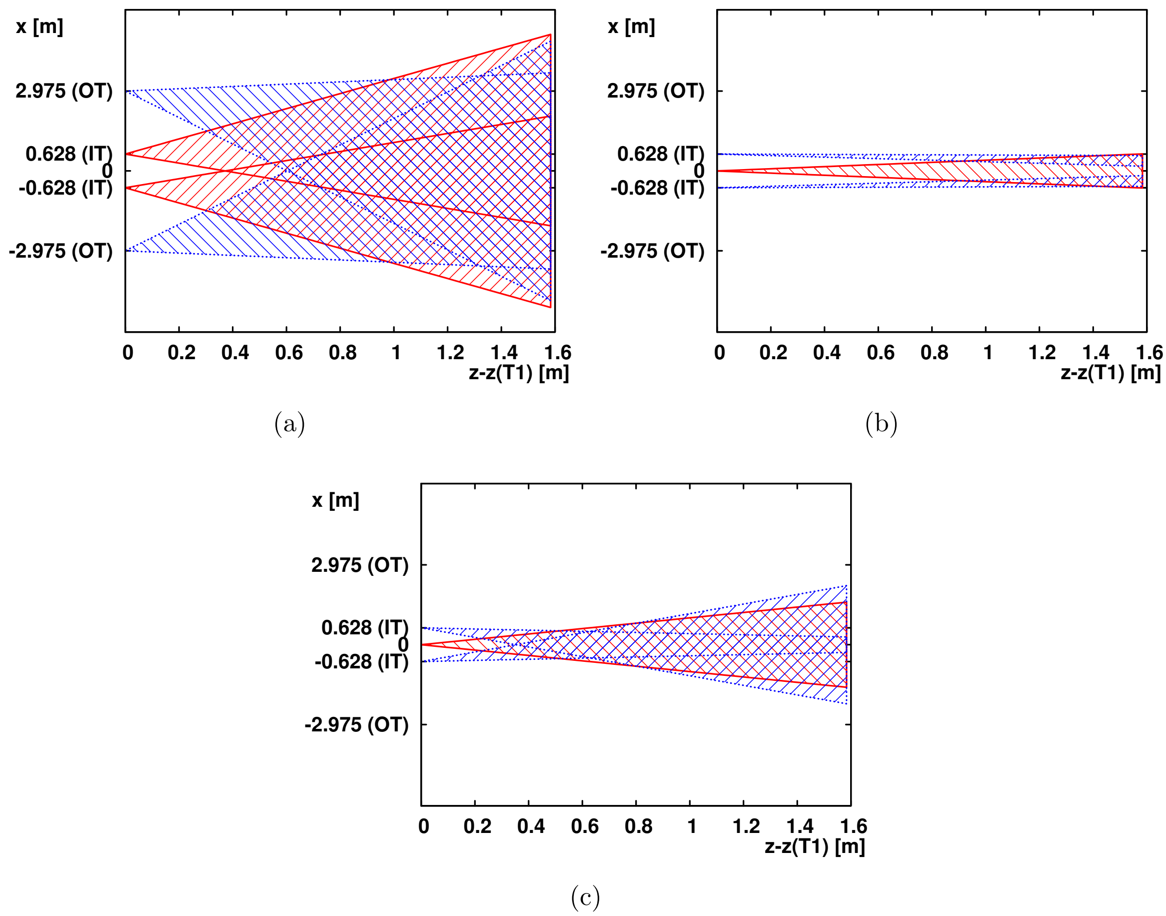

Figure 4.4: *(a) Allowed horizontal slopes for OT tracks departing from the boundaries of the outer tracker, (b) allowed slopes of IT tracks departing from the centre and the boundaries of the inner tracker and (c) allowed slopes of cross tracks departing from the boundaries of the innertracker.*

slope s_{max} and a maximum position, x_{max} with the following requirement:

$$\left| \frac{s}{s_{\max}} - \frac{x_{\mathrm{T1}}}{x_{\max}} \right| < 1.$$

The values of $s_{\max}$ and $x_{\max}$ depend the track category due to the different positions and sizes of the OT and IT detectors. This is illustrated in Fig. 4.4.

Once a prototrack is made, hits from the three stations are selected in windows around this prototrack. The window size for the three stations $\Delta x_{1,2,3}$ depends on the track category and is listed in Table 4.1. The window is larger in the middle station to accomodate for the curvature of the tracks. Relativistic particles of charge e and momentum p (eV) traversing a homogeneous magnetic field with strength B (T) at a speed near the speed of light $v \approx c$, will describe a circular trajectory with a radius R

(m) equal to

$$R = \frac{p}{Bc}. \tag{4.1}$$

The sagitta, s (m), of a circular track traversing a length L (m) is then given by

$$d = \frac{0.3BL^2}{8p} \tag{4.2}$$

The integrated magnetic field[2] between T1 and T3 is $\int B\mathrm{d}l \approx 0.245$ Tm, and the distance between the first and last station is 1.4 m. A particle with a minimum momentum of 1 GeV/c can have a trajectory between T1 and T3 with a maximal sagitta of 1.3 cm. The windows accomodate these tracks.

If the centre of the hit cell is within the window, the cell is kept as possibly belonging to the track candidate. This step is schematically represented in Fig. 4.5.

At this point a miminum number of hits is required to be in the windows: nx_{min}; for the OT tracks at least 7 hits must be present, for the IT tracks 4 hits, and for cross tracks 5 hits. Furthermore, each station should have at least a single hit in the x layer.

Precision track search using drift time

The knowledge of the hit positions is not limited to the centres of the hit cells. More accurate positions are determined using the drift time measurement in the OT. However the OT cells have a left-right ambiguity which is not known from the information of a single hit.

To include and ultimately solve these ambiguities of the OT cells, a set of parabolas is constructed using the drift time information. Each parabola is constructed from three initial hits from the windows, one hit from each station. This is drawn in Fig. 4.6. A priori it is not known what the correct combination of ambiguities will be. Therefore all hit combinations and the ambiguities should be tried. However, since this yields very high combinatorics for all the hits in the windows[3] this is not optimal. To avoid multiple copies of the same track already assigned hits will not be re-used in the construction of a new parabola. Which hits are excluded will be explained next.

Around each constructed parabola of three hits smaller windows of size δx are made (see Table 4.1). This is indicated in Fig. 4.6 by the grey shading. The additional hit positions using both ambiguities are compared to these smaller windows around the parabola. Compatible hits are added to the track candidate. Hits for which both ambiguities fit, will be added twice and the ambigity will be resolved at a later stage. To reduce combinatorics, individual hits that are added to a track candidate will not be used (with this specific ambiguity) as initial hits for another parabola. The idea is that the hits that are close enough are part of the same candidate. The total number of hits that are included in all the windows has to be to minimally $nx2_{\text{min}}$.

[2]Determined from the software parametrisation v2.5 of the magnetic field.

[3]As an example with 7 hits distributed as 2 in the first two stations and 3 in the last, this yields with the ambiguities at least $((2 \times 2) \times (2 \times 2) \times (2 \times 3)) = 96$ combinations of parabolas to be tried.

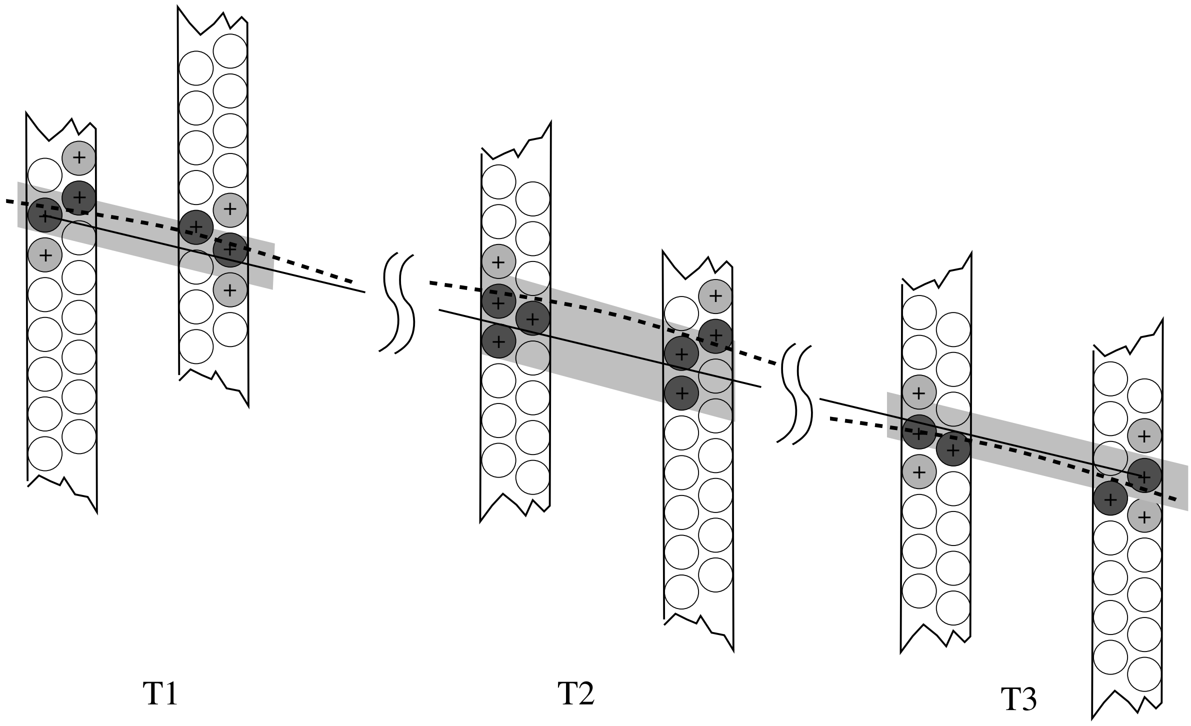

Figure 4.5: *The particle traverses the stations according to the dashed trajectory, leaving hits in cells (crosses). The initial search windows are made along a straight line (solid line). The search window is larger in the middle station to accomodate hits on a parabolic trajectory. Darker shaded hits are included within the boundaries of the windows.*

The hits that are in the small windows of the parabola are subject to a fast parametric least-χ^2 fit. Hits that deviate more then 3σ from the nominal fit are rejected and the track is subsequently refitted. This process of fitting and rejecting is iterated until no more outliers exist. The fitted curvature term of the parabola provides a measurement of the particle momentum.

This curvature of the track in the T stations due to the integrated magnetic field of $\int_{T1}^{T3} B_y \mathrm{d}z \approx 0.245$ Tm is related to the momentum via (4.1). The local radius of the circular path is related to the curvature term a of the parabolic parametrisation $ax^2 + bx + c$ according to[4] $R = \frac{1}{2a}$. Furthermore the magnetic field in the T station region of 1.4 m is $\frac{\int B \mathrm{d}l}{\Delta z} \approx \frac{\int_T B_y \mathrm{d}z}{\Delta z} \approx 0.175$ T. For particles with unit charge this means that the relation between momentum and curvature is

$$\frac{1}{p} = \frac{a}{0.026}, \tag{4.3}$$

for momenta measured in GeV/c and curvatures in m^{-1}.

[4]Stricty this holds only when the centre of the parabola, $R(x) = R(0)$. Due to the varying B-field along the particle path a parabola gives a better description of the trajectory.

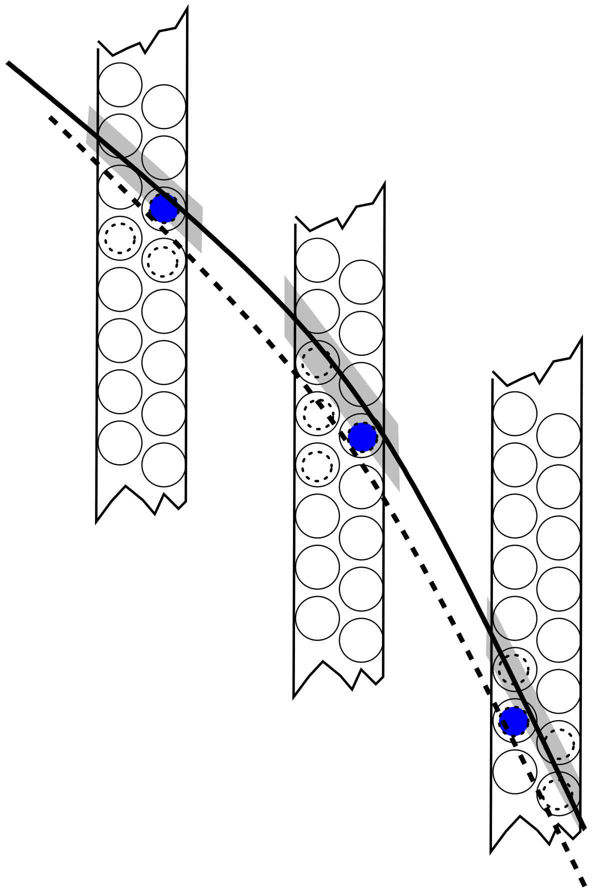

(a)

Figure 4.6: *Three hits are used, one in each station, to construct a parabola (solid line) including a drifttime and a left-right ambiguity. The actual track is indicated with a dashed line. Note the image is not to scale only to demonstrate the method more clearly.*

The curvature of the fitted track in the T stations is compared to the deflection due to the magnetic field assuming the track originates from the nominal interaction point at $(x, y, z) = (0, 0, 0)$. The effect of the magnetic field on a charged particle is approximated as an instantaneous change of direction (*kick*) at the centre of the magnet at $z = 5300$. This method of determining the momentum is named the p_t-kick method [70].

In Fig 4.7 a schematical drawing of the p_t-kick method is given. The magnetic field $\mathbf{B}$ changes the x component of the momentum of a charged particle in direction by

$$\Delta p_x = q \int |\mathbf{B} \times \mathrm{d}\mathbf{l}|_x, \tag{4.4}$$

where q equals the charge of the particle and $\mathbf{l}$ is the direction. In terms of track

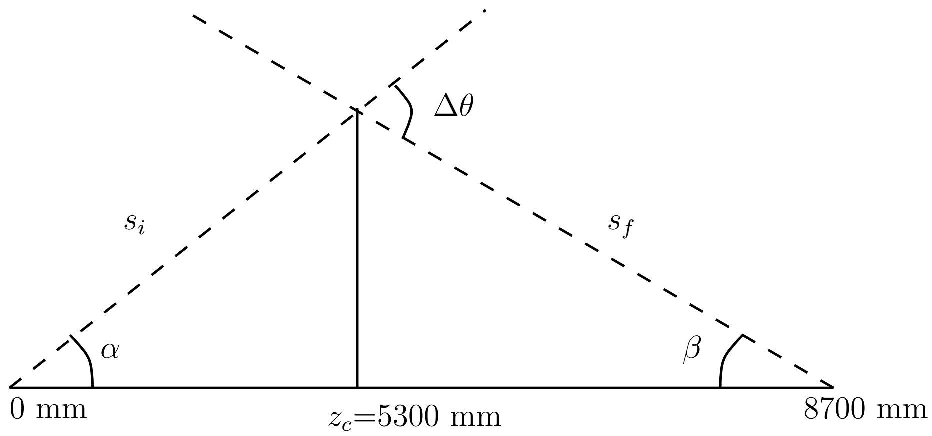

Figure 4.7: *The p_t-kick method assumes a track originating from the nominal interaction point at $(x, y, z) = (0, 0, 0)$. The reconstructed track candidate has a slope s_f defined in the centre of the T stations at $z = 8700$ mm. This track is extrapolated to a plane in the centre of the magnet at $z_c = 5800$ mm. The slope of the initial track, s_i, can now be computed and compared to the slope of the final track, s_f, after bending in the magnet. The kick $\Delta\theta$ can be computed.*

parameters of the candidates the momentum change can be expressed as

$$\begin{aligned} \Delta p_x &= (p_f - p_i)_x \\ &= p\left(\frac{s_f}{\sqrt{1+s_f^2+t_f^2}} - \frac{s_i}{\sqrt{1+s_i^2+t_i^2}}\right). \end{aligned} \tag{4.5}$$

Where $s = dx/dz = p_x/p_z$ is the slope of a track in the xz plane, $t = dy/dz = p_y/p_z$ is the slope in the yz plane and the labels i and f are used to denote tracks before and after the magnet respectively. The Lorentz force on the particle $\mathbf{F}_l = q\mathbf{v} \times \mathbf{B}$ is equal to the change in momentum per unit time, yielding $\Delta p = q \int B dl$. Hence we can equate this to (4.5) and obtain

$$p = \frac{q \int B\mathrm{d}l}{\left(\frac{s_f}{\sqrt{1+s_f^2+t_f^2}} - \frac{s_i}{\sqrt{1+s_i^2+t_i^2}}\right)}. \tag{4.6}$$

Assuming that for tracks in the LHCb forward acceptance the slope in the non-bending plane is small $t_i = t_f \ll 1$, (4.6) maybe written

$$p \approx \frac{q \int B\mathrm{d}l}{\left(\frac{s_f}{\sqrt{1+s_f^2}} - \frac{s_i}{\sqrt{1+s_i^2}}\right)}, \tag{4.7}$$

and from Fig. 4.7 it can be seen that $s_i = \tan\alpha$ and $s_f = \tan\beta$. This yields a simple

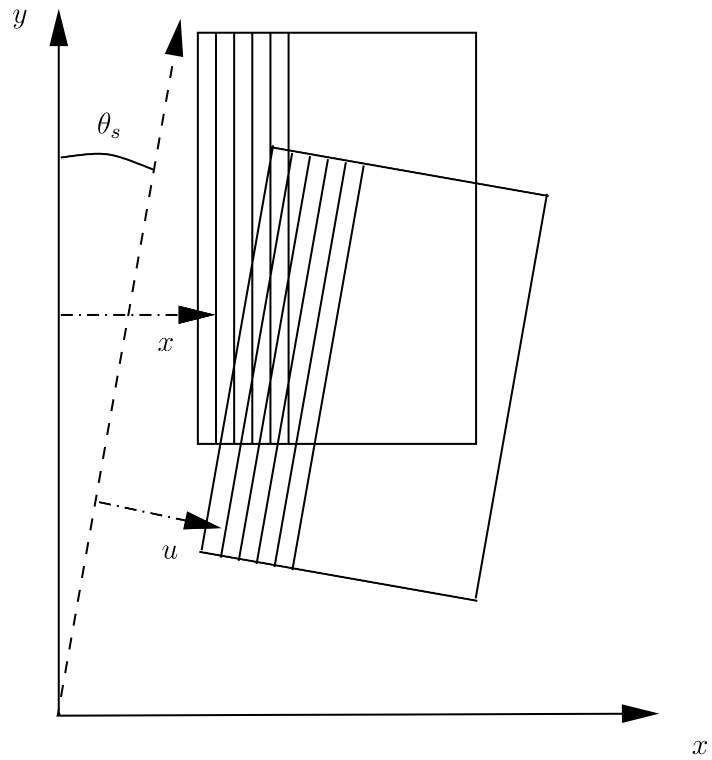

Figure 4.8: *The relative orientation of the x and stereo coordinate u are shown. The stereo channels are rotated with an angle of $\theta_s = 5^\circ$ with respect to the x layers. A channel can be an OT drift tube or an IT strip.*

relation for the momentum as

$$p = \frac{q \int B \mathrm{d}l}{\sin \beta - \sin \alpha}. \tag{4.8}$$

When the momentum from the curvature calculation is compared to the momentum of the p_t-kick angle calculation a relation between the p_t-kick angle and the curvature term is obtained. A matching condition is applied to the curvature and the deflection angle. Using (4.3) for the momentum calculated from the curvature p_c and (4.8) for the momentum p_k calculated from the p_t-kick angle tracks are only passed when they satisfy the following criterium[5]:

$$\begin{aligned} \frac{3250}{p_c} - \frac{2.1}{p_k} &< 1, \mathrm{AND} \\ \frac{3250}{p_c} - \frac{18.4}{p_k} &> 1. \end{aligned} \tag{4.9}$$

4.3.3 Y projection and 3D track candidates

To add the third dimension to the track candidates, the stereo layers of the tracker are used. The stereo layers provide u and v measurements which are projected to a y coordinate using information from the xz track candidate. The u coordinate is related to x and y via

$$u = x \cos\theta_s + y \sin\theta_s. \tag{4.10}$$

The relative orientation of the u and x channels can be seen in Fig. 4.8. The angle $\theta_s = 5°$ is the angle of the stereo channels with respect to the x channels. The ordinate x in (4.10) is the x position of the xz track extrapolated to the z position of the stereo plane. By inverting the equation the y coordinate is obtained.

Several stereo hits corresponding to different y coordinates can be consistent with the predicted x-position on the xz candidate. Hit projections with $|y| > y_{max} = 2.405$ m are outside the tracker and are not considered.

The collection of y hits matching the xz candidate track is subject to a yz track search in a similar way as the original xz track search. Two hits in station 1 and 3 from the collection of y hits are connected to form a yz prototrack. The magnetic field component perpendicular to the yz plane is negligibly small and therefore there is no bending in this plane such that almost no tracks are expected to cross from top to bottom or vice versa. The prototracks in the yz plane are restricted in the slope to, $t_{\min}$ and $t_{\max}$. The values depend on the track category and if they originate in the bottom or top part of the detector. The values are listed in Table 4.2.

Similar to the xz track search, the drift time information of OT is not used in this first step. A path is opened around the yz prototrack and y hits from all stations within the path are added to the track candidate. Hits are flagged as used and previously flagged hits will not be used in a subsequent search. The path sizes used in the three stations are $\Delta y_{1,2,3}$. The path size for the tracks with an OT measurement are large due to the left-right ambiguity which is not yet known at this point. At least $ny_{\min}$ hits are required in this path to continue the track finding. The values of the parameters are summarised in Table 4.2

In the collection of hits in the path two hits are taken from the first and last station and a new yz track candidate is created. Taking into account the drift distance and trying both possible left and right ambiguities, hits from all stations are then compared to a narrower path around a straight line with a width of δy around the yz track candidate. The new path should include minimally $ny2_{\min}$ hits.

Finally, a least χ^2 straight line fit is performed on the hits in the new path. The fit produces the yz projection of the candidate. At the same time an iterative outlier hit rejection is applied. Hits that are more than 3 standard deviations from the fit are rejected. This process of fitting and rejecting is iterated until no more outliers exist. Also double ambiguity hits are resolved by taking the ambiguity with the best fit on the track candidate.

In the case where multiple yz candidate tracks have been reconstructed with the

[5]These numbers were calculated in [69] were they were guessed on the basis of Monte Carlo studies.

track category	OT track	IT track	cross track
$y_{\max}$ (m)	2.405	2.405	2.405
$t_{\min}$ $(y > 0)$	-0.15	-0.025	-0.03
$t_{\min}$ $(y < 0)$	0.15	0.025	0.03
$t_{\max}$ $(y > 0)$	0.3	0.05	0.03
$t_{\max}$ $(y < 0)$	-0.3	-0.05	-0.03
$\Delta y_{1,2,3}$ (cm)	6.0	0.4	6.0
$ny_{\min}$	7	4	6
$ny2_{\min}$	7	4	5
δy (cm)	1.5	0.4	1.5

Table 4.2: *Parameters used to restrict the pattern tracks in the yz plane depending on the track category. The parameters, which are introduced in the text, are optimised by trial to obtain high efficiency while reducing the number of wrong combinations.*

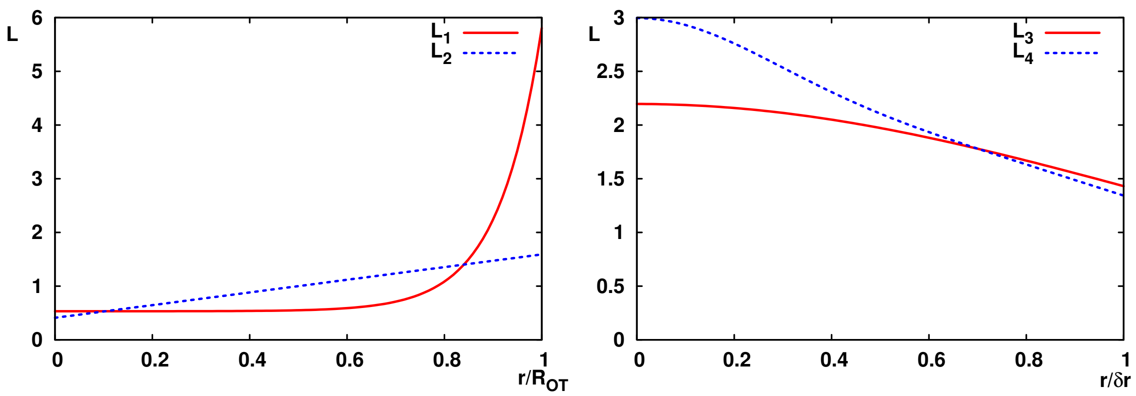

Figure 4.9: *The shapes of the likelihood distributions $\mathcal{L}_1 - \mathcal{L}_4$.*

same xz track, the best yz candidate is chosen on the basis of the likelihood calculation, which is explained next.

4.3.4 Track likelihood

From the parameters of a track candidate the expected hit positions in the individual measurement planes can be predicted. These predictions are compared to the actual observed hits in a likelihood method. The likelihood for an OT drift tube to contain a hit due to a track depends on the radius of the OT drift tube, R_{ot}, and the distance of closest approach of track with the tube, r. The likelihood for an IT strip to contain a hit due to a track is assumed not to depend on the distance to the centre of gravity of the charge distribution.

For the OT detection layers a likelihood is assigned according to the following cases;

for each measurement plane:

1. There is no hit assigned to the candidate track and no hit seen on the traversed wire:

$$\mathcal{L}_1(r) = \mathrm{a}_0 + \mathrm{a}_1\ e^{-\mathrm{a}_2\ (1-r/R_{ot})} \tag{4.11}$$

   This likelihood models a detection *inefficiency*. The distance r is calculated as the distance between the predicted position and the position of the closest wire. The constant term represents a detector inefficiency, the second term is a resolution effect. The values of the constants are given in Table 4.3, and the likelihood function is plotted in Fig. 4.9(a).

2. There is no hit on the candidate track, but a hit on the passed wire:

$$\mathcal{L}_2(r) = \mathrm{b}_0 + \mathrm{b}_1\ r/R_{ot} \tag{4.12}$$

   This likelihood models an algorithm ineffiency since the track candidate did not have a hit, but a wire in the layer was hit within a distance of 1/2 a OT cell diameter. This may happen when, for example, a hit was ejected from the candidate during the refitting and outlier procedure. The distance r is calculated here as the distance between the predicted position and the actual hit wire position. A linear likelihood is assigned to such cases. The likelihood function is plotted in Fig. 4.9(a).

3. There is a single hit on candidate track:

$$\mathcal{L}_3(\hat{r}) = \mathrm{c}_0 + \mathrm{c}_1\ e^{-\hat{r}^2/2\mathrm{c}_2^2} \tag{4.13}$$

   When a track candidate does have an OT hit assigned to it, the hit position is determined more accurately by the drift time. The drift time will have an uncertainty which is converted to an uncertainty on the measured hit position, δr. A normalised hit distance is calculated according to the distance of the predicted track to the actual hit position as $\hat{r} = r/(\delta r)$. The likelihood function is plotted in Fig. 4.9(b)

4. There are a multiple of hits on the candidate track:

$$\mathcal{L}_4(\hat{r}) = \mathrm{d}_0\ e^{-\hat{r}^2/2\mathrm{d}_1^2} + \mathrm{d}_2\ e^{-\hat{r}^2/2\mathrm{d}_3^2}. \tag{4.14}$$

   The likelihood is assumed to be distributed according to Gaussian distributions. There can be at most two hits per measurement layer when two neighbouring cells are included in the candidate. The distance to the nearest hit is taken to calculate $\hat{r}$. However, two Gaussians are used with two standard deviations, d_1 and d_3.

All parameters for the likelihoods are obtained from the previous version of the Seeding code [69] and listed in Table 4.3 and the likelihood distributions themselves are plotted in Fig. 4.9.

i	a_i	b_i	c_i	d_i
0	0.532	0.410	0.034	0.702
1	5.275	1.181	2.162	0.2532
2	11.277	-	1.070	2.294
3	-	-	-	0.966

Table 4.3: *Values for the parameters* a_i*,* b_i*,* c_i *and* d_i *with index* $i = 0, 1, 2, 3$ *for the likelihoods* $\mathcal{L}$*.*

The final likelihood for a track is produced by multiplying the likelihoods of all detection layers and multiplying the result with a binomial likelihood with the detection channel efficiency for the number of hits on the candidate

$$\mathcal{L} = \prod_{\text{Layers}} \mathcal{L}_i \times \mathcal{L}(p|n, k). \tag{4.15}$$

Here $\mathcal{L}_i$ are the likelihoods of the separate detection layers. The number of actual hits on the candidate is denoted k and the number of detection layers is denoted n. In the calculation of the binomial likelihood $\mathcal{L}(p|n, k)$ the probability p is equal to the efficiency of a detection cell, which was conservatively chosen as $\epsilon_{OT} = 0.92$ and $\epsilon_{IT} = 0.97$.

4.3.5 Track selection

A track candidate is selected by setting a threshold on the logarithm of the likelihood that was presented above. This threshold can be varied to produce more track candidates with less hits and hits that are farther away from the central fit, or fewer track candidates that have more hits and hits that are closer to the central fit. Candidates with more hits that are closer to the central fit give a higher likelihood are considered to be of higher quality.

Track candidates that share more than three hits are considered to be clones. Of the clone tracks, the one with the highest total hits is kept while the others are discarded. When the clones have the same number of hits, the track with the highest likelihood is kept.

4.4 Performance

4.4.1 Definitions

A reconstructed track is associated to a list of possible MC particles via the origin of the hits that are assigned to the track (see Sec. 3.1.4). The maximum number of hits on a track that originate from a single MC particle ($N_{\text{hits}}^{\text{same}}$) divided by the total number of hits ($N_{\text{hits}}^{\text{total}}$) on the track is called the *hit purity* of a track. A track is considered to be correctly reconstructed (or associated to a Monte Carlo particle) if it has a purity of higher than 70%.

The *efficieny*, ϵ, of a track finding algorithm is defined as the fraction of correctly reconstructed Monte Carlo particles ($N_{\mathrm{MC}}^{\mathrm{cor}}$) that have been found among the total number of MC particles in a given sample ($N_{\mathrm{MC}}^{\mathrm{tot}}$),

$$\epsilon = \frac{N_{\mathrm{MC}}^{\mathrm{cor}}}{N_{\mathrm{MC}}^{\mathrm{total}}}. \tag{4.16}$$

The track finding will also yield fake tracks, so-called *ghost* tracks, which have a purity less than 70%. These can be ascribed to wrong combinations of hits left by particles as well as to noise hits or cross talk. The *ghost rate*, γ, is the total number of reconstructed tracks ($N_{\mathrm{rec}}^{\mathrm{total}}$) minus the number of correctly reconstructed tracks ($N_{\mathrm{rec}}^{\mathrm{cor}}$) divided by the total number of reconstructed tracks:

$$\gamma = \frac{N_{\mathrm{rec}}^{\mathrm{total}} - N_{\mathrm{rec}}^{\mathrm{cor}}}{N_{\mathrm{rec}}^{\mathrm{total}}}. \tag{4.17}$$

There are two ways to specify efficiency and ghost rates, referred to as *track weighted* and *event weighted*. The track weighted numbers are obtained by calculating the efficiency ϵ and ghostrate γ using (4.16) and (4.17) over a sample of events. The event weighted numbers of efficiency and ghost rate are obtained by first calculating ϵ and γ for each event and subsequently calculating the average ϵ and γ over the event sample. In this thesis the track averaged numbers are quoted, which are more conservative due to the higher weight of very busy events.

The precision of a reconstructed track parameter, x is described by the parameter residual:

$$R(x) = x_{\mathrm{rec}} - x_{\mathrm{true}}. \tag{4.18}$$

The labels “rec” and “true” signify the reconstructed value and the corresponding MC truth value respectively.

The mean and width of the residual distribution of the parameters correspond to the bias and the resolution of the reconstruction method. The estimate of the parameter covariance matrix C_{ij} is used to define a normalised resolution or *pull*, which is defined as

$$P(x) = \frac{x_{\mathrm{rec}} - x_{\mathrm{true}}}{\sqrt{C_{ii}}} = \frac{x_{\mathrm{rec}} - x_{\mathrm{true}}}{\sigma_x}. \tag{4.19}$$

In the case that the reconstruction is correct the distribution of $P(x)$ should follow a Gaussian distribution with unit standard deviation.

4.4.2 Hit purity and hit multiplicity

The hit purity distribution of the tracks found by the seeding pattern recognition is displayed in Fig. 4.10(a) and is on average 98%. The hit multiplicity for correct tracks and ghost tracks found by the pattern recognition is shown in Fig. 4.10(b). When the hit multiplicities are split in tracks that have mainly (>80%) OT hits and tracks that have mainly (>80%) IT hits, shown in Figs. 4.10(c) and (d) respectively, it can be seen that the majority of the ghost tracks have mainly hits in the OT. A restriction on the

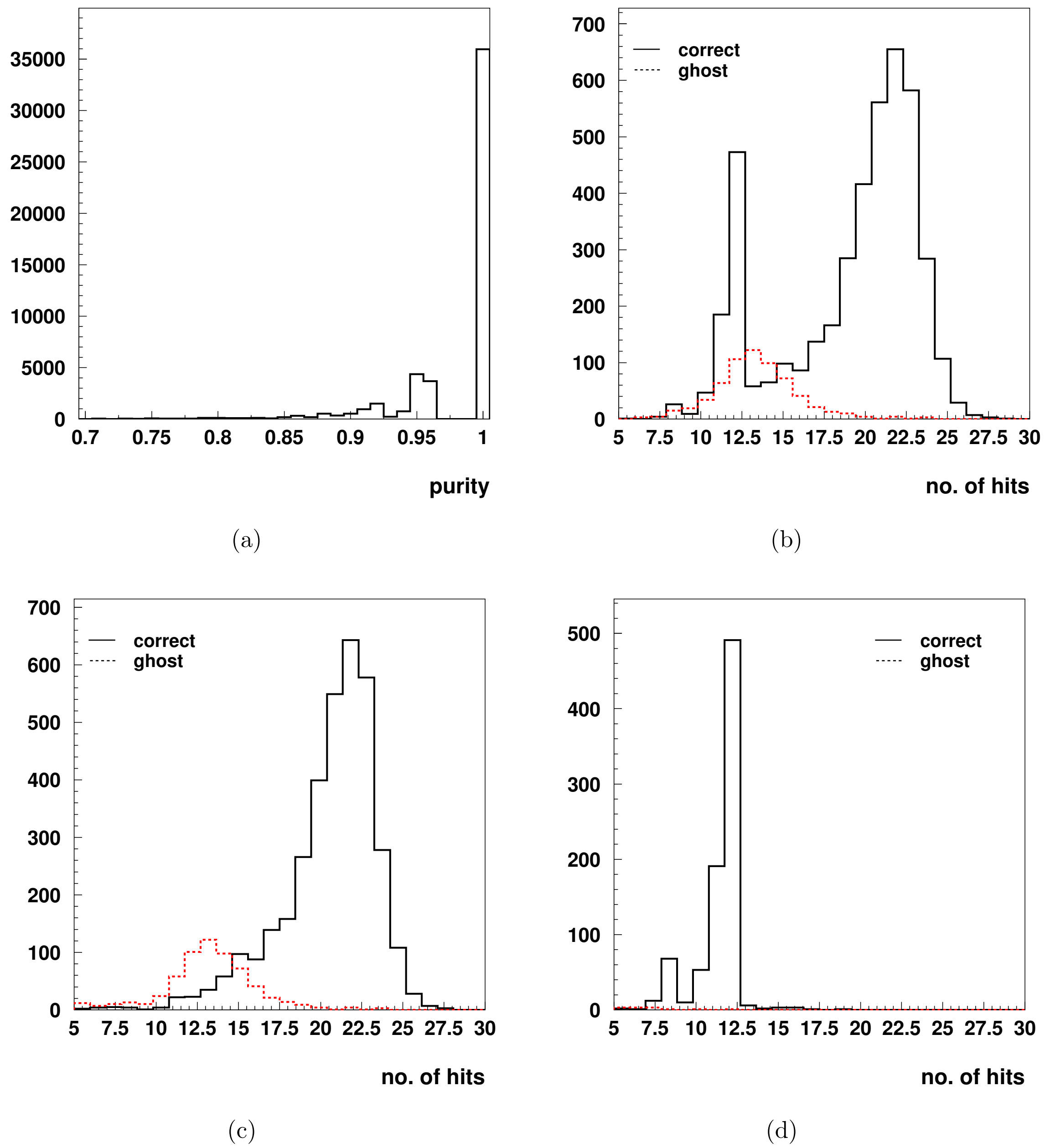

Figure 4.10: *(a) Track purity of true tracks, (b) hit multiplicity for a long MC particle sample, (c) hit multiplicity of tracks that have their hits predominantly (>80%) from the OT and (d) hit multiplicity of tracks that have their hits predominantly (>80%) from the IT.*

hit multiplicity can be used to obtain a clean sample with less ghosts at the cost of a reduced efficiency. Tracks which have at least 80% of their hits from the IT, have a very low amount of ghost tracks.

4.4.3 Efficiency and ghost rate

The performance in terms of efficiency and ghost rate of the track finding is tested with two MC particle samples: Long MC particles and T Station MC particles. The efficiency and the ghost rate of the track finding algorithm depend on the MC truth momentum of the particles. In Fig. 4.11(a) the efficiency is plotted for a sample of long MC particles and T Station MC particles that are reconstructed with the T Seeding pattern recognition. Fig. 4.11(b) shows the ghost rate of tracks reconstricted with the seeding T Station pattern recogntion as a function of a reconstructed momentum cut. The ghostrate is calculated for all the tracks with a reconstructed momentum greater than p_{cut}.

The efficiency of finding T Station MC particles at low momentum visible in Fig. 4.11(a) is due to particles which traverse the T stations at a steep angle which are not reconstructed in the seeding algorithm. The efficiency of finding tracks diminishes slightly at higher momentum, this is due to a higher detector occupancy in the forward region.

The ghost rate at first diminishes and then rises slightly with momentum. The higher ghost rate at low momentum is related to the lower efficiency for finding correct T tracks. Similarly to the efficiency reduction, the slight rise in the ghost rate at high momentum is due to a higher occupancy in the forward region.

The average efficiency and ghost rate also depend on the track quality requirement imposed by the likelihood restriction on the tracks. By changing the maximum likelihood of a track the average ghost rate and average efficiency can be tuned as shown in Fig. 4.12.

4.4.4 Track parameter distributions

In Fig 4.13 the pull distributions are displayed of the parameters x, y, s and t at a state located in the centre of the T stations at $z = 8700$ mm. These distributions show no bias, while their width is approximately 30% larger than the expected value 1. There are believed to be two main causes for this effect: the first is wrongly assigned hits or L/R ambiguities; the second is multiple scattering. There is a dependence on the momentum ranging from 20% larger at high momenta to 40% larger at low momenta. The dependence on the curvature ($1/p$-parameter) is displayed in Fig. 4.14. The rise versus $1/p$ indicates that multiple scattering plays a role. This can be understood since the parabolic track model does not include multiple scattering and therefore underestimates the errors for low momentum. This effect can be taken into account, however it would require tuning to Monte Carlo samples. The algorithm is developed to construct tracks from hits (by pattern recognition). The optimisation of the track parameters is better suited for a track fitting routine that takes effects such as multiple scattering into account.

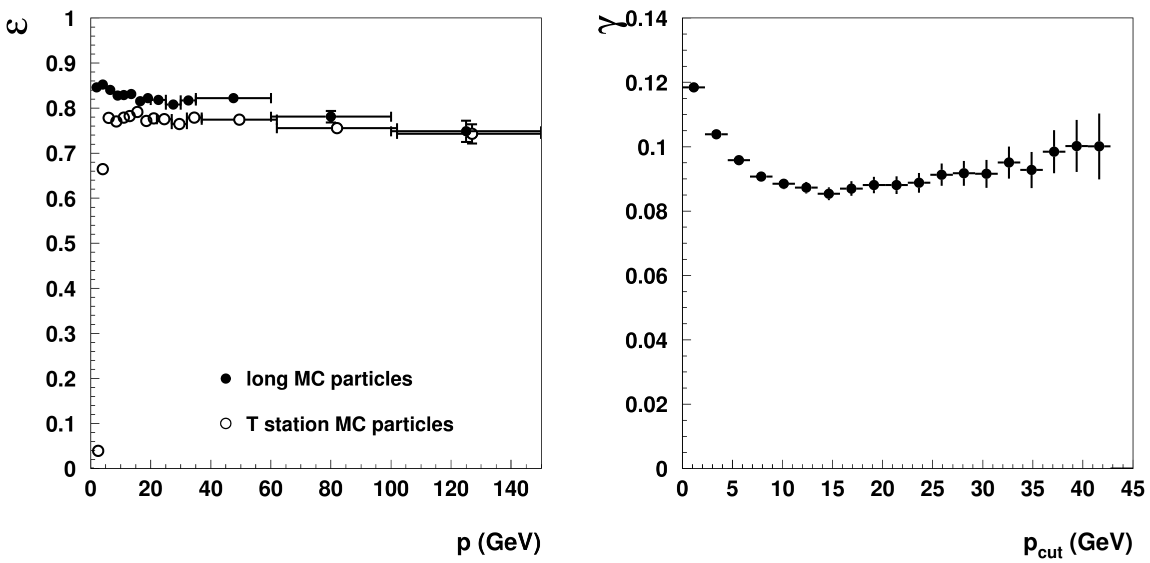

(a) (b)

Figure 4.11: *(a) Efficiency depending on the MC truth momentum for long and T station MC particles. (b) Ghost rate of the seeding algorithm dependent on reconstructed momentum greater than* p_{cut}.

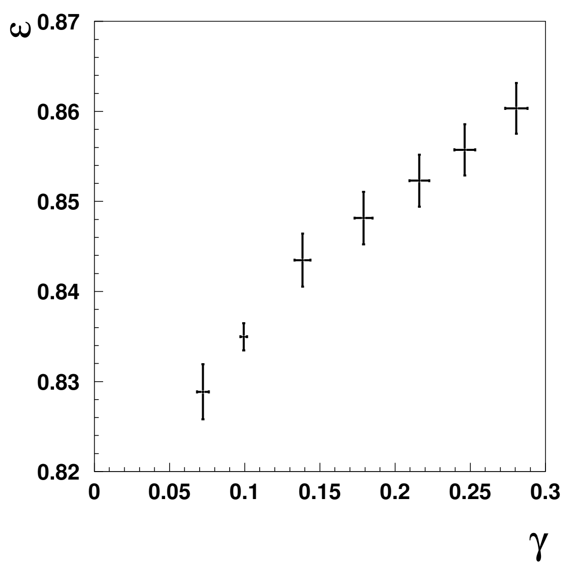

Figure 4.12: *Average efficiency versus average ghost rate dependency on the likelihood restriction for long MC particles.*

The resolutions of the first four parameters (x, y, s and t) in the trackstate for long MC particles are shown in Fig. 4.15 for tracks with >80% of the hits in OT and in Fig. 4.16 for tracks with >80% of the hits in the IT. The hit resolutions in the IT are seen to be about a factor of 5 smaller than the hit resolution of the OT, which is consistent with their typical resolution of an OT hit of 200μm and the resolution of an IT hit of 40μm.

Due to the stereo geometry the resolution on the y coordinate in Figs. 4.15(b) and 4.16(b) is worse than the x coordinate resolution plotted in Figs. 4.15(a) and 4.16(a). The method in which the y coordinate is calculated is given in (4.10). Since the detector effectively measures the x coordinate with 4 measurement planes and the y coordinate with 2 stereo planes the resolution of the y coordinate is expected to be a factor of $\sqrt{2}/\sin(5°) \approx 16$ larger. Indeed the observed resolution of the y coordinate is larger by a factor 14 (OT)-15 (IT). For the track slope distributions in Figs. 4.15(c) and (d) and Figs. 4.16(c) and (d) this comparison of x and y cannot be made that easily as the track slopes were calculated with multiple x and y coordinates.

The observed coordinate resolutions of the x coordinate amount to about 20 μm and 115 μm respectively for the resolution of the x coordinate of IT and OT tracks are consistent with the expected resolutions of $40\mu\text{m}/\sqrt{N}$ and $200\mu\text{m}/\sqrt{N}$ respectively, with N the number of measurement planes in a station.

In Fig. 4.17 the average track parameter errors are plotted as a function of curvature. Also here the errors from IT and OT are plotted separately.

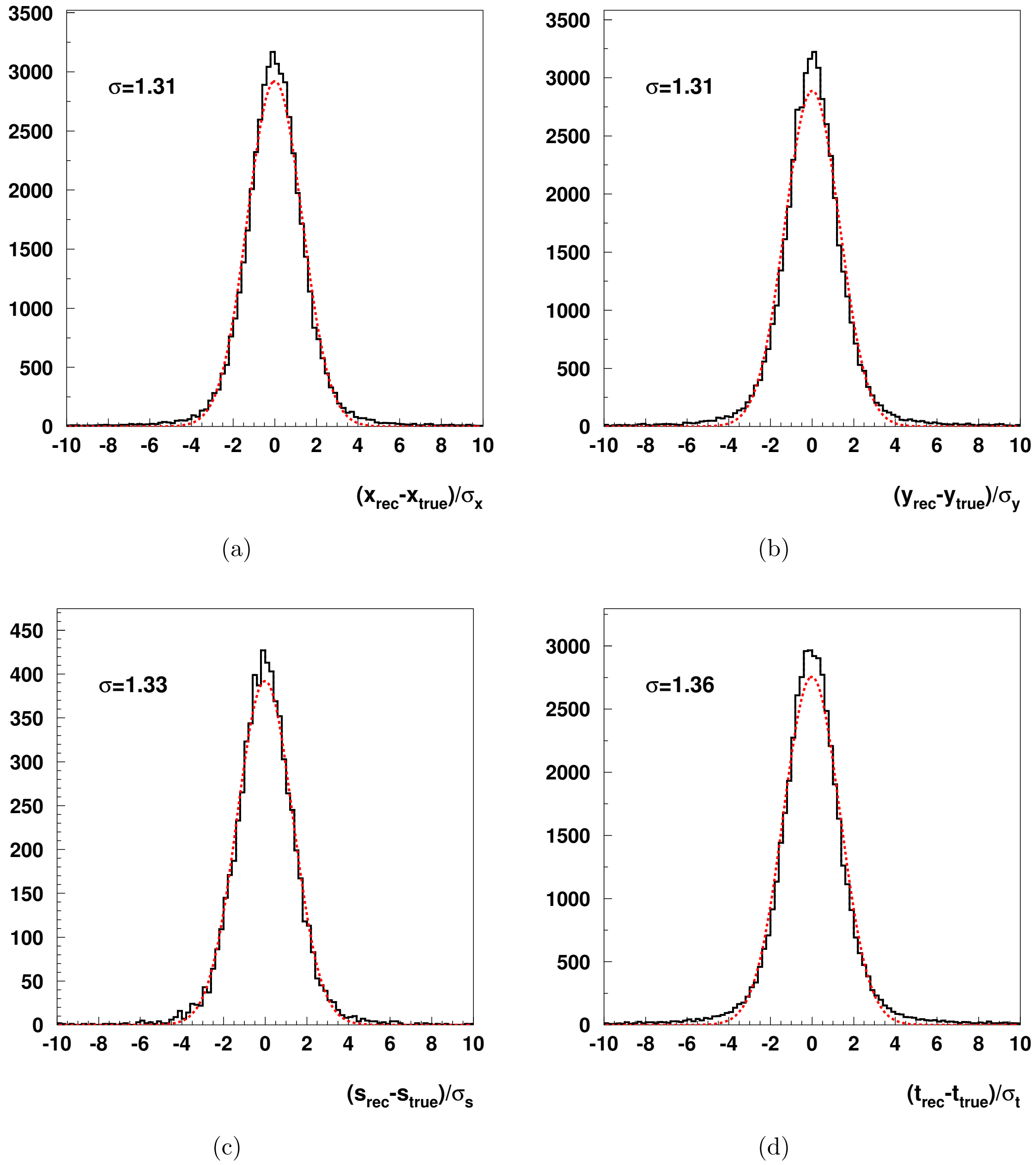

Figure 4.13: *Pull distributions of the trackstate (a) x coordinate (b) y coordinate and the slopes (c) $s = \partial x/\partial z$ and (d) $t = \partial y/\partial z$. Long MC particles have been used.*

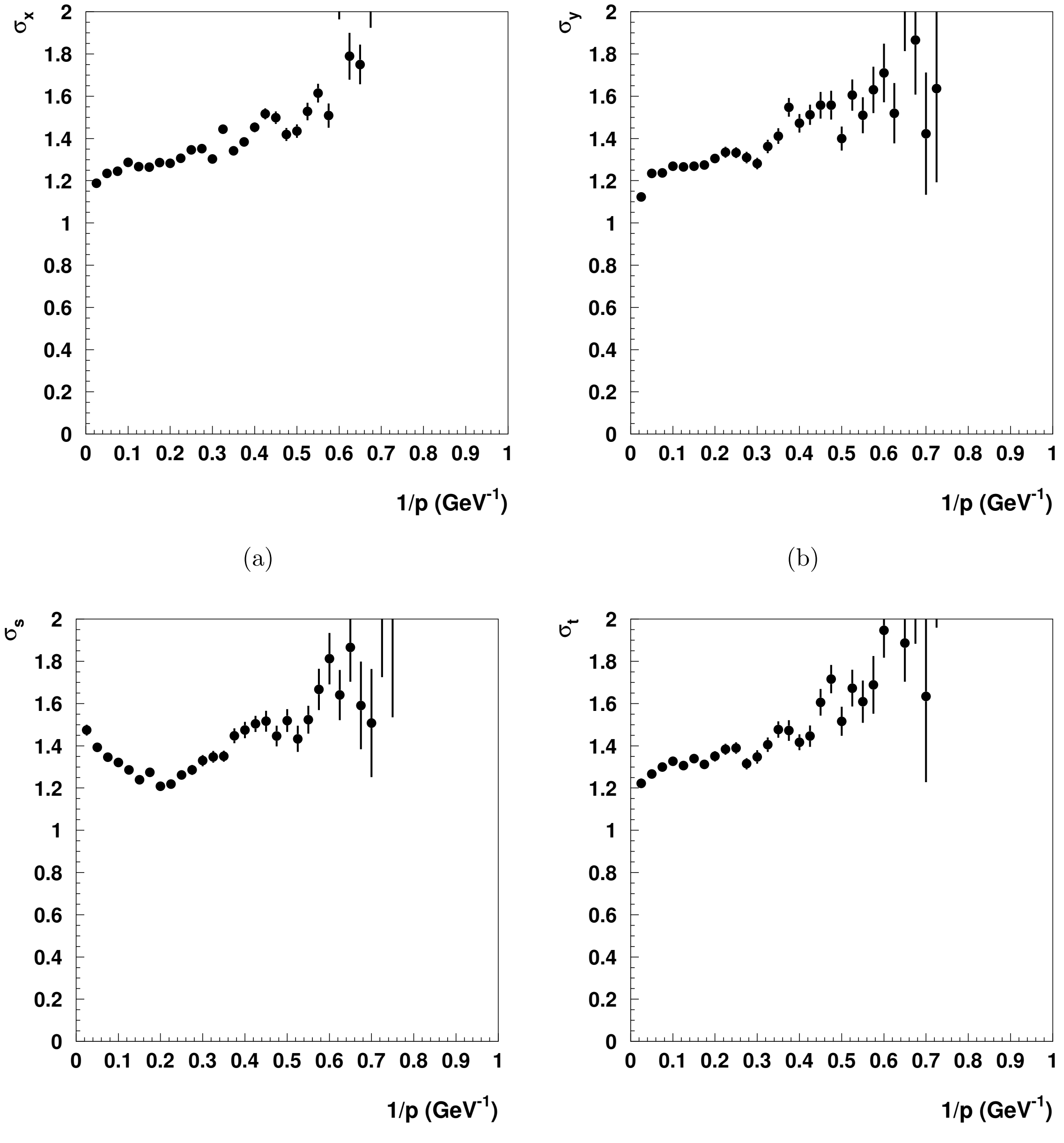

(a) (b) (c) (d)

Figure 4.14: *Width of the parameter pull versus the inverse MC truth momentum for the trackstate (a) x coordinate (b) y coordinate and the slopes (c) $s = \partial x/\partial z$ and (d) $t = \partial y/\partial z$. Long MC particles have been used.*

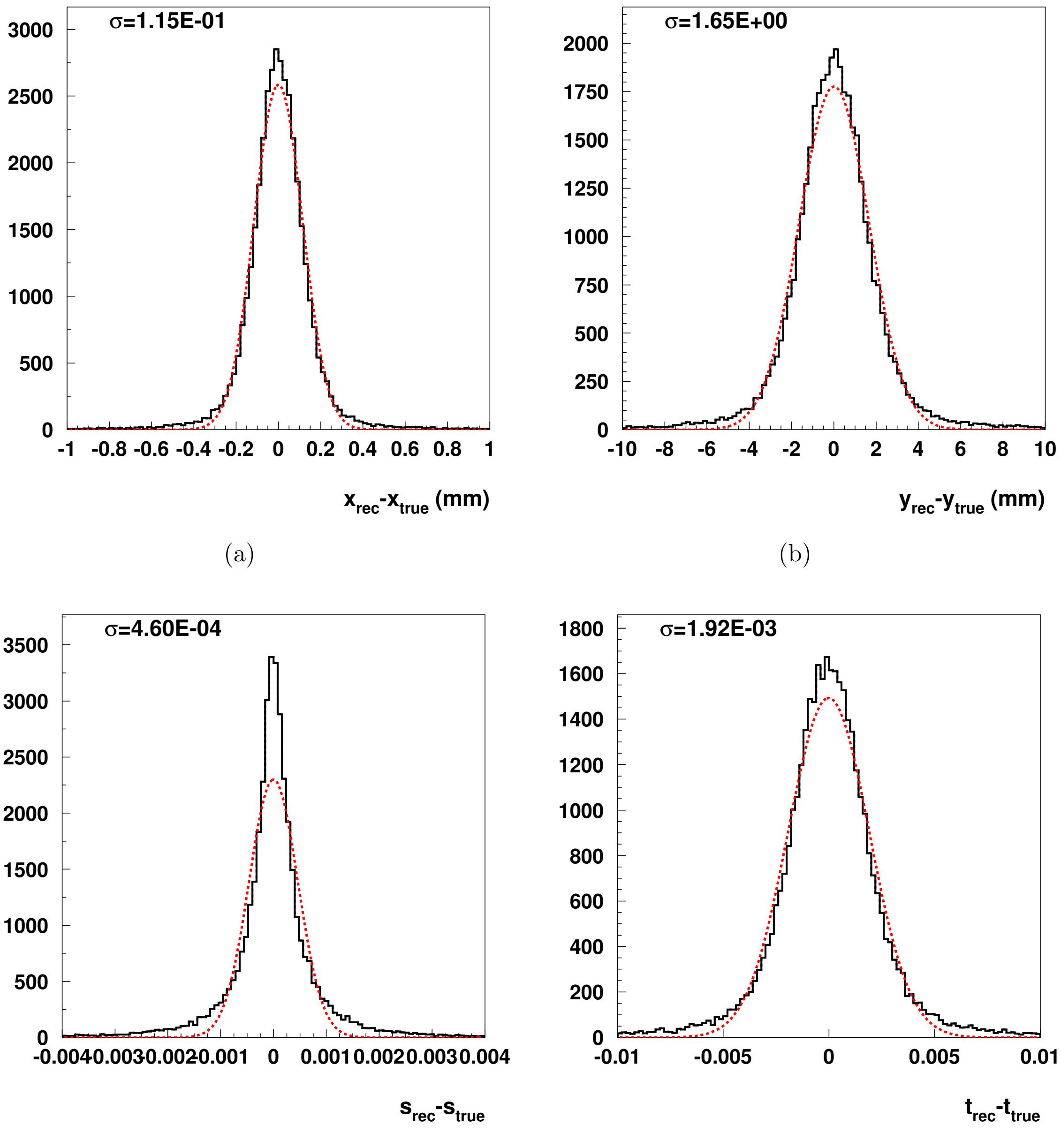

(a) (b) (c) (d)

Figure 4.15: *For tracks with >80% OT hits the resolutions of the trackstate (a) x coordinate (b) y coordinate and the slopes (c) $s = \partial x/\partial z$ and (d) $t = \partial y/\partial z$. Long MC particles have been used.*

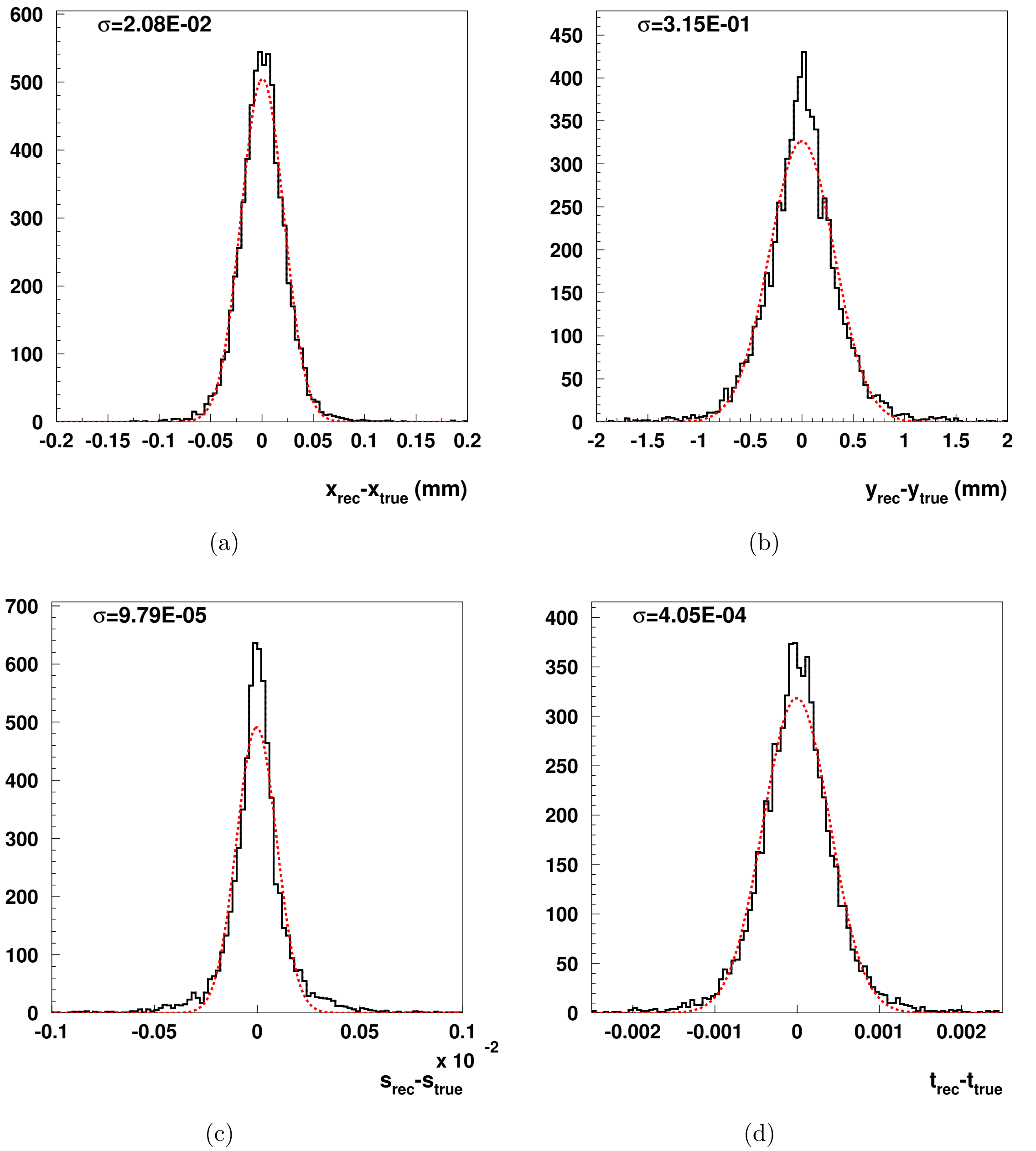

Figure 4.16: *For tracks with >80% IT hits the resolutions of the trackstate (a) x coordinate (b) y coordinate and the slopes (c)* $s = \partial x/\partial z$ *and (d)* $t = \partial y/\partial z$*. Long MC particles have been used.*

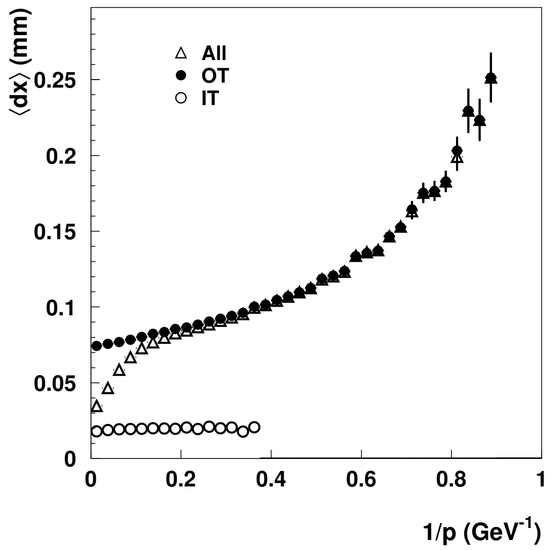

(a)

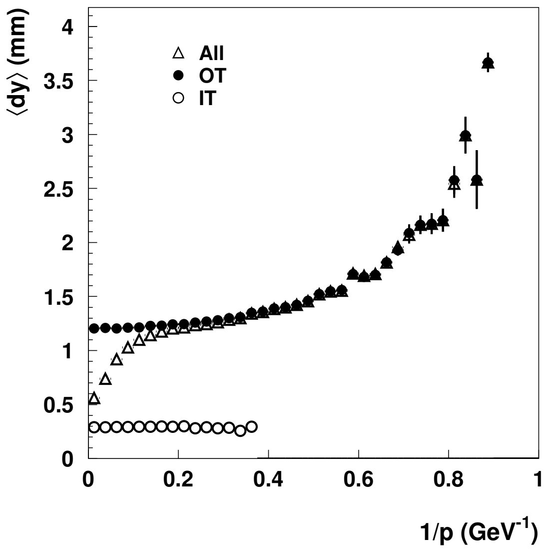

(b)

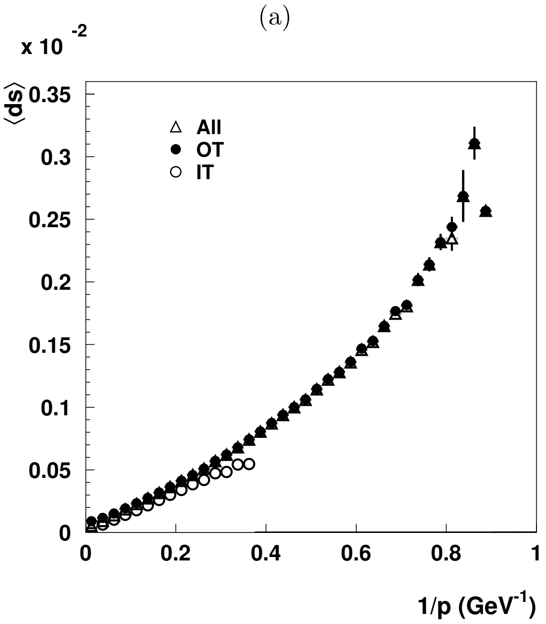

(c)

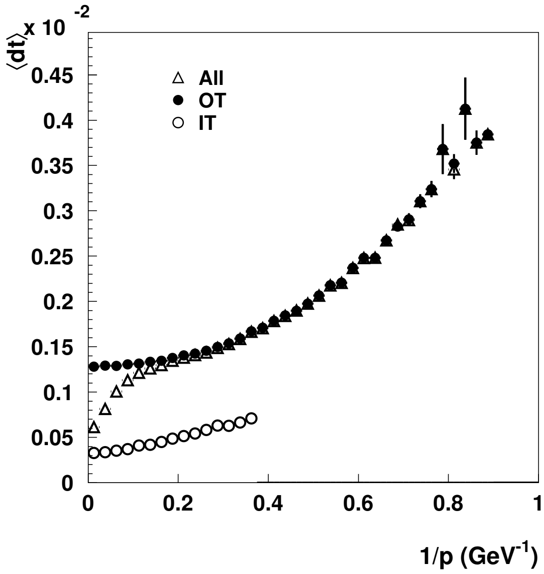

(d)

Figure 4.17: *Error distributions of the trackstate versus the inverse of the MC truth momentum for (a) x coordinate (b) y coordinate and the slopes (c)* $s = \partial x/\partial z$ *and (d)* $t = \partial y/\partial z$*. Long MC particles have been used.*

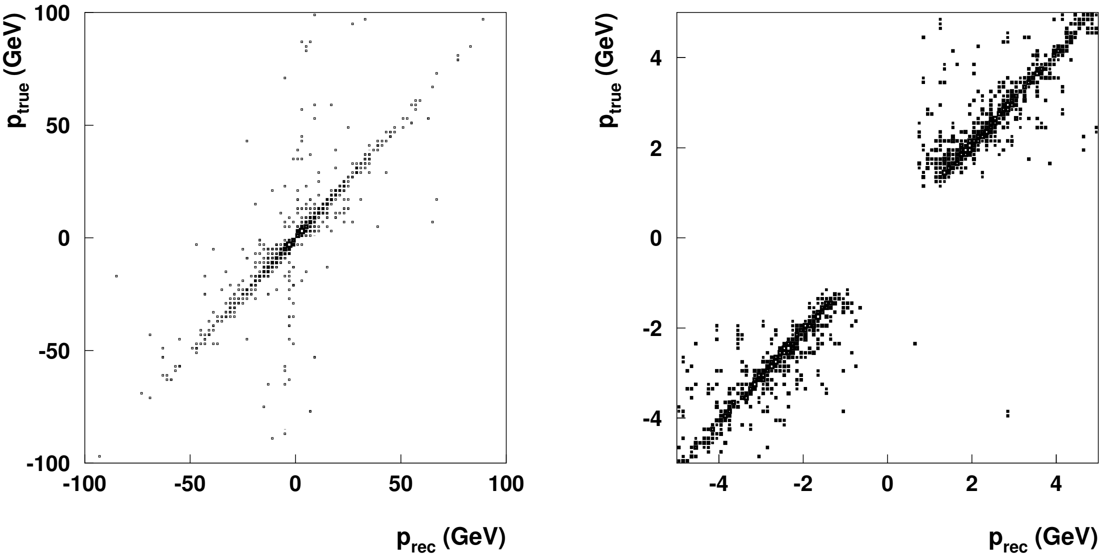

(a) (b)

Figure 4.18: *(a) The momentum estimate of the seed tracks from their curvature* (4.3) *versus the momentum of the corresponding MC particle. (b) A zoom of the region from -5 to 5 GeV.*

4.4.5 Curvature and initial momentum estimate

The momentum of the track candidates can be reconstructed from their curvature using (4.3). In Fig. 4.18 the reconstructed momentum (p_{rec}) of the tracks is plotted against the correct momentum of the associated MC particle (p_{true}). As can be seen in the figure the reconstructed momentum of the seed tracks does not fall below 1 GeV/c. This was explained in Sec. 4.3.2 to be due to the finite size of the search windows to reduce wrong hit combinations.

In Fig. 4.19(a) the residual distribution of the reconstructed momentum is shown. As can be seen in the figure the momentum residual distribution has a bias caused by an overestimation of the absolute momenta of the candidates. In the pull distribution of the momentum in Fig. 4.19(b) the overestimation is also visible; negative momenta become more negative and positive momenta become more positive. From distribution in 4.19(a) the average bias in the momentum resolution is determined to be 2.5%.

In Fig. 4.20 a correction for the overestimation of 2.5% is applied ($p_{cor} = p_{rec} \times 0.975$). The pull distribution in Fig. 4.20(a) is now only a single Gaussian centered around zero. The momentum resolution estimation shown in Fig. 4.20(a) also has become slightly better.

The momentum resolution versus the reconstructed momentum is plotted in Fig. 4.21. The momentum resolution ranges from $\delta p/p = 1.8\%$ at low momenta to $\delta p/p = 6.0\%$ at high momenta. These values are about an order of magnitude greater than the values from long tracks given in [41], and as will be summarised in the next section. The

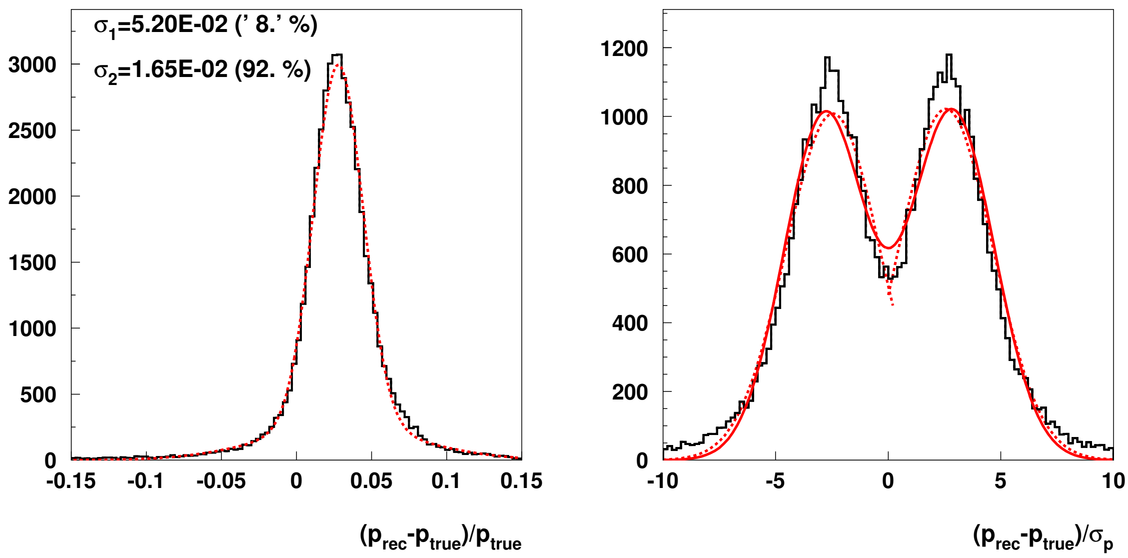

(a) (b)

Figure 4.19: *(a) Reconstructed momentum residual distribution and (b) the reconstructed momentum pull distribution.*

integrated magnetic field in the T station region is lower than the total field, 0.245 Tm vs 4.2 Tm. This means that the bending power and momentum resolution will also be affected.

4.5 Long tracks

The long tracks mentioned in Sec. 4.2 are reconstructed in two ways: By combining VELO tracks with T tracks or by adding T station hits directly to extrapolated VELO tracks [71]. The efficiency and ghost rate performance of long track reconstruction is shown in Figs. 4.22. For long tracks with a momentum higher than 10 GeV the average efficiency is 94%, which can be seen in Fig. 4.22(a). The ghost rate for long tracks is shown in Fig 4.22(b). From the plots it is clear that low momentum particles are more difficult to reconstruct. The main reason for this is that the multiple scattering leads to larger uncertainties at lower momenta. Search windows for low momentum particles therefore have to be larger, leading to a higher ghost rate [41].

The distribution of total number of hits assigned to tracks is visible in Fig. 4.23(a). It shows a double structure; the smaller peak arising due to tracks traversing the IT, the larger peak due to tracks passing the OT. The hit purity of long tracks is displayed in Fig. 4.23(b). On average 98.7% of the hits on a long track is correctly assigned. This implies on average 0.5 hits are wrongly assigned for long tracks. The momentum resolution of long tracks as a function of momentum is plotted in Fig. 4.24. It ranges from $\delta p/p = 0.35\%$ at low momenta to $\delta p/p = 0.55\%$ at high momenta.

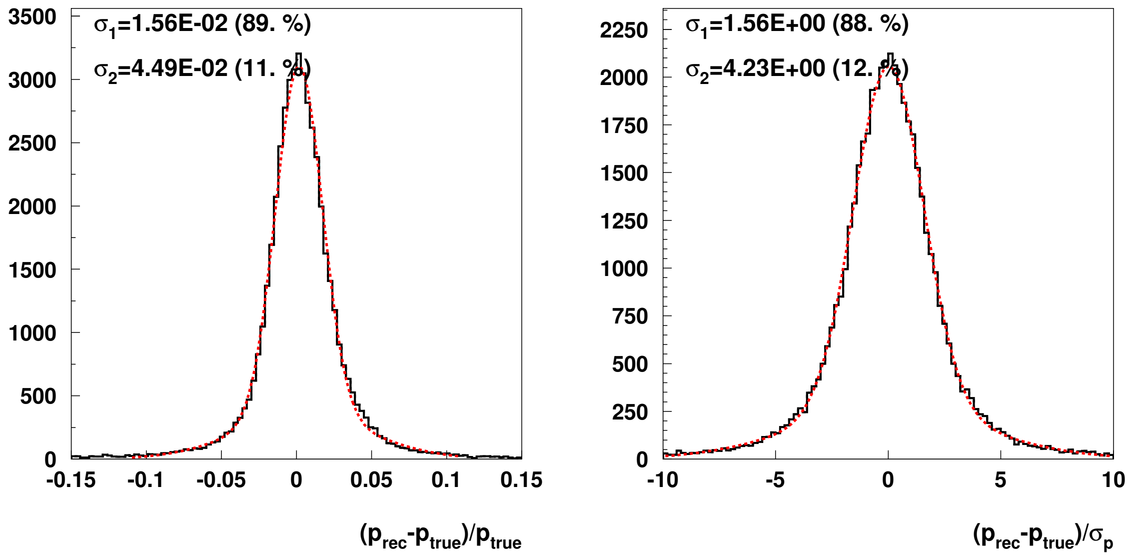

(a) (b)

Figure 4.20: *(a) Corrected reconstructed momentum residual distribution and (b) the corrected reconstructed momentum pull distribution.*

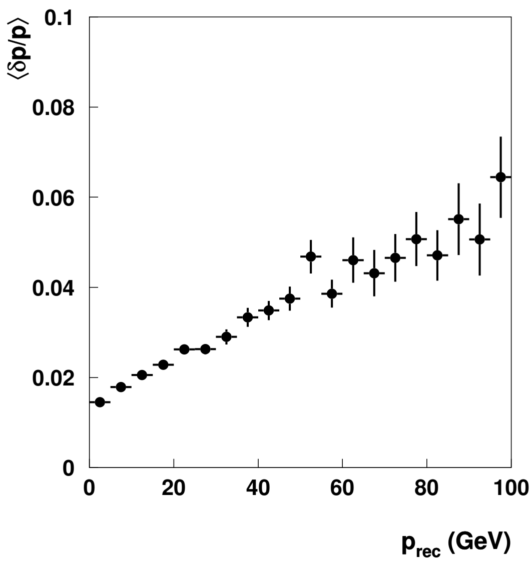

Figure 4.21: *Corrected momentum resolution versus the reconstructed momentum.*

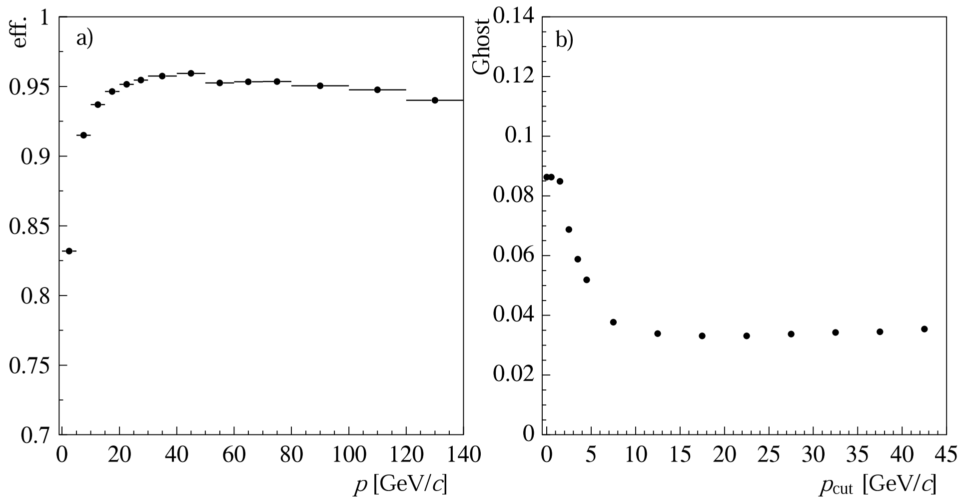

Figure 4.22: *Performance of the long track finding: (a) efficiency as a function of the momentum; (b) ghost rate, for tracks with reconstructed momentum greater than p_{cut}. Figures from [41].*

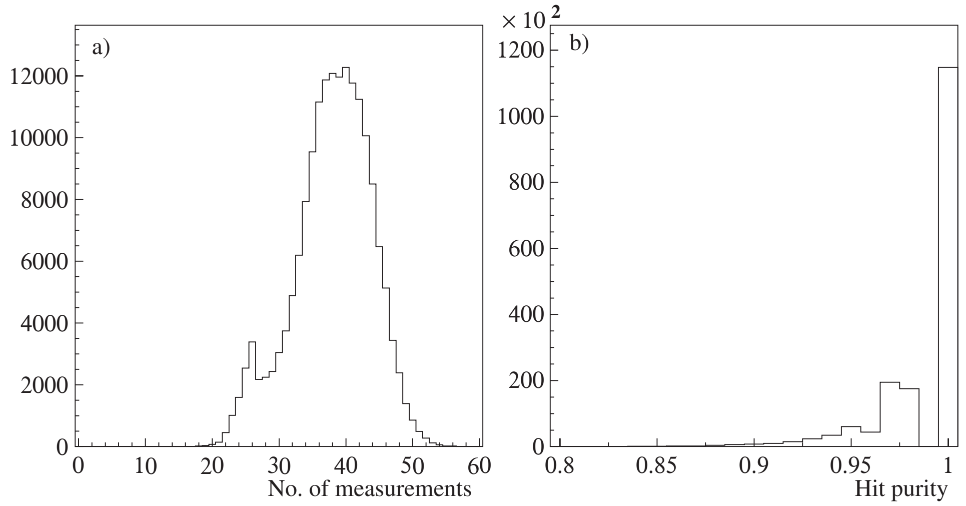

Figure 4.23: *(a) The number of detector measurements assigned to reconstricted long tracks; (b) the fraction of correctly assigned hits for long tracks. Figures from [41].*

4.6 Conclusions

A pattern recognition algorithm for the T stations is described. The formation of the tracks, the inclusion of 3 dimensional information from the tracker stations is given. Also the bending of tracks is estimated with the help of the knowledge of the magnetic field in the bending plane in the T stations. A prediction of the track trajectory is compared to the actual hit coordinates, and a likelihood is calculated per track. This

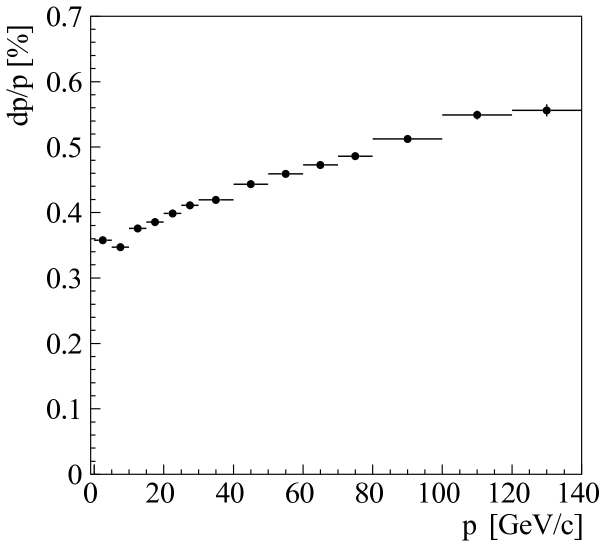

Figure 4.24: *Momentum resolution as a function of track momentum. Figure from [41].*

enables an estimation of how likely it is that the track is due to a real particle or due to a random combination of hits.

In the second part of the chapter the performance of the algorithm is given in terms of efficiency, ghostrate and parameter resolutions. The track efficiency as well as the ghost rate is given as a function of the true momentum of the particles. The dependence at low momenta maybe explained by multiple scattering which is not taken into account by the pattern recognition.

The track parameter pull distributions are fitted with a single Gaussian function with a width slighly larger than 1. This behaviour may be attributed at low momenta to multiple scattering. At higher momenta the track event model, which uses a parabolic track, might not represent tracks completely correctly.

The coordinate resolutions of the tracks in the middle of the T stations are fitted with a double Gaussian distribution. The double structure is choosen to represent IT and OT measurements. The standard deviations of the two fitted Gaussians are found to be 30 μm and 130 μm for the x-coordinate measurements. The single hit resolutions of the IT and OT detector elements are expected to be around 40 μm and 200 μm respectively. Also the error distributions of the trackparameters are shown to contain two components. Since the pull distributions can be fitted with a single Gaussian, this means that the error is calculated in a consistent way. However due to the width of the pull distributions, the error might be underestimated.

The momentum pull distribution and resolution are also investigated. An unexpected double structure can be seen in the pull distribution, while the distribution of the resolution is shifted from zero. This behaviour is attributed to an overestimation of the absolute momentum from the curvature of the tracks. A correction is applied by requiring the resolution to centre around zero. It shows that the absolute momentum was overestimated by about 2.5%.

With the tracks from the T station pattern recognition algorithm also a momentum resolution dependence on the reconstructed momentum is investigated. From the corrected distributions the momentum resolution ranges from $\delta p/p = 1.8\%$ at low momentum to $\delta p/p = 6.0\%$ at high momentum.

In the last section distributions from a long track sample are taken from the reoptimisation TDR [41]. Comparing the distributions of the efficiency and ghost rate a similar shape is observed, although the values are lower and higher respectively. Also for the long tracks the number of measurements has a double structure due to IT and OT measurements. The purity distribution shows similar fractions of correct hits. The momentum resolution as function of the momentum for long tracks is about an order of magnitude lower. This may be attributed to the magnetic field that the particles traverse which is 4.2 in the case of long tracks versus 0.245 Tm for the T tracks.

5

Selection of $B^0 \to K^*(892)^0(K^+\pi^-)\mu^+\mu^-$

The decay $B^0 \to K^*(K^+\pi^-)\mu^+\mu^-$ studied in this thesis has observables that are sensitive to new physics scenarios. This decay channel has already been subject to interest within LHCb *e.g.* [72, 73, 74]. The polar angle, θ_l, between the negative muon and the dimuon helicity axis in the dimuon rest frame, is used to determine the amount of events with a forward ($|\theta_l| < \pi/2$) or backward ($|\theta_l| > \pi/2$) going muon. The angle θ was defined in Fig. 1.4 (chapter 1).The asymmetry in this number depends on the dimuon invariant mass squared, s. This asymmetry changes in new physics models, as is shown in Sec. 1.5.

The final state includes a K^*, which[1] is a vector meson produced in the weak decay of the pseudo-scalar B^0. In the partonic interpretation in the SM the $(V-A)\times(V-A)$ structure[2] of the weak coupling causes the s quark to be predominantly left-handed polarised as explained in chapter 1. Combined with the spin of the spectator quark the helicity of the K^* is either -1 or 0, as is the helicity of the muon pair. The K^* is reconstructed in the experimentally accessible decay to $K^+\pi^-$.

The B^0-decay has a final state of four charged particles only. The pattern recognition, using the tracking detectors, and subsequently the track fitting are used to reconstruct the four-vectors of the produced particles. These reconstructed tracks are in turn augmented with particle identification information. Next the reconstructed final state particles belonging to the decay $B^0 \to K^*(K^+\pi^-)\mu^+\mu^-$ are selected using optimised kinematical criteria. The event reconstruction and selection dor the decay are described in [76] and are reproduced here.

[1]There are also searches with a pseudoscalar particle in the finalstate, $B^0 \to K_S\mu\mu$, *e.g.* [75]. For this decay the standard model predicts a negligibly small forward-backward asymmetry, which, however, may be enhanced by new physics. The experimental search involves K_S particles which are more difficult to reconstruct at LHCb with respect to the K^* [41].

[2]This can be seen from the double W-couplings in Figs. 1.1(a,b).

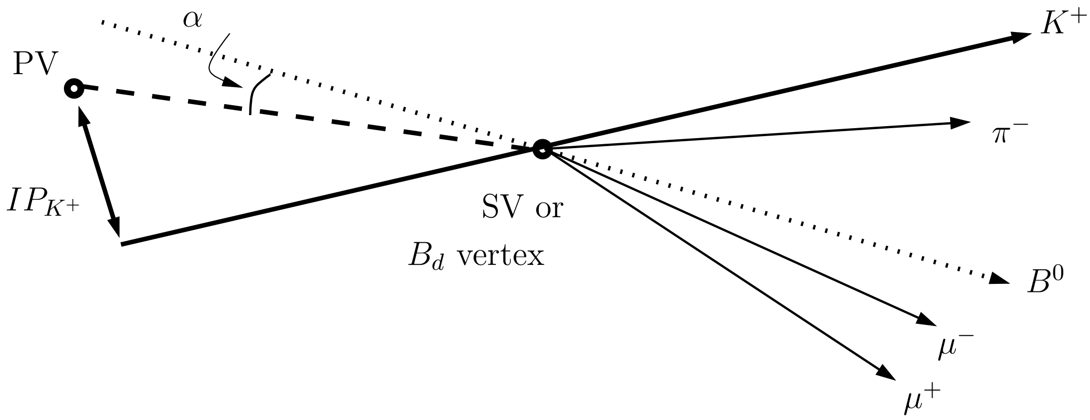

Figure 5.1: *Topology of the production and decay of $B^0 \rightarrow K^{*0}(K^+\pi^-)\mu^+\mu^-$, with the reconstructed tracks shown as plain lines, and the B^0-meson direction shown as a dotted line. The only impact parameter (IP) shown is the IP for the K^+-meson. The flight angle between the reconstructed B-meson direction and the line between primary and secondary vertex is denoted α.*

5.1 Reconstruction

The final state of $B^0 \rightarrow K^*(K^+\pi^-)\mu^+\mu^-$ consists of two muons, a charged kaon and a charged pion. Charged tracks generally leave hits in all parts of the detector, hence long tracks are reconstructed. The charged particle reconstruction uses PID information from the subdetectors to determine the particle types.

The vertices that are reconstructed are the primary vertex (PV) where the pp interaction takes place and the secondary vertex (SV) where the B-meson decays. Subsequently an impact parameter (IP) is calculated for each track, defined as the distance of closest approach of that track and the primary vertex. The impact parameter is illustrated for a K^+ track in Fig. 5.1. The impact parameter significance (IPS) is the IP divided by the uncertainty σ_{IP} obtained in a vertex fit procedure, $IPS = IP/\sigma_{IP}$.

The momenta of the K, π and μ particles in the signal decay should not point back to the primary vertex, therefore their impact parameter significance is required to be large. In events with multiple PV's conservatively the smallest IPS (sIPS) is used. The impact parameter significance, rather than the plain impact parameter, is used, as it takes the track error into account. Tracks which have a large uncertainty *e.g.* low momentum tracks with a long extrapolation between the first and the last measurement and the primary vertex will have a reduced IPS and are therefore rejected.

In the experiment the trigger will perform the first stage of the selection, reducing the event rate to produce a manageable datastream to disk. In the simulation this first step is described by a preselection. However, the preselection and trigger do not coincide completely as the preselection is also used for the trigger optimalisation. The preselection therefore uses more loose criteria. Before the final selection of events a trigger simulation is run to reduce the event rate to the final value. On the preselected data a more stringent final selection is performed. The final selection is optimised for maximise signal over the square root of the background ratio ($S/\sqrt{B}$) in [76, 73]. The kinematical requirements are summarised in Table 5.1 and will be briefly discussed below.

After the events with final state particles have been selected, the resonances are reconstructed. The first resonance is the K^* which is the combination of a kaon and a pion. The muons are combined together within a wide mass range. The last resonance to be reconstructed is the B^0 meson which is made from the K^* and the dimuon combination. The individual selection rules for each particle or resonance will be highlighted below.

5.2 Selection criteria

The K^* selection uses the reconstructed kaon and pion candidates. First, both the kaon and the pion are required to have an impact parameter significance with respect to the primary vertex of at least 3.0 standard deviations. This will reduce most of the K^* mesons originating from the primary vertex. Second, a mass window of ± 100.0 MeV is placed around the K^* mass of 896 MeV. The K^* resonance has an intrinsic width of about 50 MeV [77] such that the selection window is four times the FWHM of the K^* mass distribution. Third, the minimum transverse momentum is set to a value of 300 MeV in order to reject low momentum particles from uncorrelated sources. The K^* decays strongly, and thus all four tracks from the B^0 originate from the same secondary vertex. The χ^2/dof of[3] the K^* vertex is tightened to 25/1.

The two muons are combined and the resulting invariant mass is selected within a wide mass window. Effectively no restriction is placed on the invariant mass[4]. The mass-window requirement is chosen as loose as possible since the dimuon pair originating from the signal decay has a large spread in invariant mass. The distribution of the dimuon mass before and after the final selection is plotted in Fig. 5.2. The combination of the two muons is required to have a vertex fit with a maximum χ^2/dof of 15.0/1 to prevent two uncorrelated muons to be selected. The $J/\psi(1S)$ and $\psi(2S)$ resonances are removed from the selection to reject the decays of the type $B^0 \to J/\psi K^*$.

The final B^0-resonance is constructed using the resonances of the K^* and the dimuon. A mass window of ± 100.0 MeV is required around the B^0 meson mass. The vertex fit for the B^0 from the K^*-candidate and the dimuon candidate is required to have a maximum χ^2/dof of 20.0, the maximal impact parameter significance of the flight path of the B^0 is choosen to be 5.0 standard deviations.

The flight angle between the reconstructed B-track and the line between primary and secondary vertex is denoted α in Fig. 5.1. The cosine of the angle is restricted to

[3]The number of degrees of freedom for an n-prong vertex is equal to $2n - 3$.

[4]The invariant mass window is set to ± 3000.0 MeV around the J/ψ mass, resulting in the loose selection of $0 < q^2 < 36$ GeV^2.

Restriction	Preselection	Final Selection
B^0 mass window	± 500 MeV	± 50 MeV
B^0 p_T	> 250 MeV	> 250 MeV
B^0 vertex χ^2	< 30	< 20
B^0 cos(angle)	> 0.995	> 0.99975
B^0 FS	> 6	> 6
B^0 smallest IPS	< 1000	< 5
$K^*(892)^0$ mass window	± 300 MeV	± 100 MeV (2 FWHM of K^* mass distribution)
$K^*(892)^0$ p_T	> 300 MeV	> 300 MeV
$K^*(892)^0$ vertex χ^2	< 25	< 25
$K^*(892)^0$ sIPS	> 1.5	> 1.5
$K^*(892)^0$ FS	$-$	> 1
$K^\pm$ p	> 2000 MeV	> 2000 MeV
$K^\pm$ p_T	$-$ MeV	> 400 MeV
$K^\pm$ sIPS	> 1.5	> 3.0
$\pi^\pm$ p	$-$	> 2000MeV
$\pi^\pm$ p_T	$-$	> 250 MeV
$\pi^\pm$ sIPS	> 1.5	> 3.0
$\mu\mu$ mass window	± 3000.0 MeV	rejection of 2900–3200 MeV & 3650–3725 MeV
$\mu\mu$ vertex χ^2	< 10000	< 15
$\mu^\pm$ p	> 4000 MeV	> 4000 MeV
$\mu^\pm$ p_T	> 300 MeV	> 500 MeV
$\mu^\pm$ sIPS	> 0.5	> 2.0

Table 5.1: *Kinematic preselection and selection criteria for the decay $B^0 \to K^*\mu^+\mu^-$. Taken from [76].*

a minimum of 0.99975. This ensures collinearity[5] of the flight direction (from primary vertex to secondary vertex) and the momentum of the reconstructed B^0-candidate, since the flight direction and the momentum vector are expected to be parallel for true particles.

The flight significance (FS) is defined as the distance between the B^0-decay vertex and the PV divided by the reconstruction uncertainty on this distance. In events with more than one PV the PV is conservatively chosen as the one with which the B^0 has the smallest IP. The flight significance of the B^0 is required to be larger than 6 standard deviations, in order to reject combinatorial background consisting of tracks originating from the primary vertex.

[5]Collinearity between two vectors can be written in terms of an inner product, $\mathbf{x} \cdot \mathbf{y} = |x||y| \cos\theta$. Hence the cosine of the angle is the natural way to determine the collinearity.

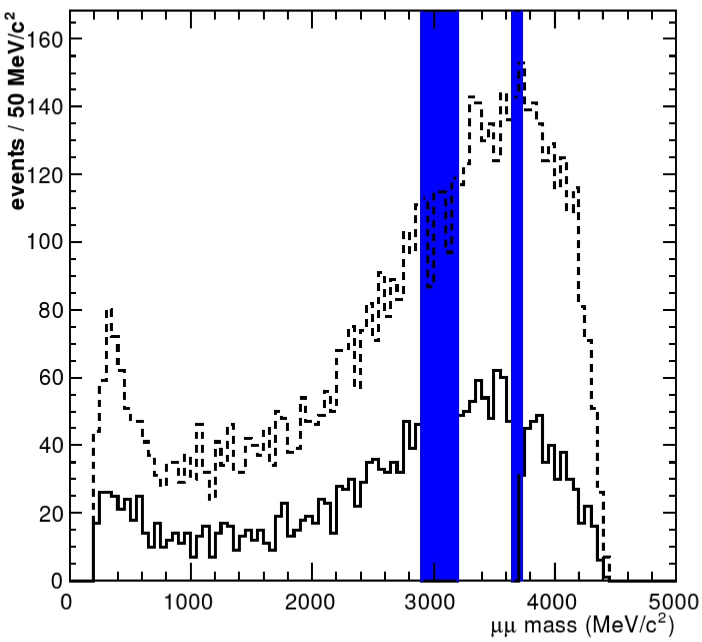

Figure 5.2: *Reconstructed $\mu\mu$ mass distribution before (dashed) and after (solid) final selection. The shaded areas show the regions of the $J/\Psi(1S)$ and $\psi(2S)$ rejections. Figure adapted from [76].*

5.3 Event yields

The estimated signal event yield in LHCb for a total $b\bar{b}$ data collection of 2 fb^{-1} per year is calculated by multiplying the total $b\bar{b}$ yield ($N_{b\bar{b}}$) by the hadronisation fraction of B^0-mesons (f_{B^0}) times the branching ratios (BR) and the trigger efficiency (ϵ_{tr}) and the combined reconstruction and selection efficiency ($\epsilon_{r,s}$) [76] as

$$S = N_{b\bar{b}} \times 2 \times f_{B^0} \times BR(B^0 \to K^{*0}\mu\mu) \times BR(K^{*0} \to K^+\pi^-) \times \epsilon_{tr} \times \epsilon_{r,s}. \tag{5.1}$$

The $b\bar{b}$ yearly yield estimate was calculated in chapter 2 to be $N_{b\bar{b}} = 10^{12}$. The fraction of $b\bar{b}$ events hadronising to B^0 or $\bar{B}^0$ is $f_{B^0} = 0.398$. The branching ratios of the subsequent decays are $BR(B^0 \to K^{*0}\mu\mu) = 1.22^{+0.38}_{-0.32} \times 10^{-6}$ and $BR(K^{*0} \to K^+\pi^-) = 0.67$. The trigger efficiency was estimated [41] to be $\epsilon_{tr} = 0.89$. The combined reconstruction and selection efficiency is estimated [76] to be $\epsilon_{r,s} = 0.0126 \pm 0.0003$.

The annual event yield for the decay $B^0 \to K^*\mu^+\mu^-$ amounts to $7200 \pm 180^{-1900}_{+2200}$. The first error is due to the statistical uncertainty on the number of selected events and the second error is the measured uncertainty on the branching ratio.

Sample		Annual yield: Before L0 and L1	Annual yield: After L0 and L1	Trigger efficiency
$B^0 \to s\mu^+\mu^-$	Non-resonant	2020 ± 80	1730 ± 75	86%
	All other	24 ± 10	20 ± 7	83%
$B_u \to s\mu^+\mu^-$		11 ± 3	9 ± 3	81%
$b \to \mu^-,\ \bar{b} \to \mu^+$		1230 ± 270	1050 ± 250	85%
$B_d \to \mu^+ c(\to \mu^-)$		210 ± 120	70 ± 70	33%
$B_u \to \mu^+ c(\to \mu^-)$		630 ± 180	470 ± 160	75%
$B_s \to \mu^+ c(\to \mu^-)$		$< 110\,@\,90\%\,CL$	–	–
$\Lambda_b \to \mu^+ c(\to \mu^-)$		120 ± 50	100 ± 50	83%
Total background		4200 ± 350	3500 ± 320	83%
Signal		8130 ± 2300	7200 ± 2100	89%
B/S		0.5 ± 0.2	0.5 ± 0.2	

Table 5.2: *Summary of the expected annual background yields for the signal $B^0 \to K^{0*}\mu^+\mu^-$ calculated in [76].*

5.4 Background categories

The most prominent background is due to muon pairs originating from resonances such as $J/\psi(1S)$ and $\psi(2S)$ [76]. However, these resonances have a well defined width and can therefore be excluded from the invariant dimuon mass spectrum.

Events arising from the non-resonant process $B^0 \to K^\pm\pi^\mp\mu^+\mu^-$ are expected to contribute to the forward-backward asymmetry for certain regions of phasespace. Also the value of the invariant dimuon mass squared, s, at which A_{FB} vanishes, can change with the invariant mass of the $K\pi$ system [78]. The expectation is that in the standard model the non-resonant events have a zeropoint of A_{FB} that is equal to the resonant signal [76]. It is at present not clear how to include these events, therefore the non-resonant contribution is not included in the simulation and selection.

A summary of the expected background event rates is reproduced in Table 5.2. The total annual background after the trigger is expected [76] to be around 3500 ± 320 of which 1730 ± 75 is non-resonant background[6] ($B^0 \to K^\pm\pi^\pm\mu^+\mu^-$). The second largest background originates from the semileptonic decay of both the b and $\bar{b}$-quark in the event. Together with the estimated signal yield from the selection gives an B/S of 0.5 ± 0.2.

[6]This number is an estimation with a branching fraction of BR($B_d \to K^\pm\pi^\mp\mu^+\mu^-$)=$1 \times 10^{-6}$ [76].

6

Systematic selection effects on A_{FB}

The analysis of the forward-backward asymmetry (A_{FB}) in the decay $B^0 \to K^{*0}\mu^+\mu^-$ involves the observables described in Sec. 1.4: the polar angle between the negative muon and the dimuon helicity axis in the dimuon-rest frame, θ_l, and the dimuon invariant mass squared, s. The event selection can possibly influence the distribution of these variables. Such an influence, in turn, could alter the forward-backward asymmetry as a function of s. The distributions of the two observables are evaluated for possible biases when subjecting the events to the selection procedure. For all studies the invariant mass of the two muons was selected to be below the J/ψ mass, $\sqrt{s} < 2900$ MeV.

6.1 Datasets

To evaluate possible selection induced biases on the asymmetry two Monte Carlo samples were used; a signal sample and a dimuon inclusive background sample.

The signal decay[1] products are selected at generator level within a cone of 400 mrad around the beam axis for an efficient event generation in the LHCb acceptance. The signal sample has a size of 4×10^5 events which corresponds to an integrated luminosity of 27 fb^{-1}, equivalent to 13.5 nominal years of data.

The background consists of an inclusive dimuon sample[2]. It was obtained by requiring two muons with opposite charge to be within 400 mrad around the beam axis at generator level. The size of the background sample is 2.6×10^7 events which corresponds to a moderate integrated luminosity of 5 pb^{-1}, equivalent to about 1 day of data taking.

[1] The signal sample was generated with Gauss version v25r7, digitised by Boole v12r10 and tracked using Brunel v30r14

[2] For the background an inclusive dimuon sample was used generated with Gauss version v25r10, digitised by Boole version v12r10 and tracked using Brunel v30r17.

6.2 Signal event distributions and efficiencies

The effects of the individual selection steps on the distributions of the polar angle of the positive muon, θ_l, and the dimuon invariant mass squared, s, are investigated. Since the asymmetry of the number of forward-going muons and backward-going muons depends on these two variables, the selection restrictions should not introduce any biases in these distributions.

The effects of the selection procedure are shown below for signal as well as for dimuon inclusive background events. First, the effect of the final event selection on the θ_l and s distributions is discussed. Subsequently the separate selection steps are applied to identify the effect of each step. Then the selection criteria are applied to the background events as will be described in section 5.4. The correlation of the θ_l and s distributions with the reconstructed $K\pi\mu\mu$ invariant mass for the background will be shown last.

6.2.1 Selection Effects

The distribution of the MC-truth value of the polar angle of the negatively charged muon, θ_l^{MC} is displayed in Figs. 6.1(a,b,c) for three different cases. The generator distribution without any selection or acceptance effects is shown in Fig. 6.1(a)[3]. The distribution for the same variable for the preselection only is shown in Fig. 6.1(b). Finally the distribution for the final selected events is given in Fig. 6.1(c). The full event selection procedure causes a distortion of the θ_l distribution, as is shown by dividing the distribution of the final selection in Fig. 6.1(c) by the distribution of the MC truth in Fig. 6.1(a). The resulting efficiency is shown in Fig. 6.1(e) and is not symmetric around $\theta = \pi/2$. This might possibly affect the asymmetry between the number of events with a forward and backward going lepton. In the next section this apparent efficiency will be investigated in separate bins of s.

The distribution of the reconstructed variable θ_l, instead of the true value θ_l^{MC} after the final event selection is shown in Fig. 6.1(d). The number of entries is larger than in the distribution of the true variable θ_l^{MC}, because one event can contain multiple reconstructed decays. For example, an event might have two reconstructed K^+ particles, which both satisfy the selection criteria for the decay $B^0 \to K^*\mu^+\mu^-$, and will give two entries in the histogram.

In Fig. 6.1(f) the ratio of the angular distributions obtained from the reconstructed angle θ_l divided by the true angle θ_l^{MC} is shown. The ratio is flat hence the effect of the reconstruction on the distribution is small. More importantly, the resulting distribution is symmetric around $\theta_l = \pi/2$, and hence the forward-backward asymmetry will not be affected.

Figs. 6.2(a-f) show the distributions of the dimuon invariant mass squared, s. The MC-truth value on generator level (s^{MC}) without acceptance effects is shown in Fig. 6.2(a).

[3]Note that for this study a separate sample was generated, not affected by the standard 400 μrad acceptance.

The distribution after the preselection is shown in Fig. 6.2(b). The final selection procedure leads to the distribution given in Fig. 6.2(c).

The selection does not affect the s-distribution as is shown by the efficiency in Fig. 6.2(e). In Fig. 6.2(d) the distribution of the reconstructed variable s is shown after the final selection. Again, the number of entries is larger than in the distribution of the true variable s^{MC}, because now every candidate is included. The effect of the reconstruction is quantified by dividing the distribution of the reconstructed value s, by the distribution of the true value s^{MC}. In Fig. 6.2(f) the invariant mass squared distribution of fully selected and reconstructed events is divided by the MC truth matched values of the same sample, showing that the effect of the reconstruction on the s distribution is small.

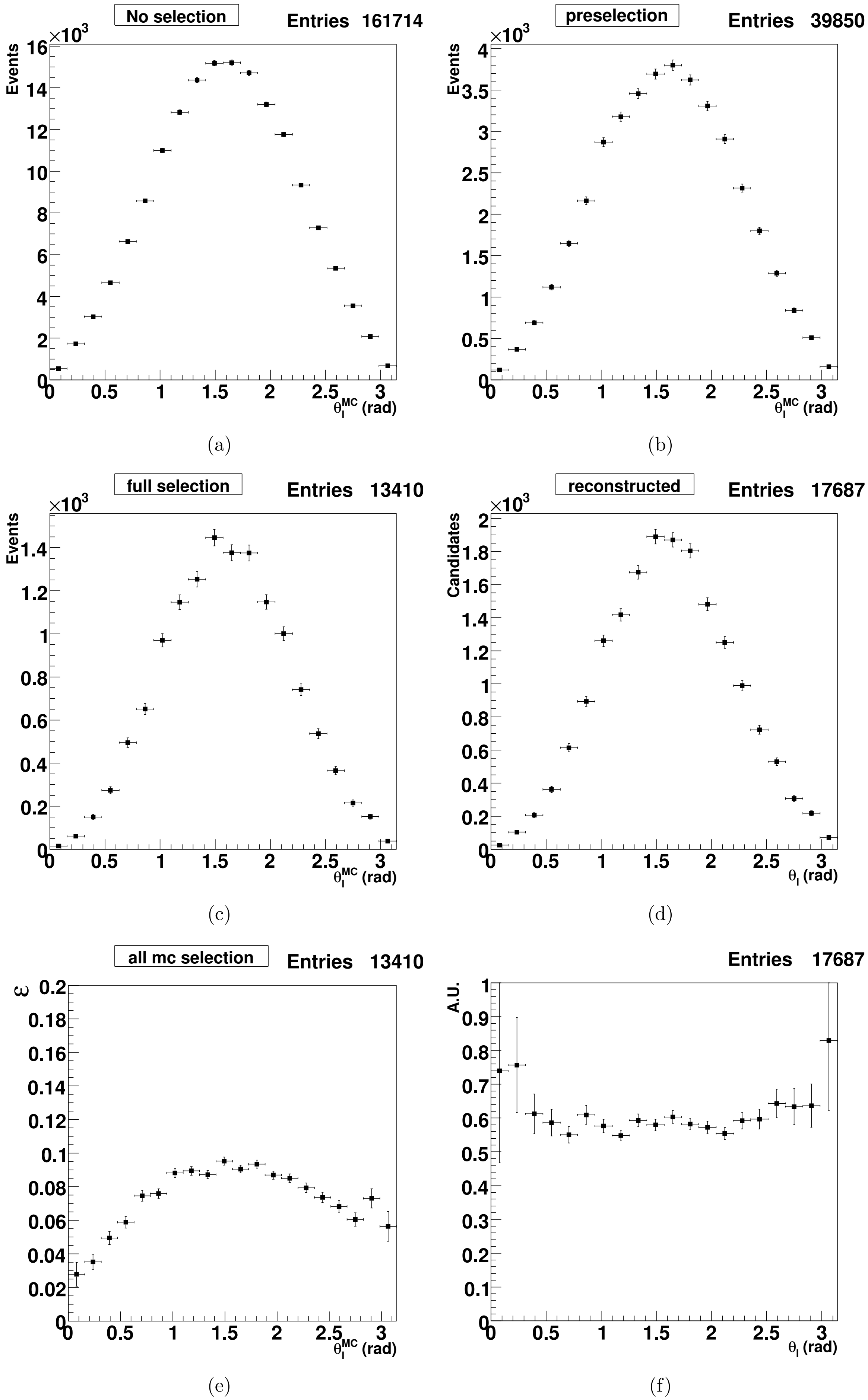

Figure 6.1: *(a) Distribution of the true value of the polar angle, θ_l^{MC}, without selection or acceptance applied. (b) Distribution of θ_l^{MC} after the preselection. (c) Distribution of θ_l^{MC} after the full selection. (d) Distribution of the reconstructed value of the polar angle θ_l after the selection. (e) The selection efficiency: (c)/(a). (f) The effect of the reconstruction quantified by the ratio of reconstructed and true variables: (d)/(c).*

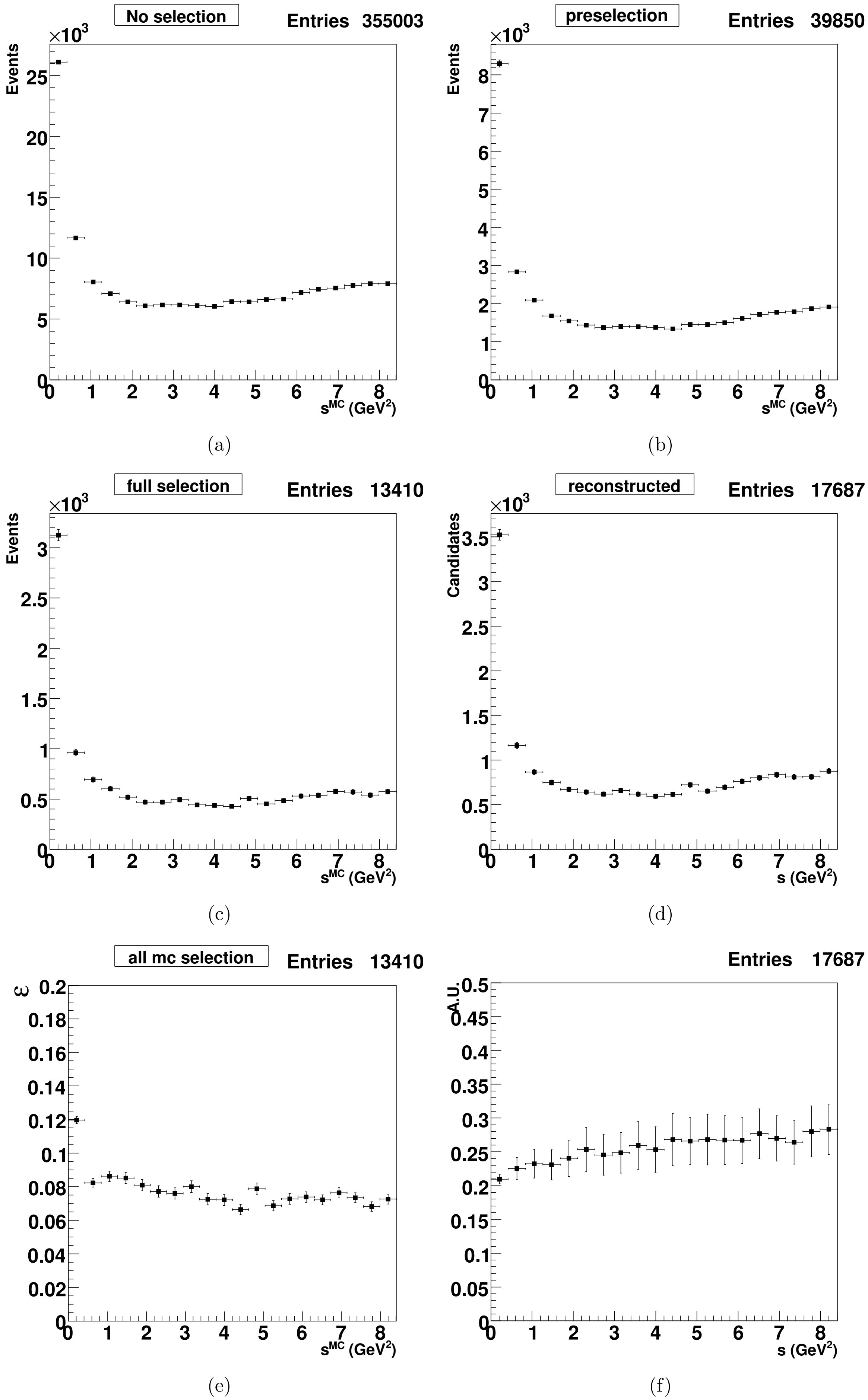

(a) (b) (c) (d) (e) (f)

Figure 6.2: *(a) Distribution of the true value of the invariant mass, s^{MC}, without selection or acceptance applied. (b) Distribution of s^{MC} after the preselection. (c) Distribution of s^{MC} after the full selection. (d) Distribution of the reconstructed value of the invariant mass s after the selection. (e) The selection efficiency: (c)/(a). (f) The effect of the reconstruction quantified by the ratio of reconstructed and true variables: (d)/(c).*

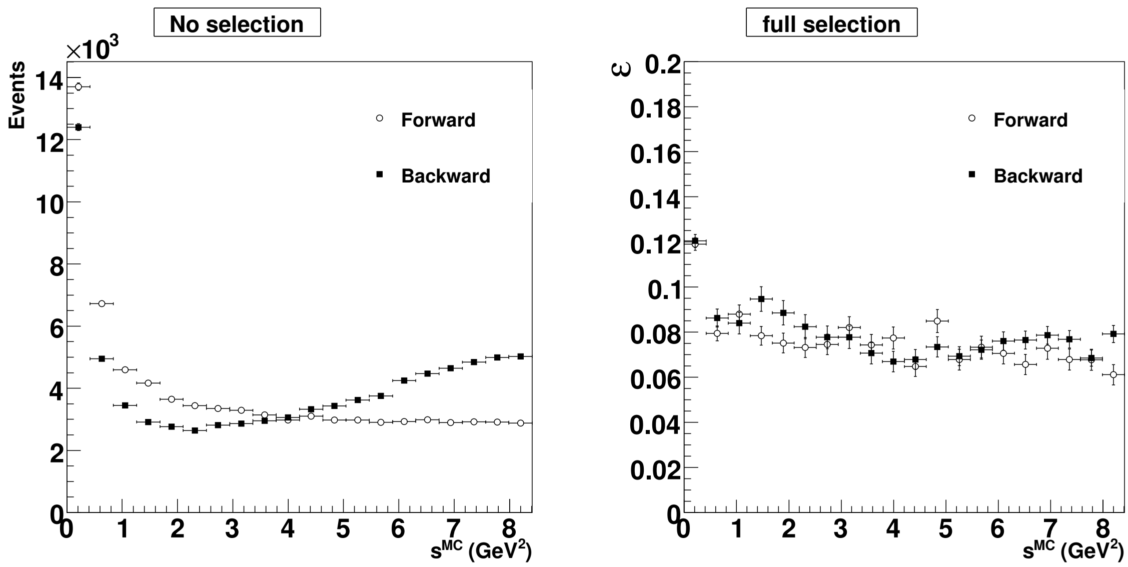

(a) (b)

Figure 6.3: *(a) Distributions of s of forward and backward Monte Carlo truth events in 4π (b) Selection efficiencies for forward and backward events*

6.2.2 Implications

The fraction of selected events is different for forward and backward directions as was shown in Fig. 6.1(e). A bias in the selection efficiency for events in a certain direction has implications for the derived forward-backward asymmetry and its zero-crossing point. To investigate whether a bias arises, the s-distributions for forward and backward events are displayed separately in Fig. 6.3(a).

The efficiencies for forward and backward events as a function of s are displayed in Fig. 6.3(b). In this representation no statistically significant difference is observed between the efficiencies of forward and backward events. This means that the forward-backward asymmetry as a function of s is not affected by the selection. In other words, despite a different total efficiency for forward and backward events, the efficiency as a function of s is equal.

To explain the effect seen in Fig. 6.1(e), it becomes clear from Fig. 6.3(a) that a smaller (absolute) number of forward events will be selected at low s, compared to the absolute number of selected backwards events. Similarly at large s, a smaller number of backward events are selected. Although the efficiencies for forward and backward events are equal, the dependence on s will cause a distorted apparent efficiency as a function of θ_l, after integration over s. Since these regions are not symmetric in the s range around the point where the forward and backward event numbers are equal, an apparent bias in the efficiency as a function of s has been introduced. This apparent bias for an integrated s-range can also shown as follows. The difference in the true number of forward events (N_F) and true number of backward events (N_B) is given by:

$$\Delta N^{\text{true}}(s) = N_F(s) - N_B(s), \tag{6.1}$$

which leads to an asymmetry of

$$A_{FB}^{\text{true}} = \frac{N_F(s) - N_B(s)}{N_F(s) - N_B(s)}. \tag{6.2}$$

The difference changes when selection efficiencies are introduced for forward (ϵ_F) and backward events (ϵ_B):

$$\Delta N^{sel}(s) = \epsilon_F(s)N_F(s) - \epsilon_B(s)N_B(s), \tag{6.3}$$

leading to

$$A_{FB}^{\text{sel}}(s) = \frac{\epsilon_F(s)N_F(s) - \epsilon_B(s)N_B(s)}{\epsilon_F(s)N_F(s) - \epsilon_B(s)N_B(s)}. \tag{6.4}$$

In general $A_{FB}^{\text{true}} \neq A_{FB}^{\text{sel}}(s)$ unless $\epsilon_F(s) = \epsilon_B(s)$. However even if $\epsilon_F(s) = \epsilon_B(s) = \epsilon$, one can still see a possible bias in the value integrated over s, since

$$\begin{aligned} A_{FB}^{\text{true,int}} &= \frac{N_F - N_B}{N_F + N_B} \\ &= \frac{\int \mathrm{d}s N_F(s) - \int \mathrm{d}s N_B(s)}{\int \mathrm{d}s N_F(s) + \int \mathrm{d}s N_B(s)} \\ &\neq \frac{\int \mathrm{d}s \epsilon(s) N_F(s) - \int \mathrm{d}s \epsilon(s) N_B(s)}{\int \mathrm{d}s \epsilon(s) N_F(s) + \int \mathrm{d}s \epsilon(s) N_B(s)} = A_{FB}^{\text{sel,int}} \end{aligned} \tag{6.5}$$

When the efficiency of the angle θ_l (displayed in Fig. 6.1(e)) is calculated separately for slices of the invariant mass s, the bias vanishes. In Fig. 6.4 the θ_l distributions for events are shown in nine slices of the invariant dimuon mass squared. Both the θ_l^{MC} distributions before any selection and after final event selection are displayed.

The efficiency for each of the nine slices in s is displayed in Fig. 6.5. The apparent efficiency difference between forward and backward events of Fig. 6.1(e) is no longer present after showing the efficiency in bins of s. Table 6.1 shows the values for A_{FB} before and after the selection for the different bins of the invariant dimuon mass squared, s. The last two columns list the efficiencies of forward and backward events separately. The integrated forward-backward asymmetry before and after the selection steps is also shown for a total s-range from 1.0 to 8.4 GeV^2.

It is clear that $A_{FB}(s)$ is not significantly altered per bin of s, whereas the integrated A_{FB} is. The implication of the equal efficiencies for forward and backward going muons is that the selection does not influence the forward-backward asymmetry as a function of s.

The forward-backward asymmetry is calculated for the four cases: events before any selection, after preselection, after full selection and after selection using reconstructed variable. The forward-backward asymmetries for these event samples are displayed in

s range (GeV^2)	A_{FB} before	A_{FB} after	ε_F	ε_B
$s < 1.0$	0.066 ± 0.009	0.067 ± 0.015	0.1047 ± 0.0023	0.1089 ± 0.0025
$1.0 < s < 2.0$	0.121 ± 0.016	0.090 ± 0.027	0.0785 ± 0.0030	0.0900 ± 0.0037
$2.0 < s < 3.0$	0.098 ± 0.017	0.081 ± 0.030	0.0756 ± 0.0032	0.0805 ± 0.0037
$3.0 < s < 4.0$	0.038 ± 0.017	0.083 ± 0.030	0.0800 ± 0.0034	0.0717 ± 0.0033
$4.0 < s < 5.0$	-0.010 ± 0.018	-0.025 ± 0.031	0.0718 ± 0.0033	0.0697 ± 0.0031
$5.0 < s < 6.0$	-0.102 ± 0.017	-0.117 ± 0.030	0.0716 ± 0.0033	0.0716 ± 0.0029
$6.0 < s < 7.0$	-0.204 ± 0.017	-0.249 ± 0.030	0.0704 ± 0.0033	0.0762 ± 0.0028
$7.0 < s < 8.0$	-0.279 ± 0.017	-0.293 ± 0.031	0.0679 ± 0.0032	0.0746 ± 0.0026
$8.0 < s < 9.0$	-0.298 ± 0.017	-0.362 ± 0.031	0.0644 ± 0.0031	0.0774 ± 0.0026
$1.0 < s < 9.0$	-0.029 ± 0.003	-0.229 ± 0.007	-	-

Table 6.1: *Values for A_{FB} before and after selection in the 9 invariant dimuon mass bins. The asymmetry for the integrated range A_{FB}^{int} is given in the last row. In the last two columns the angular efficiencies for forward and backward events are displayed.*

Fig. 6.6(a,b,c,d) respectively. As was already calculated in table 6.1 the shape of the asymmetry does not change significantly.

In the next section the selection of dimuon inclusive background events is investigated for systematic biases in the angular distributions.

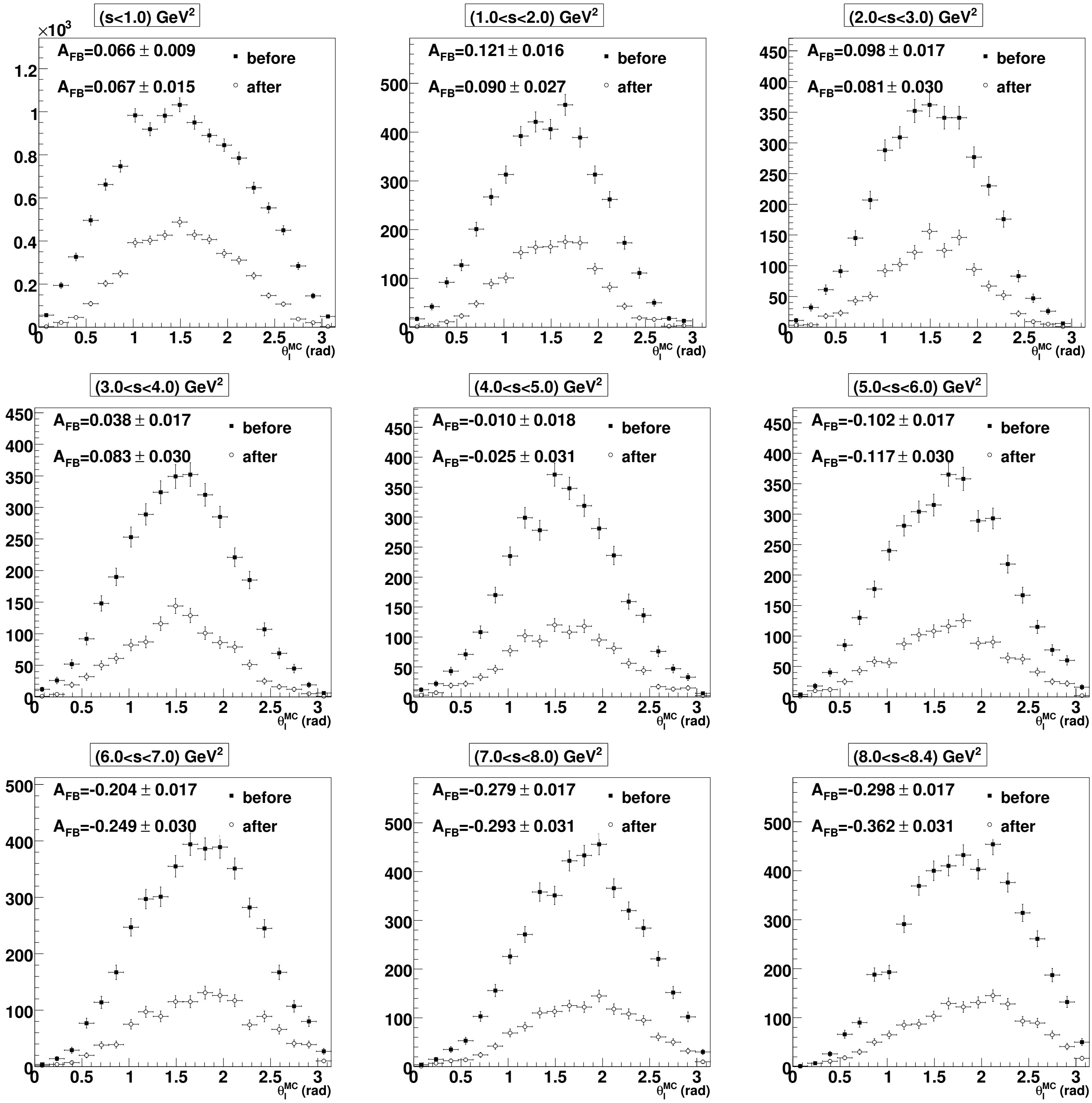

Figure 6.4: *Changes in the MC matched dimuon angle distribution before and after selection in 9 slices of the invariant dimuon mass s.*

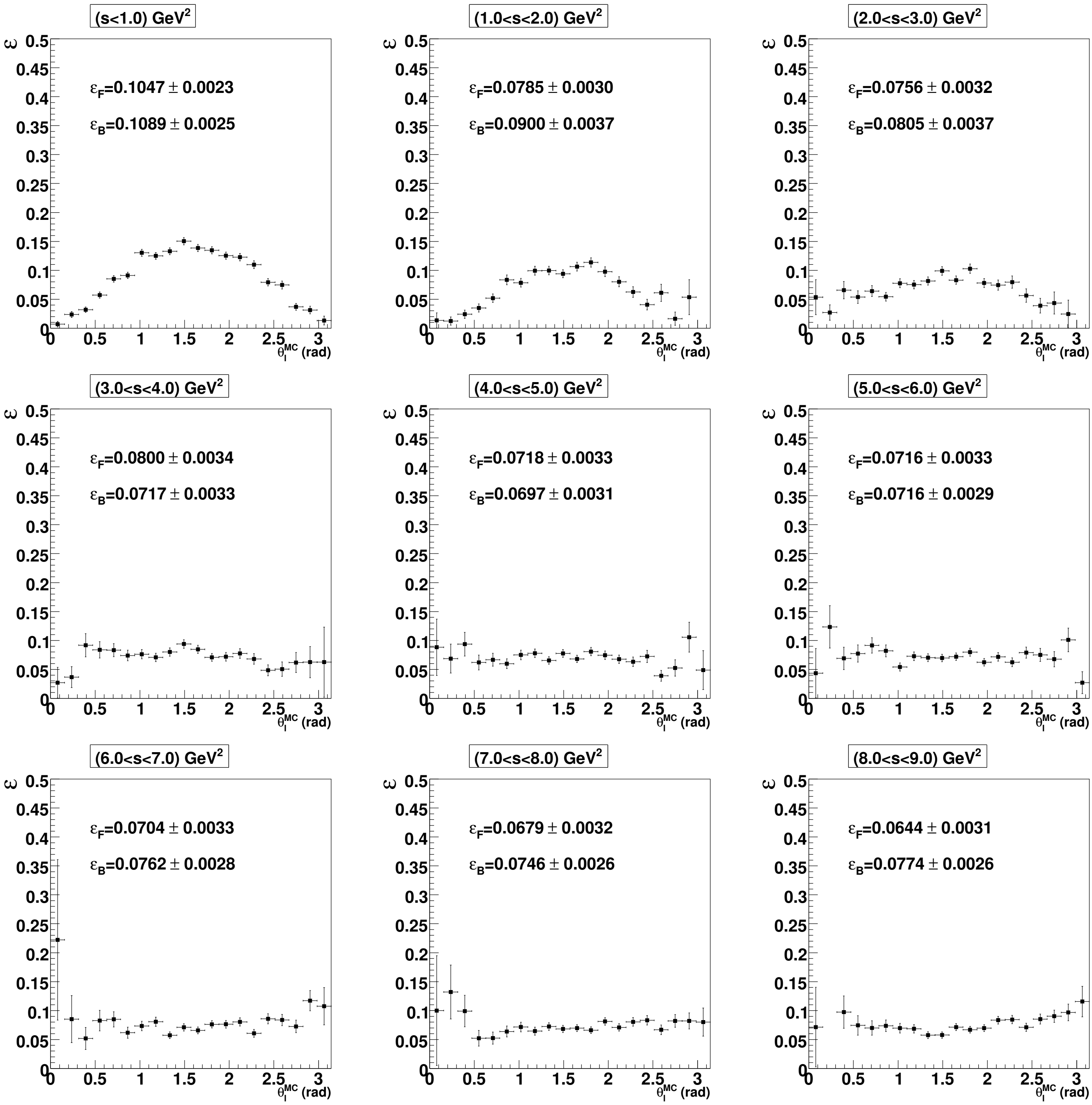

Figure 6.5: *Angular efficiency in nine equal slices of the invariant dimuon mass s.*

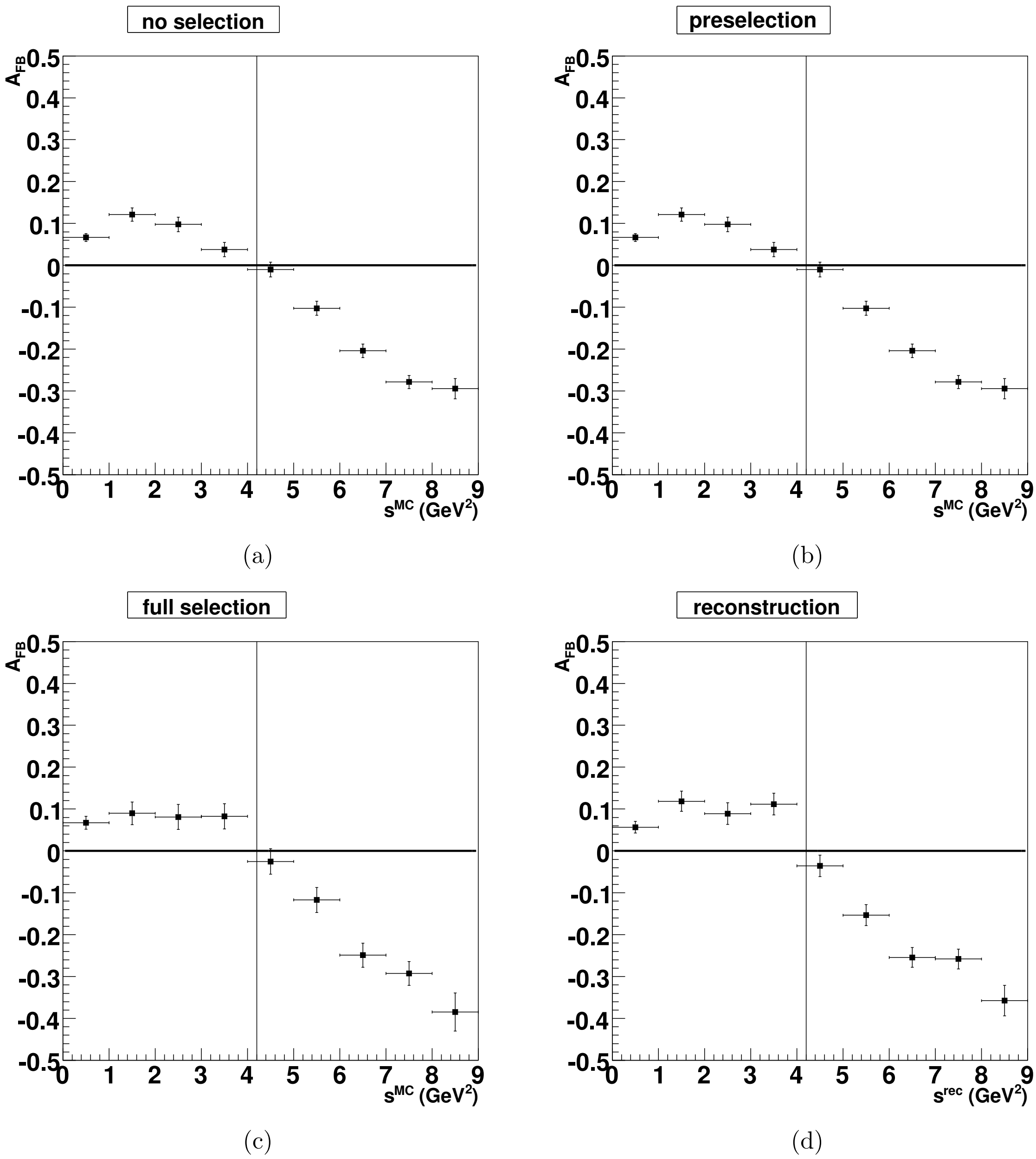

Figure 6.6: *Forward-backward asymmetries for the datasets of (a) MC truth events, (b) preselected events, (c) all selected events and (d) reconstructed events. The vertical line indicates the true value of the zero-crossing.*

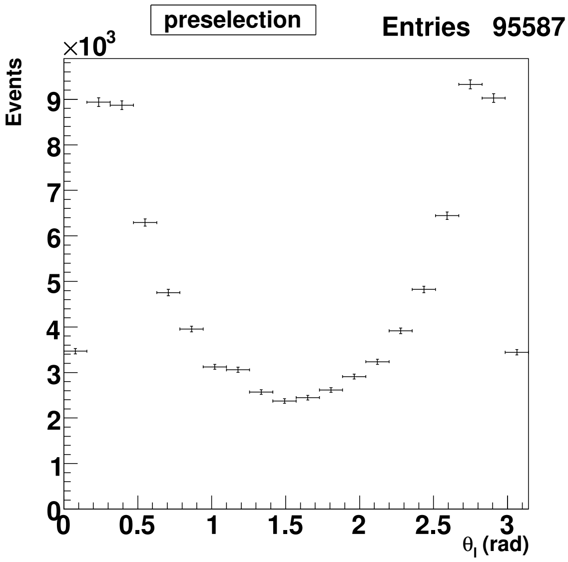

(a)

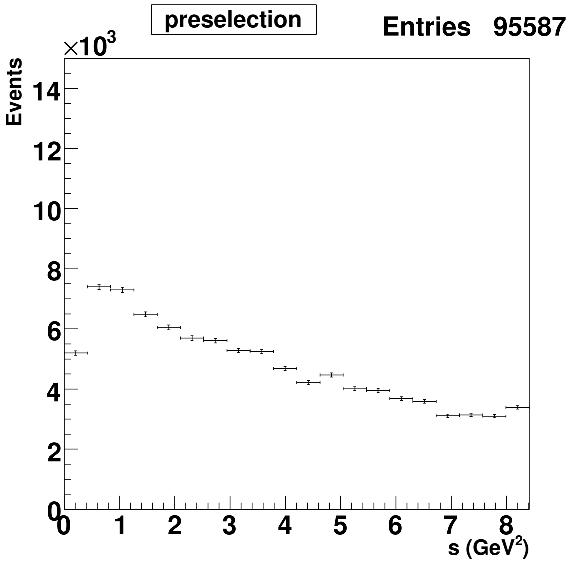

(b)

Figure 6.7: *(a) Distribution of θ_l and (b) s for the preselected background.*

6.2.3 Background event distributions

Distributions of the polar angle of the muon, θ_l, and the invariant dimuon mass, s, for the preselected background are given in Fig. 6.7. After the full selection is performed the number of available background events is reduced to 8, and hence the shapes of the background distributions cannot be determined. Therefore all background events that pass the preselection only are used, assuming that these comprise a representative sample for the background after full selection. The separate selection steps are applied on the background in the next section.

6.2.4 Effects of selection on the polar muon angle distributions in the background

The effects of the selection steps on θ_l distributions of the background events are shown in Figs. 6.8. Any artificially introduced asymmetry in the polar angle could lead to a shift in the zero-crossing point of the forward-backward asymmetry as it changes

$$A_{FB}(s) = \frac{N_F(s) - N_B(s)}{N_F(s) + N_B(s)}, \tag{6.6}$$

with

$$N_F(s) \to N_F(s) + M_F(s) \tag{6.7}$$

and

$$N_B(s) \to N_B(s) + M_B(s), \tag{6.8}$$

where N is the number of signal events and M is the number of background events. The labels F and B denote events with a forward muon and events with a backward muon. Due to the addition of the extra number of events the asymmetry will be reduced. However, as long as the number of selected forward and backward background events are the same at each value of the invariant dimuon mass ($M_F(s) = M_B(s)$), the value of the zero crossing point, s_0, where the forward and backward events are equal, will not change. Therefore it is important to check the symmetry of the θ_l distributions after the selection.

The θ_l distributions after separate selection steps are shown in Fig. 6.8; K^* selection rules applied in Fig. 6.8(a), the B^0 selection rules applied in Fig. 6.8(b), the K selection rules applied in Fig. 6.8(c), the π selection rules applied in Fig. 6.8(d), the $\mu\mu$ selection rules applied in Fig. 6.8(e) and finally the final selection applied in Fig. 6.8(f). From all the selection criteria the selection on the muon variables changes the distributions most, as is shown in Fig 6.8(e). However, the selection has no influence on the difference between the total number of forward and backward events. This is visible in the distributions of the dimuon invariant mass in Figs. 6.9(a-f), where the same selections are applied as in Figs 6.8(a-f). The conclusion can be drawn that the selection will not bias the background events in a false zero-crossing of the forward-backward asymmetry.

The forward-backward asymmetry will be flattened by the inclusion of events which do not have an angular preference. The precise effects of the background will be given in chapter 7.

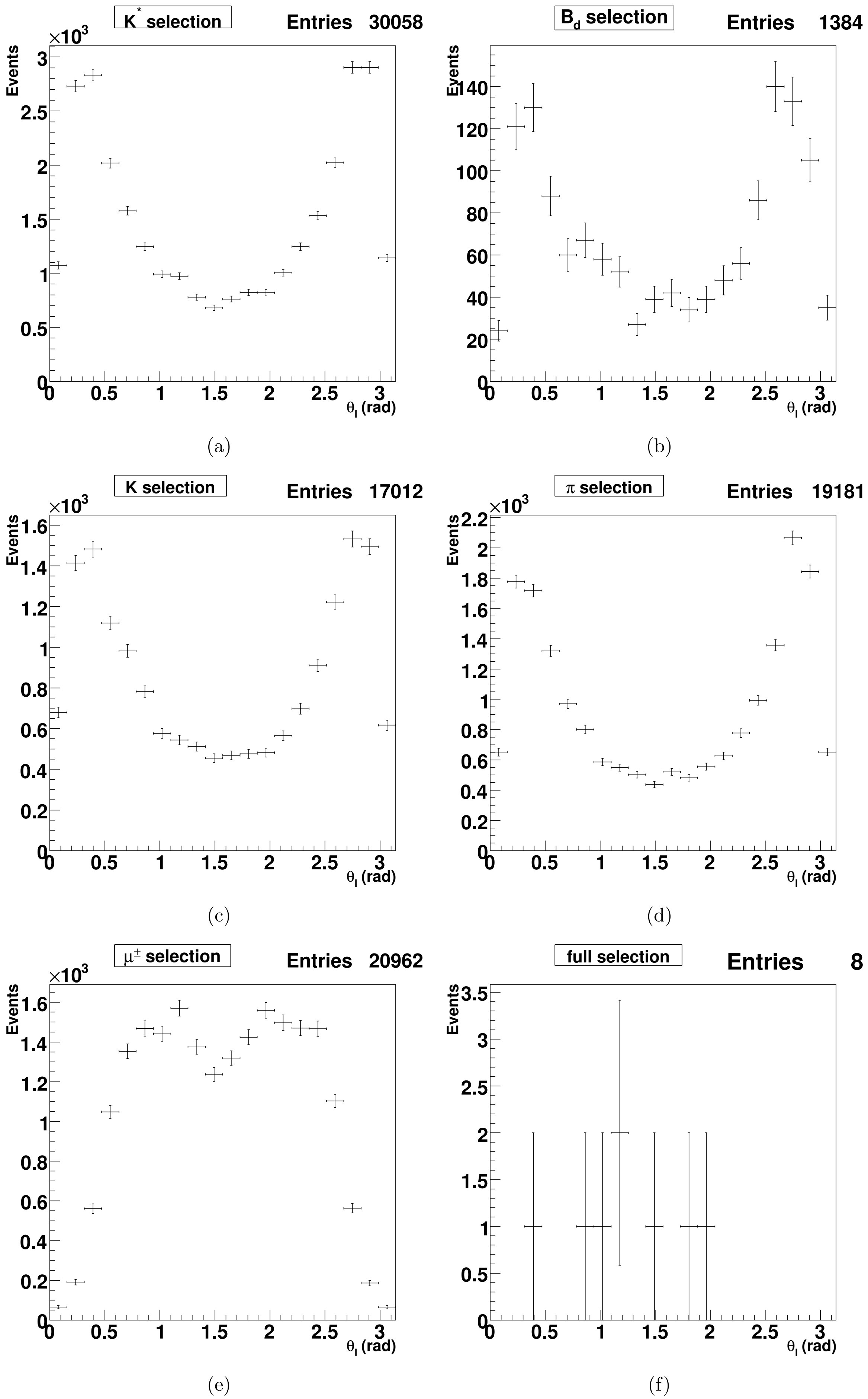

Figure 6.8: *Selection and reconstruction effects on θ_l distributions for background.*

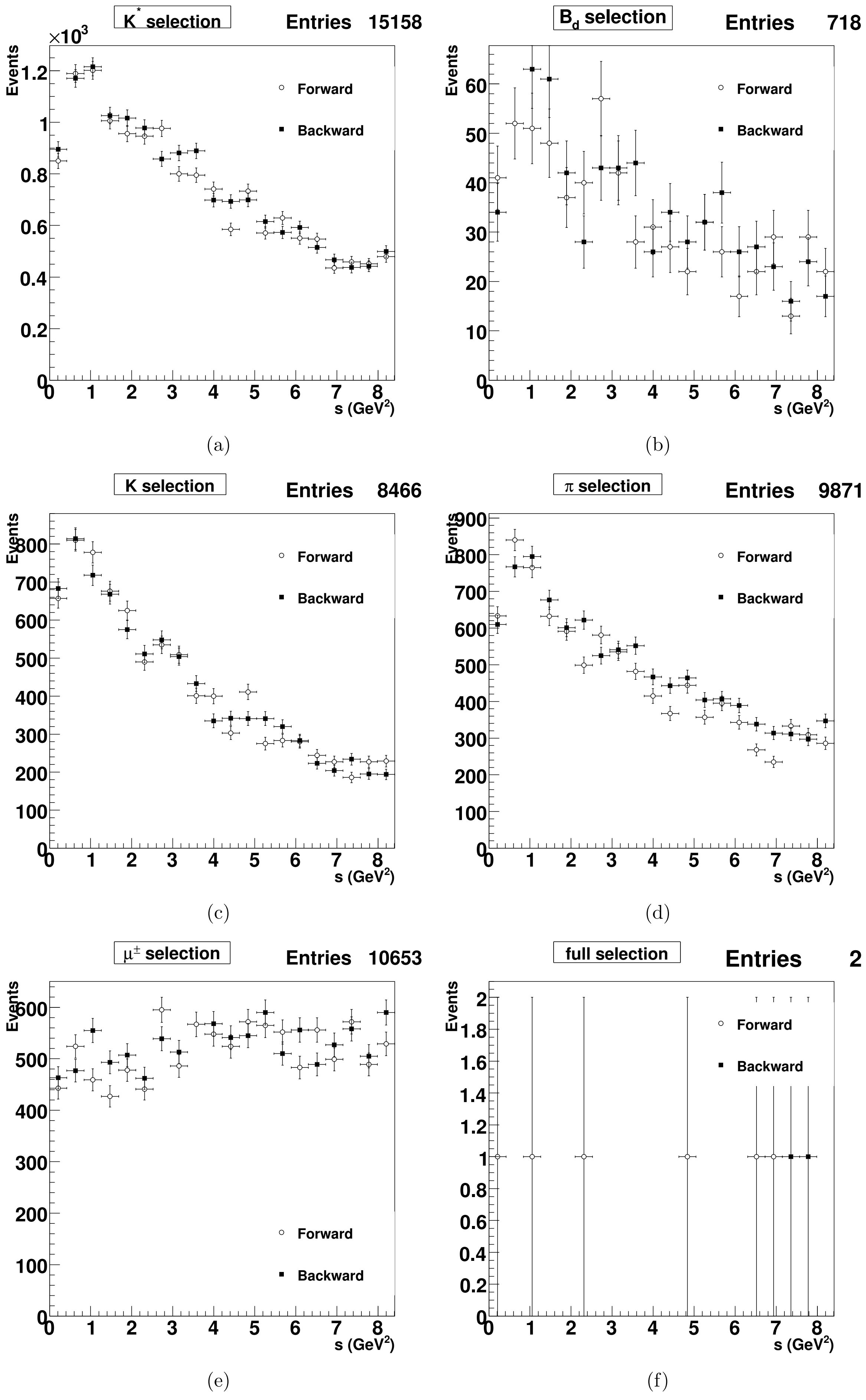

Figure 6.9: *Selection effects on s distributions for forward and backward going muons in the background. Forward and backward events have equal numbers in each bin of s.*

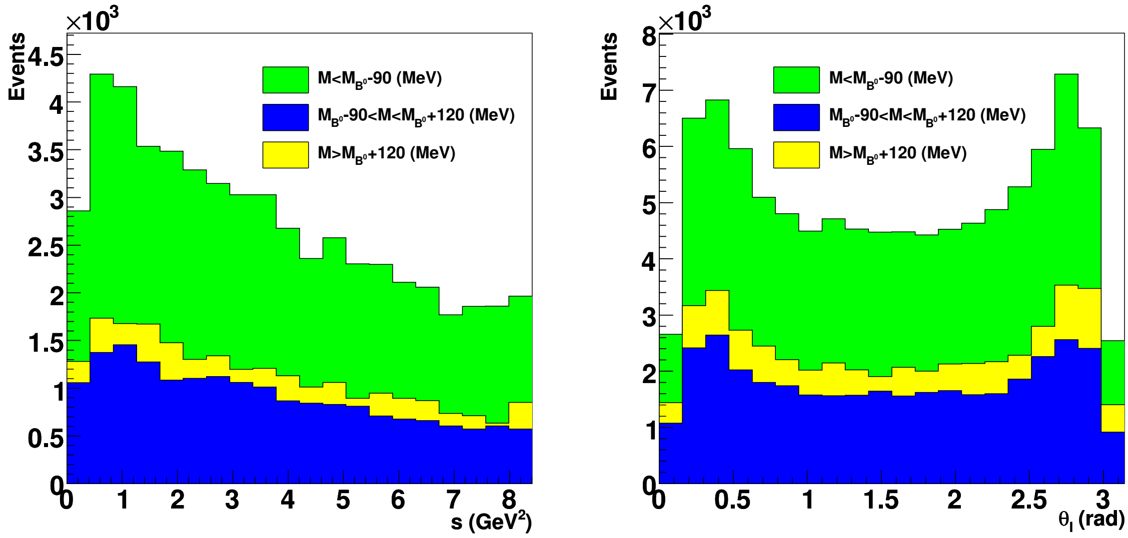

(a) (b)

Figure 6.10: *(a) Shape of s distributions of the dimuon inclusive background at the sidebands and peak region in the invariant mass spectrum of the* B^0 *meson. (b) The shape of the* θ_l *distributions for the same three regions.*

6.2.5 Background Correlations

The background in the decay channel $B^0 \to K^{0*}\mu^+\mu^-$ in a region around the B^0 resonance can be estimated from the sidebands of the invariant mass spectrum of the B^0 mass peak. To be able to use the events in the mass sidebands the distribution of the invariant B^0 mass must be smooth in the analysing variables, *i.e.* the invariant dimuon mass and the polar muon angle, θ_l. The peak region is chosen in the range from $M_{B^0} - 90$ (MeV) to $M_{B^0} + 120$ (MeV).

The shapes of the invariant mass s, and angle θ_l, are shown in Fig. 6.10 for the sideband regions and the peak region. Fig. 6.10(a) depicts the invariant dimuon mass dependence for three regions in the B^0 mass spectrum. The s-distribution shows a similar shape in all three mass regions.

Similarly, Fig. 6.10(b) shows the distribution of the angle θ_l. The background is symmetric in θ_l, yielding a zero forward-backward asymmetry. The dependence of θ_l is smooth with respect to the B^0 invariant mass. Since both s and θ_l are smooth an interpolation from the sideband into the peak region seems feasible. The precise method of separating the background from the signal in the peak region will be described in the next chapter.

6.3 Conclusions

Potential systematic effects from the event selection on the forward-backward asymmetry and its zero-crossing have been investigated. The combined restrictions on the muons will have the largest influence on the shapes of the invariant dimuon mass s and the muon polar angle θ_l. However, the zero-crossing will not be affected.

An apparent bias in the efficiency of the polar angle is explained due to an integration over the invariant mass. When the efficiency is calculated in slices of s, the efficiency for forward and backward events is equal, and the bias vanishes.

The selection effects for the background show that there is no preference for events with either forward or backward going muons. The addition of background events does not affect the zero-crossing of the forward-backward asymmetry.

The distributions of the invariant dimuon mass, s for the dimuon inclusive background shows a similar shape in the sideband regions and the peak region of the B^0 mass distribution. The shape of the distribution in the B^0 mass sidebands can therefore be used to estimate the shape and number of the background events in the peak region. The same holds for the distribution of the polar angle θ_l. This is exploited when the background fraction in the peak region is determined by interpolation.

7

Sensitivity studies of A_{FB} in $B^0 \to K^{*0}\mu^+\mu^-$

7.1 Introduction

In the decay $B^0 \to K^{*0}\mu^+\mu^-$ the angular distribution of the muons depends on the dimuon invariant mass. In the rest frame of the B-meson the angle θ_l of the negative muon with respect to the dimuon helicity axis in the dimuon rest frame determines whether it is an event with a forward going ($|\theta_l| < \pi/2$) or backward going ($|\theta_l| > \pi/2$) muon. (See Fig. 1.4 for an illustration.)

The number of events with a forward going muon (N_F) depends on the dimuon invariant mass squared (s) and is generally not the same as the number of events with a backward going muon (N_B). In the standard model the forward-backward asymmetry defined as $A_{FB}(s) = (N_F(s) - N_B(s))/(N_F(s) + N_B(s))$ is conservatively estimated to vanish at $s_0 = 4.2 \pm 0.6$ GeV^2 [33]. In this chapter a comparison is made between two different methods to fit the observed A_{FB} in order to determine its zero-crossing point s_0 (ZCP).

The first method implements a straight line fit of the asymmetry $A_{FB}(s)$, which is binned as a function of the dimuon invariant mass squared, s. The second method determines the A_{FB} using an unbinned polynomial fit to the distribution of invariant dimuon masses squared for events with a forward and backward muon separately.

The determination of the zero crossing of A_{FB} with the binned straight line method will be described in section 7.2. In section 7.3, the unbinned method will be presented, the stability of the fitting method will be discussed and expectation values for three different physics models discussed in chapter 1 will be shown. The determination of the error on the zero-crossing point for a single experiment will be discussed in section 7.4.

In the section 7.5 a method is described to subtract background in the unbinned fitting approach. Finally in section 7.6, the sensitivity potential of LHCb is examined using the unbinned method to distinguish new physics manifestations of Wilson coefficient $C_{7\gamma}$ with a reverse sign with respect to the standard model.

7.1.1 Monte Carlo samples

The MC data used in the analyses is produced by the LHCb event generator[1] based on the Pythia program together with the event generator EvtGen. Three physics models described in section 1.7 were simulated to test the fitting methods; a model with SM parameters, SUSY1 parameters and SUGRA1 parameters. The total sizes of the available event samples are listed in Table 7.1. These events are used to simulate many experiments, each with an integrated luminosity of 2 fb^{-1}, the equivalent of one year nominal LHCb operation.

The background sample used in the studies in Section 7.5 consists of dimuon inclusive Monte Carlo events. The sample of 2.6 10^7 Monte Carlo background events corresponds to an integrated luminosity of 5.2 pb^{-1}. This is a relatively small sample corresponding to a nominal running time of a few hours. In order to emulate a larger equivalent sample only the preselection criteria are applied, giving an equivalent of 0.43 ab^{-1} of integrated luminosity.

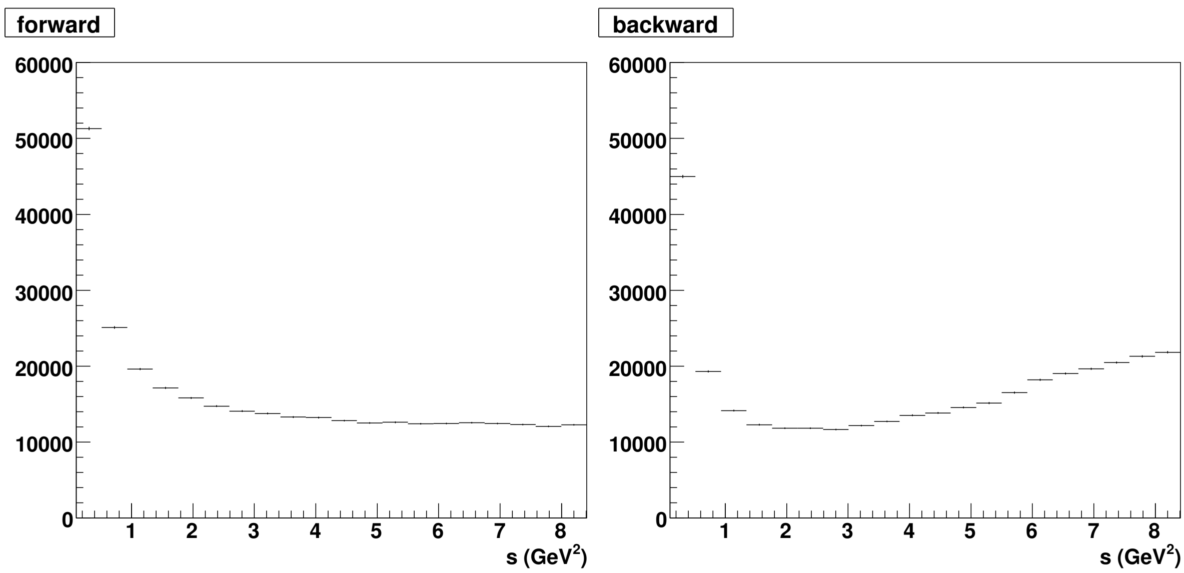

Figure 7.1: *Distribution of s for forward and backward going muons respectively from the LHCb Monte Carlo events with standard model parameters. The sample size is equivalent to an integrated luminosity of 424 fb^{-1}.*

Model	s_0 (GeV^2)	Size (Events)	$\int \mathcal{L}$
SM	3.93 ± 0.04	1529951	0.424 ab^{-1}
SUSY1	3.51 ± 0.09	1425017	0.396 ab^{-1}
SUGRA1	4.66 ± 0.02	1520020	0.422 ab^{-1}
$\mu\mu$ incl. BG	-	2.6 10^7	5.2 pb^{-1}

Table 7.1: *Estimated true values for the zero crossing value, s_0, for various models stated in the second column. The total data sample sizes, used to estimate the true value are shown in the third column, and in the fourth column the corresponding integrated luminosity is given.*

7.1.2 Invariant dimuon mass distributions from MC events

The distributions of the dimuon invariant mass from the LHCb event generator for events with a forward and backward going muon are shown in Fig. 7.1. A large amount of statistics is used to illustrate the difference in shape of the distributions. It can be seen that the number of backward events rises at high s whereas the number of forward events continues to fall with s. The value of s for which the amount of forward and backward events is identical, the zero crossing point of the asymmetry, is determined in the procedure that is described next.

7.1.3 Estimation of the input value of the zero crossing

To evaluate the accuracy of the fit methods the input value of the zero crossing must be known for the different models. An estimation of this value is made with a very high statistics Monte Carlo sample where a zoom is made within the range where the asymmetry changes from positive to negative, as shown in Fig. 7.2. In this small area a straight line fit is made to determine the true zero crossing point. The statistical uncertainty on the true zero crossing point quoted in Table 7.1 is obtained from the straight line fit [2].

[1] GAUSS v12r3.

[2] When the zero crossing point is determined with different binnings or ranges, the observed variations are compatible with the statistical uncertainty.

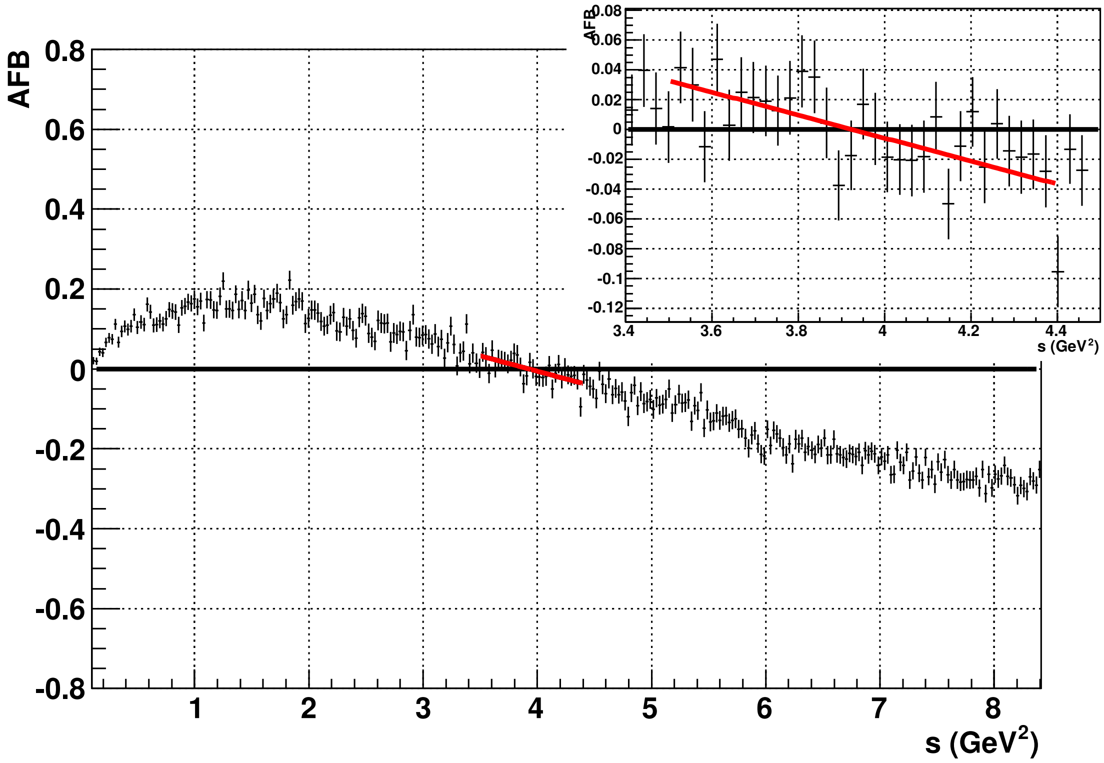

Figure 7.2: *Example of the input value estimation of the zero crossing using an equivalent integrated luminosity of 0.424 ab^{-1} of events. The model depicted has SM parameters.*

7.2 Determination of A_{FB} and s_0 with a binned fit

In the binned approach the $A_{FB}(s)$ is calculated by determining the amount of forward and backward going muons in separate bins of s. The asymmetry per bin is subsequently calculated and the resulting points are fitted using a straight line fit in an appropriate region to determine the ZCP. As can be seen in Fig. 7.2 the assumption of linearity means that the fit range should be restricted.

The binned fitting method is tested for three of the physics models introduced in section 1.7: the Standard Model, the SUGRA1 model and the SUSY1 model.

When the ZCP is determined from a straight line fit, it is indeed found that the choice of the fit range can affect the determination of the zero crossing of the asymmetry. Especially in cases where the A_{FB} is nonlinear around its vanishing point, the estimate can be biased. An example asymmetry obtained from 2 fb^{-1} event sample generated with SM parameters, is fitted over two different bin sizes but over the same ranges in Fig. 7.3 and Fig. 7.4. In both examples the same data is fit over two identical ranges.

Although the binsize does not affect the zero-crossing point, the fit range is subject to some arbitrariness and since the exact shape of the forward-backward asymmetry is not known, even in the standard model case, a linear fit might not be sufficient. Furthermore, a direct linear fit of the A_{FB} could be biased by the choice in fit range.

To investigate whether there can be a systematic bias in a straight line fit, MC experiments each of a size of 2 fb^{-1} have been performed for the available amount of events. As an illustration for each experiment the zero crossing point has been determined in a straight line fit using 12 bins over a range[3] from 2.87 to 4.25 GeV^2. The distribution of zero-crossing points reflects the statistical error of the fit, while the shift from the true value is a measure for a systematic bias. In Fig. 7.5 the resulting distribution is shown. A small bias of the fitted value is observed of 0.27 ± 0.4 GeV^2 compared to the determined true value.

This procedure to determine the mean and uncertainty of the zero crossing value has been performed for several different fit ranges and bin sizes. Fig. 7.6 shows the mean values and errors on the means for different bin sizes and different ranges superimposed on the estimated true value of the LHCb Monte Carlo with SM parameters. A bias of each fit has been calculated as the true value minus the obtained value. In Table 7.2 the biases are reproduced. Biases in the determination of s_0 are observed to range from -0.09 GeV2 to 0.27 GeV^2.

The results for the measurements of ZCP for different physics models are shown in Figs 7.7 and 7.8. The biases for these models are also reproduced in Table 7.2.

When the A_{FB} is not linear in the region of the zero crossing the estimate of the zero crossing may yield a wrong result. This is noticeable when comparing the results of the zero cross fit for the different models. It is observed that for events generated according to the SUSY1 parameters a systematically high zero crossing points is found, whereas for the data generated according to SUGRA1 parameters a systematically low zero crossing point is obtained. To eliminate the choice of binning and a particular choice of range an unbinned method will be presented next.

[3]The range is choosen over an integer number of bins starting from $s = 0.1$ GeV^2.

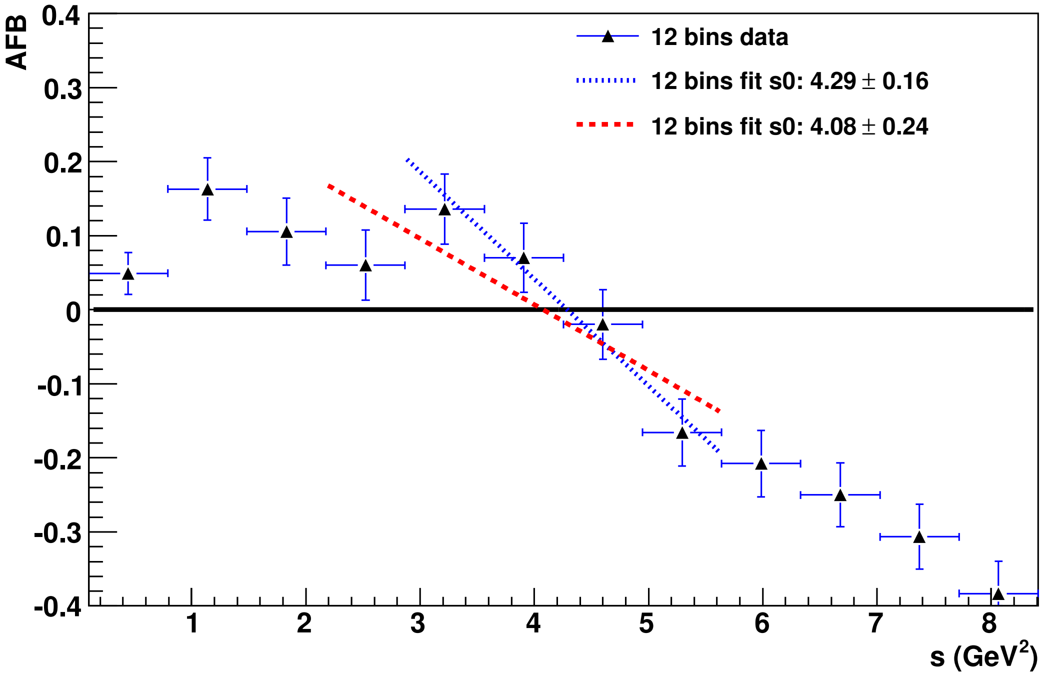

Figure 7.3: *Binned fit of a MC sample with SM parameters for a fit using 12 bins. The sample size corresponds to 2 fb^{-1}. Taking one more bin in the fit range changes the result of the zero crossing.*

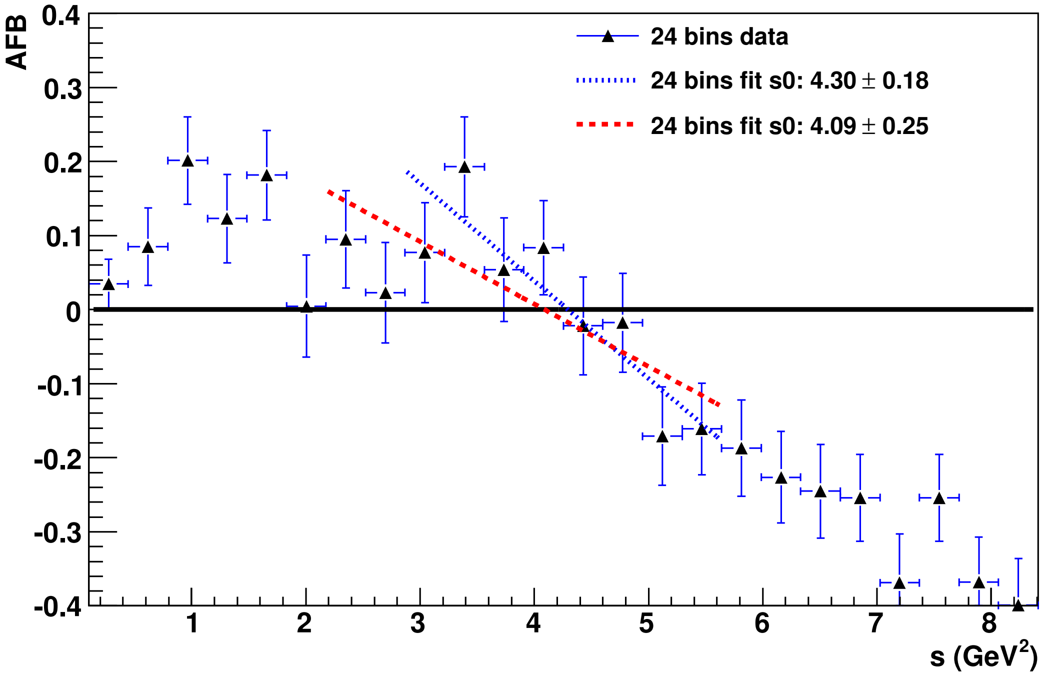

Figure 7.4: *Binned fit of a MC sample with SM parameters for a fit using 20 bins. The sample size corresponds to 2 fb^{-1}. Taking two more bin in the fit range changes the result of the zero crossing.*

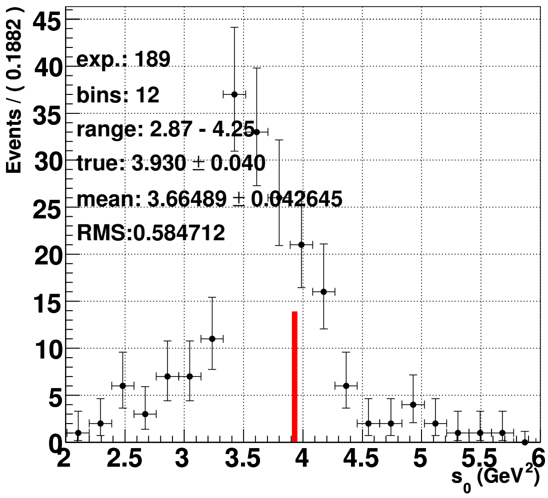

Figure 7.5: *Distribution of the fitted zero crossing point for the model with SM parameters. It shows a bias in binned line fits for 12 bins in a fit range from 2.87 to 4.25 GeV^2. The true value is shown by the vertical line. Each zero-crossing point was determined with an equivalent sample size of 2 fb^{-1}. A total of 212 zero crossing points were fit, however only a number of 189 fits actually yielded a number in the reasonable range from 2 to 6 GeV^2.*

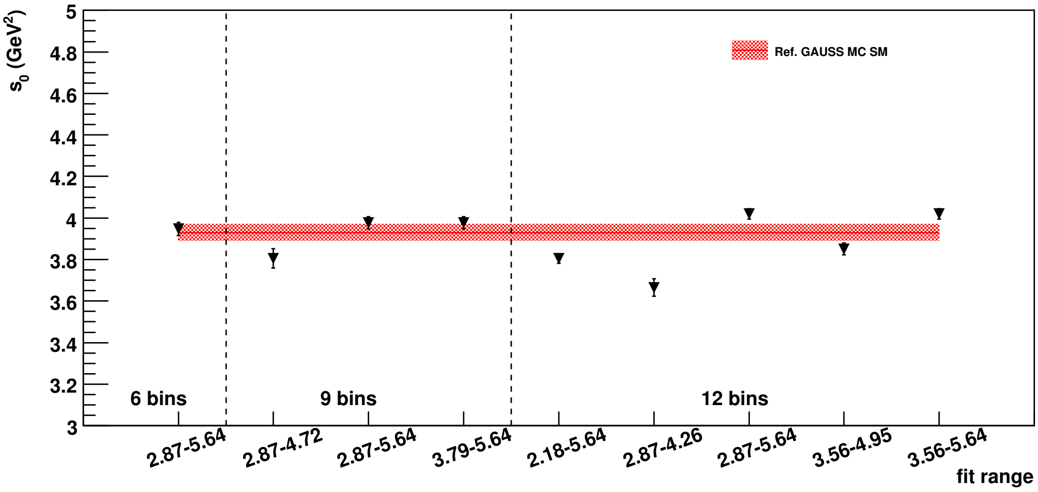

Figure 7.6: *Mean values for the fit of the zero crossing for different binnings and different ranges of a model with SM parameters. The sample size that is used is equivalent to 2 fb^{-1}.*

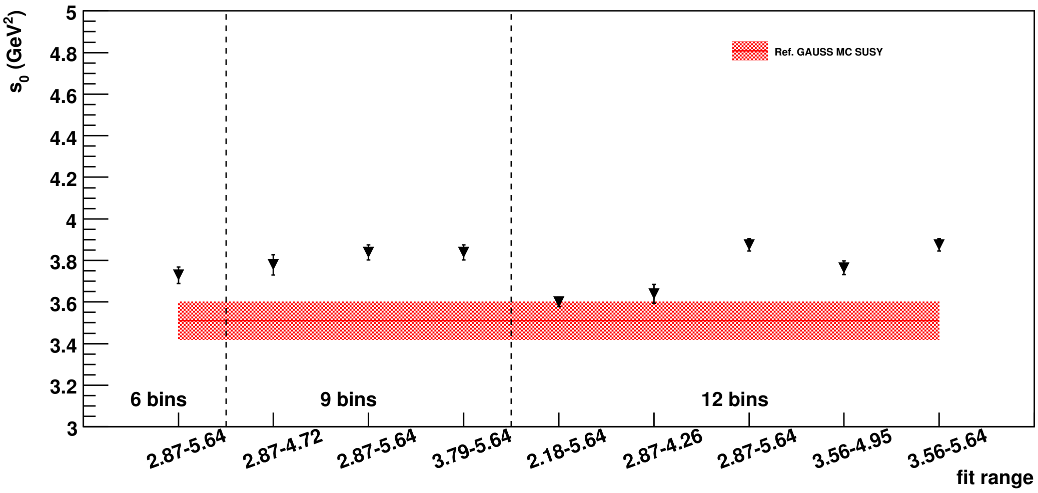

Figure 7.7: *Mean values for the fit of the zero crossing for different binnings and different ranges of a model with SUSY1 parameters. The sample size that is used is equivalent to 2 fb^{-1}.*

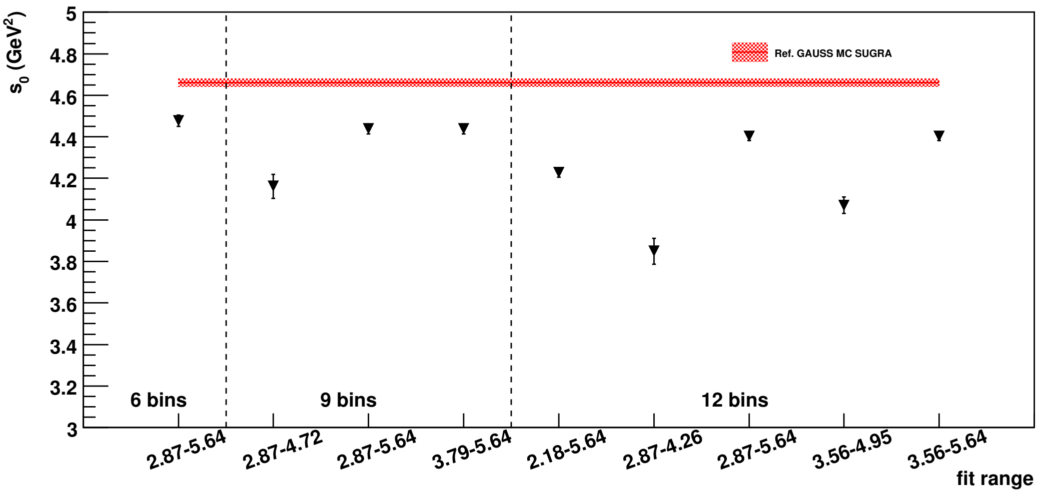

Figure 7.8: *Mean values for the fit of the zero crossing for different binnings and different ranges of a model with SUGRA1 parameters. The sample size that is used is equivalent to 2 fb^{-1}.*

start (GeV^2)	end (GeV^2)	bias SM (GeV^2)	bias SUSY1 (GeV^2)	bias SUGRA1 (GeV^2)
6 bins				
2.87	5.64	-0.02 ± 0.03	-0.22 ± 0.04	0.18 ± 0.03
9 bins				
2.87	4.72	0.12 ± 0.05	-0.27 ± 0.05	0.50 ± 0.06
2.87	5.64	-0.05 ± 0.03	-0.33 ± 0.04	0.22 ± 0.02
3.79	5.64	-0.05 ± 0.03	-0.33 ± 0.04	0.22 ± 0.02
12 bins				
2.18	5.64	0.13 ± 0.02	-0.09 ± 0.02	0.43 ± 0.02
2.87	4.26	0.27 ± 0.04	-0.13 ± 0.05	0.81 ± 0.06
2.87	5.64	-0.09 ± 0.02	-0.36 ± 0.03	0.26 ± 0.02
3.56	4.95	0.08 ± 0.03	-0.25 ± 0.03	0.59 ± 0.04
3.56	5.64	-0.09 ± 0.02	-0.36 ± 0.03	0.26 ± 0.02

Table 7.2: *Bias values and errors on the bias in the zero crossing using events from the LHCb event generator. The fit range is indicated by the begin value in the first column and the end value in the second column. The next columns indicate the difference of the truth value and the mean value of the Gaussian and its error for three different physics models.*

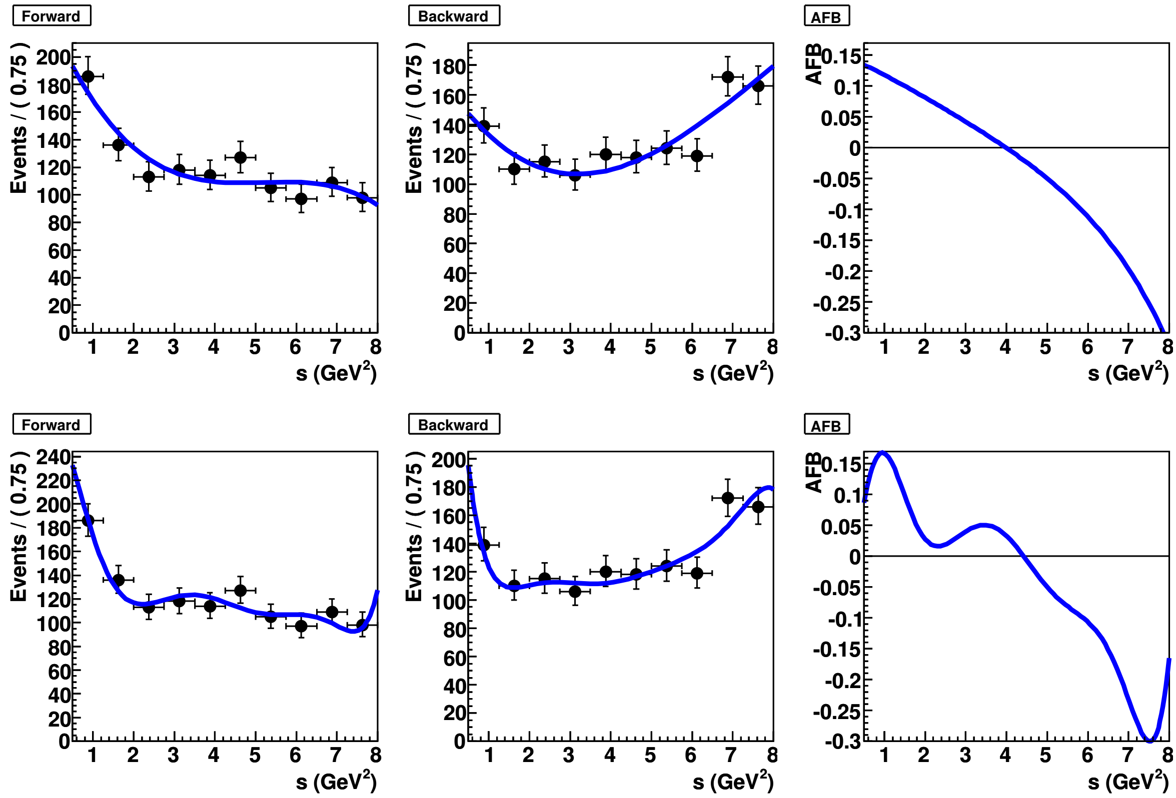

Figure 7.9: *Top: Unbinned fit with a 3rd order polynomial. Bottom: Unbinned fit with a 7th order polynomial. The fit is performed on the LHCb event generator events with a data size of 2 fb^{-1}.*

7.3 Unbinned likelihood fit

In this section an alternative determination of A_{FB} is discussed. Instead of first subtracting the forward and backward distributions in bins of s, the distributions of invariant mass of events with forward going and backward going muons are fitted separately with an unbinned polynomial likelihood fit. The fitted functions are then subtracted and subsequently normalised to obtain the A_{FB}. The RooFit library [79] was used to perform the likelihood fits. The fit utilises an n^{th}-order polynomial function. The order of the polynomial was chosen as low as possible not to be affected by statistical fluctuations but high enough to describe the full shape in a wide range of the muon invariant mass distributions.

In Fig. 7.9 representations of the unbinned method are given for two different fits using a 3^{rd}-order and 7^{th}-order polynomial respectively. The higher order polynomial will follow more rapid variations in the data. A third order polynomial was found to be sufficient. Both the forward and the backward distributions are fitted with an equal order polynomial.

The likelihood is described by implementing Chebyshev polynomials of the first kind

start (GeV^2)	end (GeV^2)	bias SM (GeV^2)	bias SUSY1 (GeV^2)	bias SUGRA1 (GeV^2)
unbinned				
0.10	8.41	0.02 ± 0.03	-0.13 ± 0.04	0.03 ± 0.02
0.79	8.41	-0.02 ± 0.03	-0.14 ± 0.05	0.14 ± 0.03
1.48	8.41	-0.02 ± 0.03	-0.15 ± 0.06	0.12 ± 0.03

Table 7.3: *Bias values and errors on the bias in the zero crossing using events from the LHCb event generator. The fit range is indicated by the begin value in the first column and the end value in the second column. The next columns indicate the difference of the truth value and the mean value of the Gaussian and its error for three different physics models.*

as probability density functions (PDFs). Chebyshev polynomials have properties that are desirable as they are orthogonal and have less correlation between parameters of different orders compared to ordinary polynomials. The coefficients for the forward and backward polynomials are denoted as α_i and β_i. To ensure proper relative normalisation the polynomial for the forward events is normalised to the number of events with a forward going muon, n_f, and the polynomial for the backward events is normalised to the number of events with a backward going muon, n_b. This leads to an asymmetry which is normalised as

$$A_{FB}(s) = \frac{n_f F(s;\alpha_i) - n_b B(s;\beta_i)}{n_f F(s;\alpha_i) + n_b B(s;\beta_i)}, \tag{7.1}$$

where F and B represent the forward and backward PDFs respectively.

7.3.1 Expectation value for s_0 and A_{FB} with the LHCb event generator

Using the LHCb event generator data, estimates are made for the measurement of the forward-backward asymmetry that LHCb is able to make after 1 year. The resulting A_{FB} distribution of 212 independent experiments is represented in Fig. 7.10 by the 1σ and 2σ bands. The statistical spread in the zero-crossing point is shown in Fig. 7.11.

The bias of the mean of the zero-crossing point distribution derived in the 212 experiments and the error on the mean are displayed for a number of fit ranges in Fig. 7.12 and Table 7.3.

Because the method does not rely on the linearity of the asymmetry in a certain s-range, the fit range can be enlarged almost arbitrarily.

For the SUSY1 and SUGRA1 models the zero-crossing points are also fitted with the unbinned method. The results are included in Table 7.3 and in Figs. 7.13 and 7.14 for the SUSY and SUGRA models respectively.

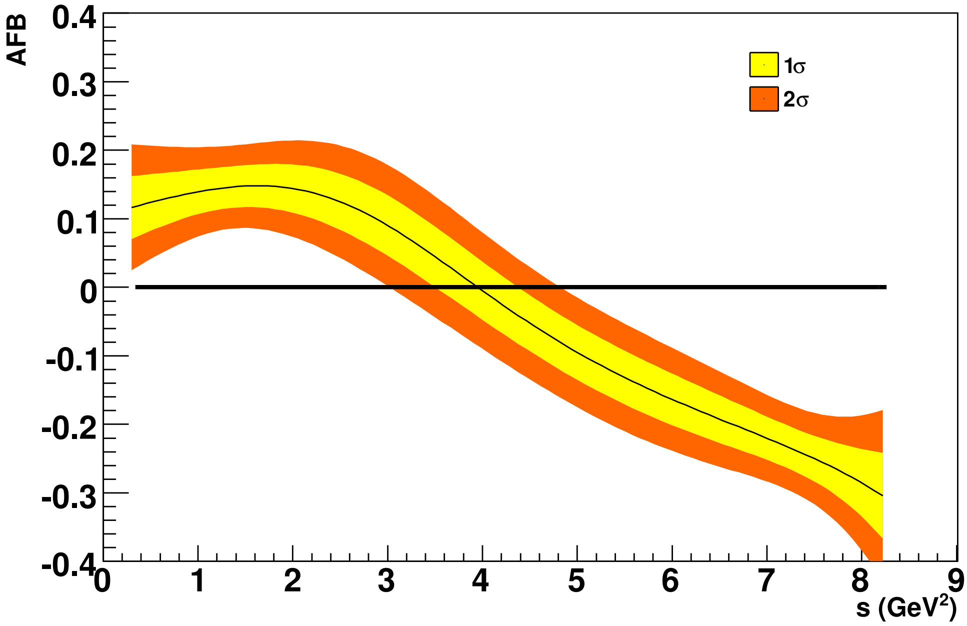

Figure 7.10: *Expectation value for 2 fb^{-1} (1 year) of MC, estimated with 212 experiments of 1 year.*

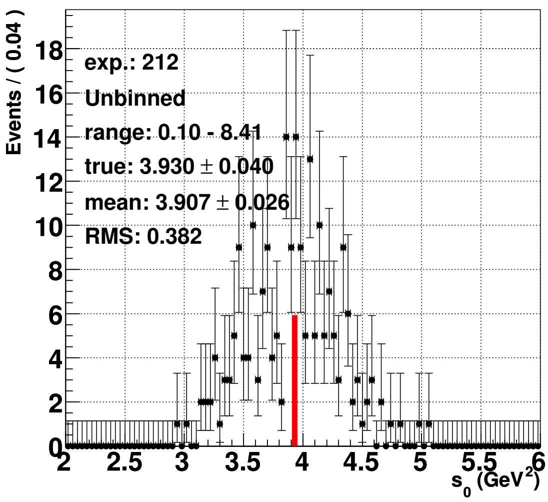

Figure 7.11: *Distribution of the zero crossing values with 212 times a 2 fb^{-1} (1 year) experiment. The vertical line indicates the estimated true value of the zero crossing.*

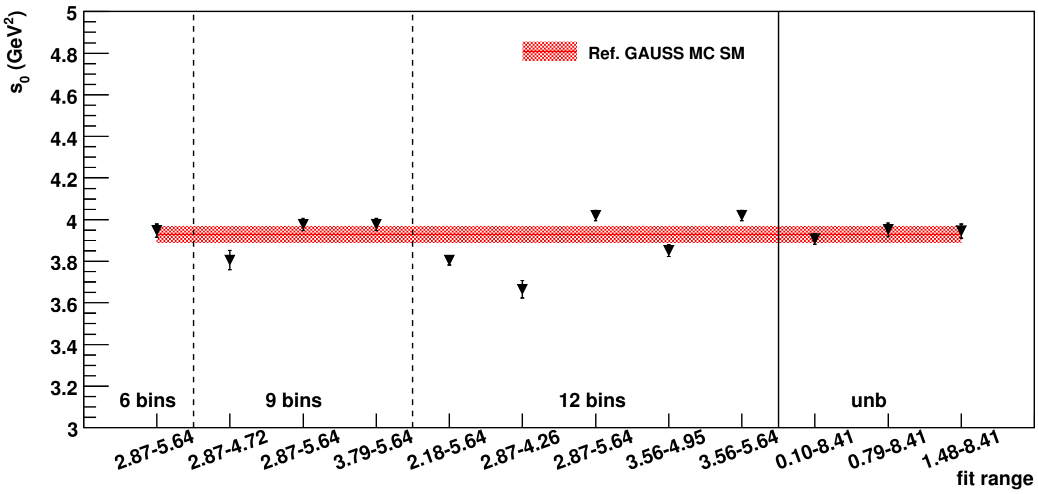

Figure 7.12: *The mean values for the zero crossing and the errors obtained by the binned fit for a different number of bins and the unbinned fit (labelled "unb") for different ranges and number of bins. The events are produced with SM parameters. The fits were performed on 212 experiments each with a sample size of 2 fb*$^{-1}$ *(1 year).*

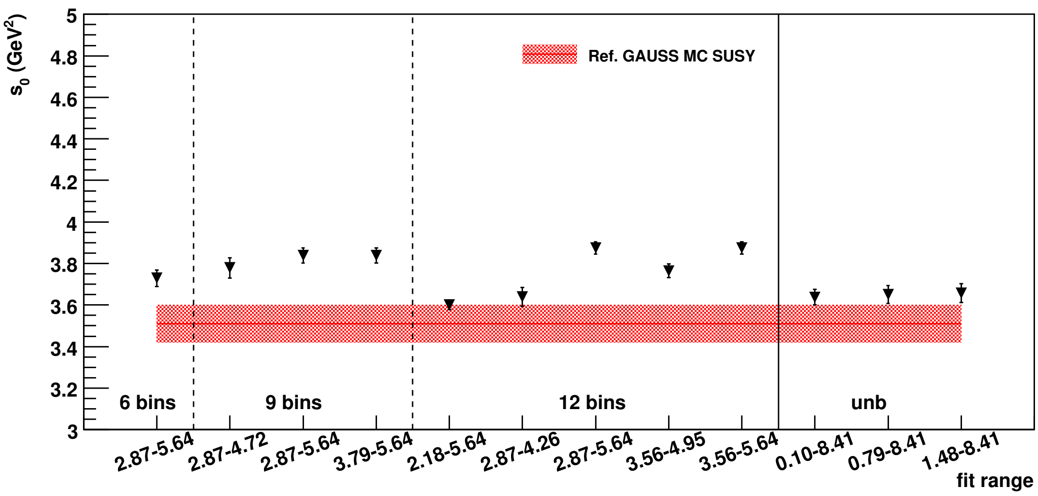

Figure 7.13: *The mean values for the zero crossing and the errors obtained by the binned fit for a different number of bins and the unbinned fit (labelled "unb") for different ranges and number of bins. The events are produced with SUSY1 parameters. The fits were performed on 197 experiments each with a sample size of 2 fb*$^{-1}$ *(1 year).*

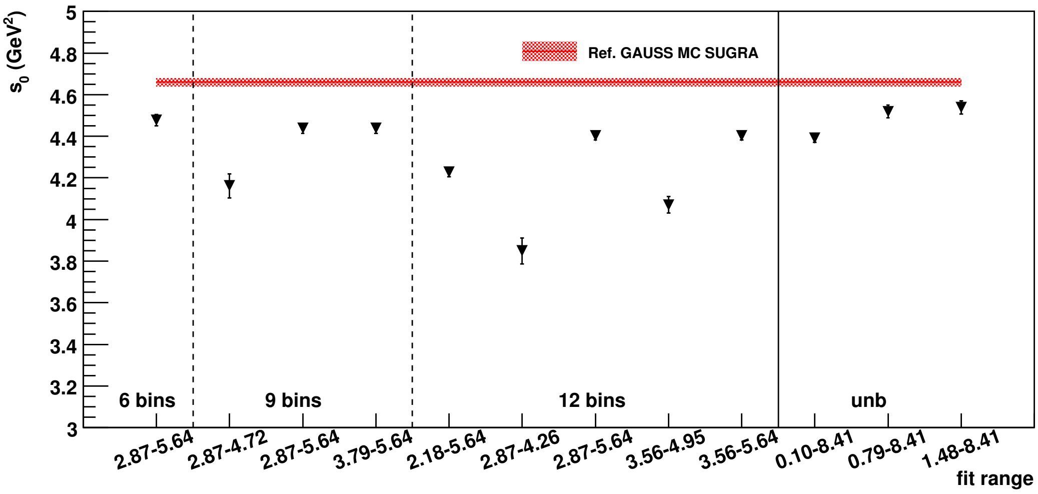

Figure 7.14: *The mean values for the zero crossing and the errors obtained by the binned fit for a different number of bins and the unbinned fit (labelled "unb") for different ranges. The events are produced with SUGRA1 parameters. The fits were performed on 211 experiments each with a sample size of 2 fb^{-1} (1 year).*

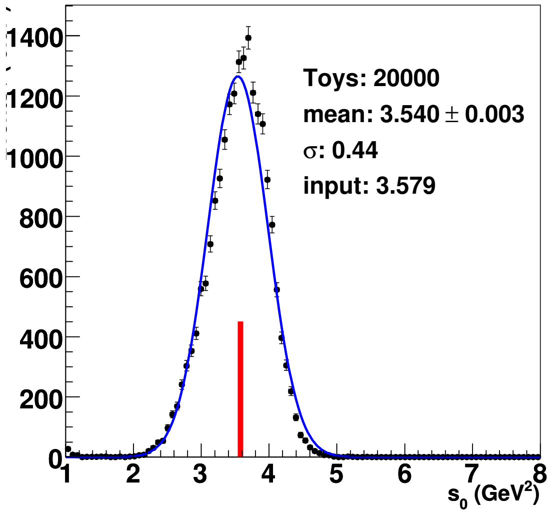

Figure 7.15: *Error on the zero crossing is determined by the width of the Gaussian. It is obtained from a distribution of 20000 toy trial A_{FB} curves. Each of the A_{FB} curves is due to a variation according to the error on a single experiment of 1 year of events from the LHCb event generator with SM parameters.*

7.4 Determination of zero crossing point error

Given one particular experiment, corresponding to a 2 fb^{-1} sample, the statistical uncertainty of the determination of s_0 is determined as follows. The zero-crossing point is determined from the A_{FB} polynomial solution. To be flexible, the order of the polynomial can be chosen to match the shape of the forward and backward s distributions. Hence a n^{th}-order polynomial solution is obtained with a numerical procedure to solve for the zero-crossing point. The parameters of the forward and backward polynomials are calculated by the likelihood maximisation in RooFit and the errors are represented by a covariance matrix. This covariance matrix is subsequently used to determine the error on the zero-crossing point.

Since the polynomial parameters are in general correlated, the covariance matrices, denoted M, must be diagonalised to obtain decorrelated errors:

$$M = EDE^{-1} = EDE^{T}, \tag{7.2}$$

where E is the matrix containing the eigenvectors of the transformation, and D is a diagonal matrix containing the decorrelated parameter errors. The second equality follows from the fact that eigenvector matrices form an orthogonal basis and are real and symmetric.

The original polynomials are transformed to the diagonal basis using the eigenvector matrix E by rewriting the parameters

$$\boldsymbol{\alpha}' = E\boldsymbol{\alpha},\ \boldsymbol{\beta}' = E\boldsymbol{\beta}, \tag{7.3}$$

where $\boldsymbol{\alpha}$ and $\boldsymbol{\beta}$ are vectors of parameters of the two polynomials.

To numerically determine the error on the zero crossing from the errors on the parameters of an asymmetry of a *single* experiment, a general Monte Carlo solution is employed. Multiple A_{FB} curves are generated by smearing the decorrelated errors on the parameters in a Gaussian way; these are the toy trial curves. The resulting curves are solved for the zero-crossing point. The distribution of zero-crossing points is subsequently fitted with a Gaussian to obtain the width of the distribution, which is taken as the error on the zero crossing point. The distribution of s_0 is displayed in Fig. 7.15. For one particular experiment of 2 fb^{-1} (1 year equivalent) of events from the LHCb event generator the fit of 20000 toy trials returned a standard deviation of the zero crossing point of $\sigma_{s_0} = 0.44\ \text{GeV}^2$. This corresponds to the error estimation of the zero crossing point for an unbinned fit based on 7200 observed events.

In the next section scenarios with background will be described.

7.5 Background Treatment

In the experiment there will be background from several sources. In the selection procedure described in [76] the background categories are listed. The categories are reproduced in Table 5.2.

Disregarding the non-resonant background source of $B^0 \to K\pi\mu\mu$ decays, a method is described here to correct for the background in the B^0-meson mass peak region from the mass sidebands. The peak region is defined as a region from 90 MeV below to 120 MeV above the B^0-meson mass (5279.5 MeV). For non-resonant background it has been assumed that the zero-crossing point is the same as for the resonant signal [76].

The event selection eliminates all but $0.008 \pm 0.002\%$ of the available dimuon background in the peak region. To study the background in the peak region, an assumption is made that the *shape* of the background is not affected by the selection[4].

The amount of background events in the complete s range has been estimated [76] to be approximately 3500 triggered events per 2 fb^{-1} neglecting non-resonant background. In the following the available background and signal samples are rescaled according to the yields, and subsequently added.

7.5.1 Effect of background

In general, adding background with no forward-backward preference by itself causes the asymmetry to be diluted. The denominator in Eq. (1.26) will increase while the numerator remains unaffected, leading to a smaller asymmetry. However, backgrounds that produce an asymmetry dependent on the invariant dimuon mass squared, s, have an influence on the shape of the forward-backward asymmetry and, possibly, the zero-crossing point.

The expectation value for the forward-backward asymmetry in the presence of preselected background (see Chapter 5) from dimuon inclusive events is shown in Fig. 7.16. The figure shows that the zero-crossing point is not significantly altered by the dimuon background.

To study different background effects, two types of background have been artificially created from the selected background events. First, a sample which is non-flat in the invariant mass s and flat in θ_l, has been added to the signal sample (background model 1). The result is shown in Fig. 7.17. As expected from Eq. (6.6), although the shape of the asymmetry is diluted, the zero crossing does not change position. Second, a sample (background model 2) was produced with an asymmetric θ_l distribution, but flat in s. The resulting background is added to the signal and the resulting forward-backward asymmetry is shown in Fig. 7.18. In accordance with the predictions from Eq. (6.6) it is observed that the zero crossing does shift due to a non-symmetric θ_l distributed background.

In the next section the correction to the A_{FB} for the background contribution will be shown, independed of the actual shape of the background distributions.

[4]This is the only assumption made to study the background correction. In the experiment it must be investigated.

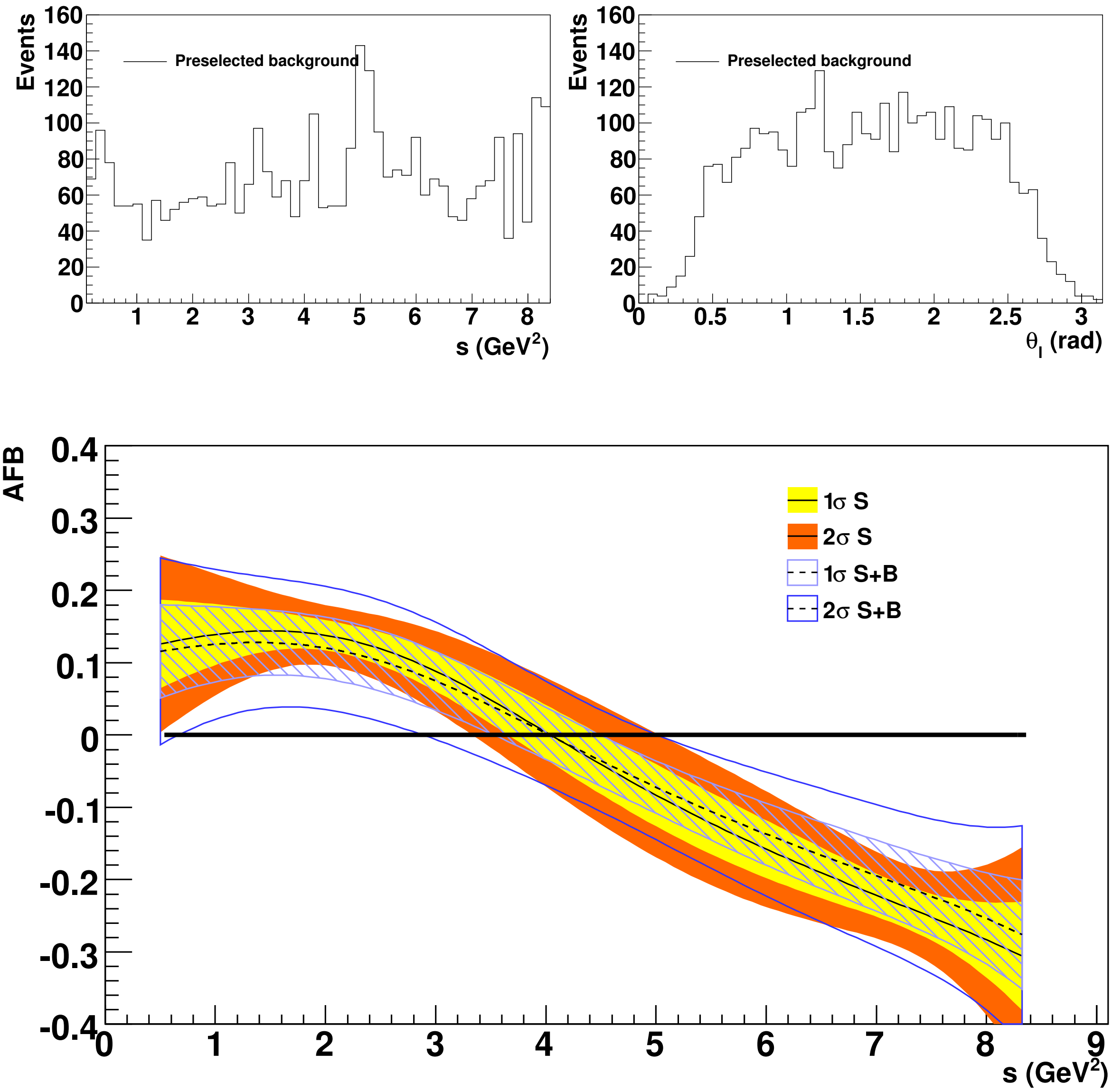

Figure 7.16: *The top pictures show the s-distribution and θ_l distribution of the preselected dimuon inclusive background from the LHCb event generator. The bottom picture shows the expectation value for 1 year of LHCb with preselected dimuon inclusive background from the LHCb event generator added. (Estimated with 12 experiments of 1 year.)*

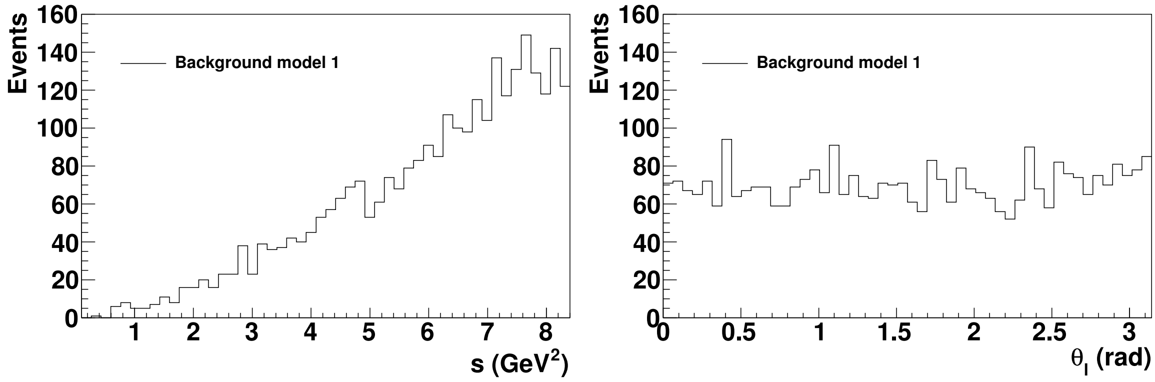

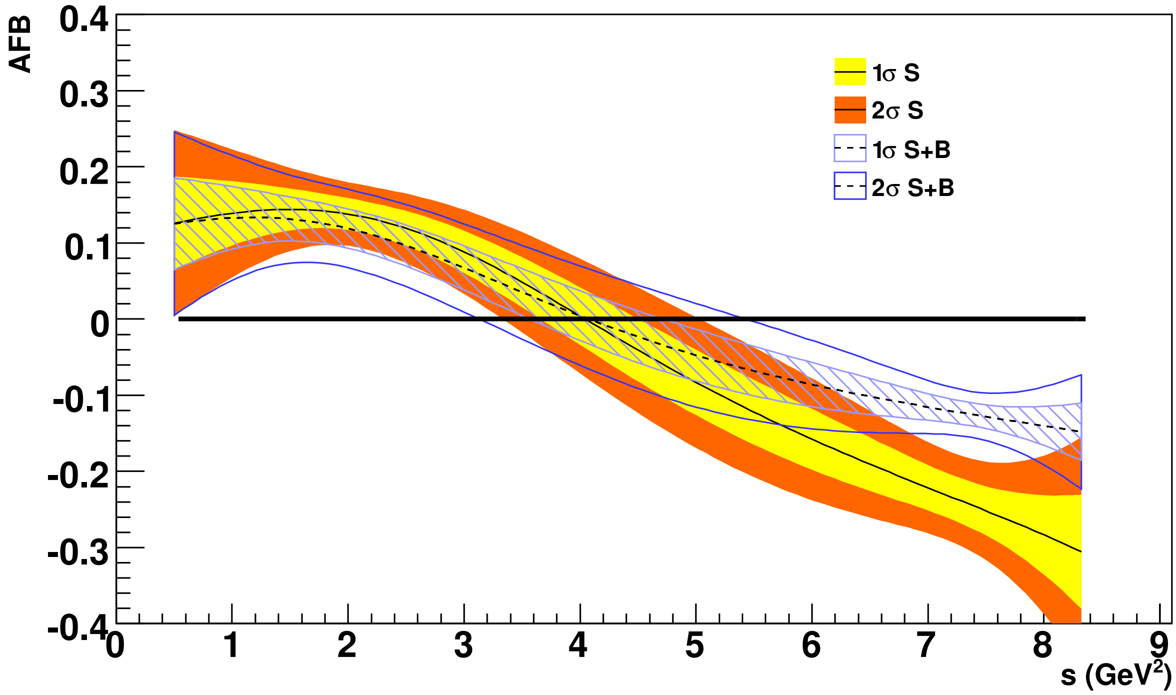

Figure 7.17: *The top pictures show the s-distribution and θ_l-distribution of the simulated background model 1. The bottom picture shows the expectation value for 1 year of LHCb with background added. (Estimated with 12 experiments of 1 year.)*

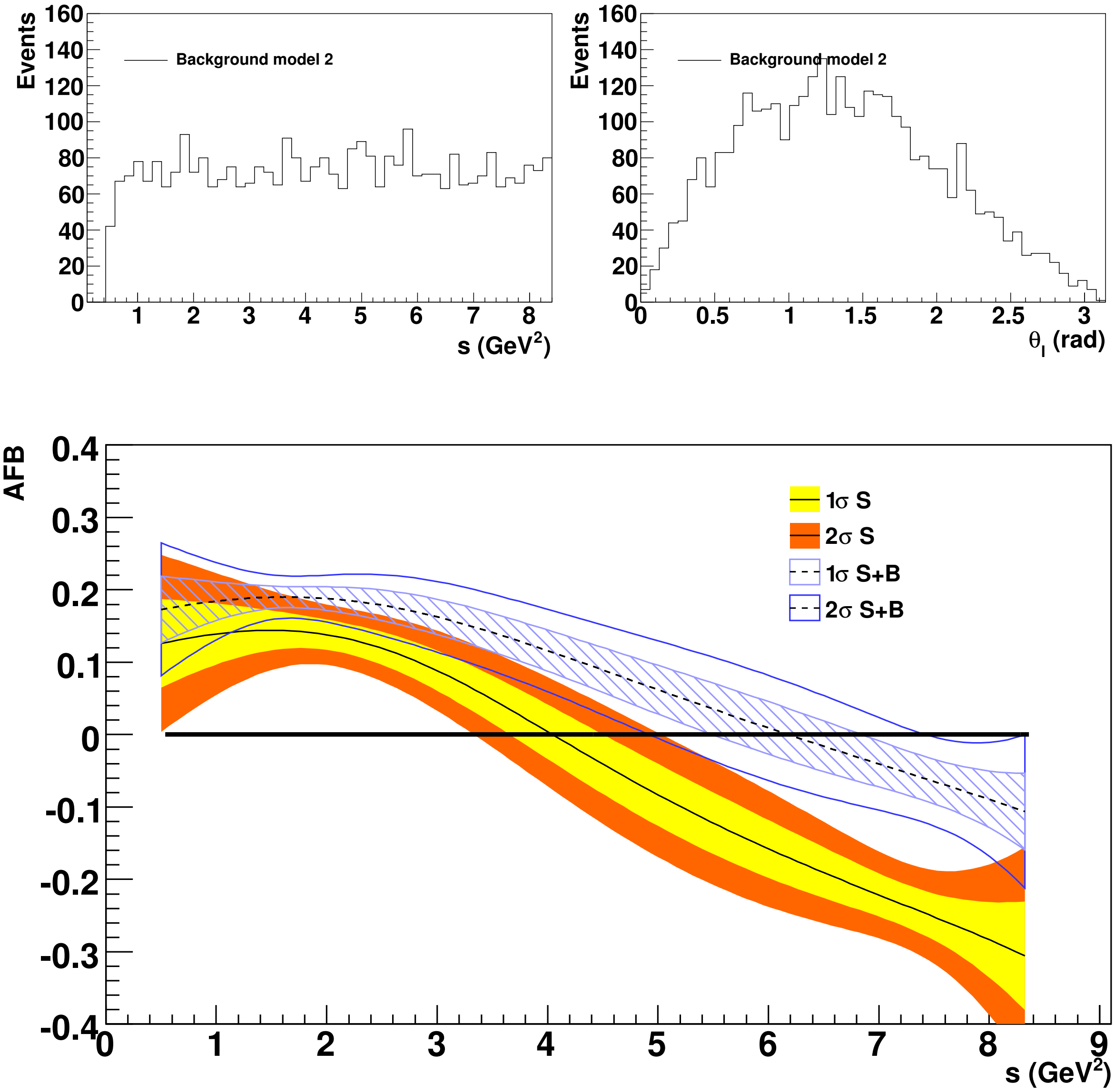

Figure 7.18: *The top pictures show the s-distribution and the θ_l-distribution of the simulated background model 2. The bottom picture shows the expectation value for 1 year of LHCb with background added. (Estimated with 12 experiments of 1 year.)*

7.5.2 Correction for background

A correction for the dimuon inclusive background in the B^0 mass peak region is applied estimating the background in the peak by using events from the sidebands. The background is modelled by a linear polynomial in the invariant mass which is observed to fit the events well. In the peak region the signal and background PDFs are added. A fit of the invariant mass distribution in the sidebands is performed as shown in Fig 7.19(a) and (d) and the background parameters are fixed. Subsequently the invariant dimuon mass squared distribution of the peak region is fitted with a 3^{rd} order Chebyshev polynomial for the signal and the fixed linear Chebyshev term obtained from the sidebands, shown in Fig 7.19(b) and (e). Due to the constraint from the background in the sidebands, the signal part of the PDF is recovered, shown in Fig 7.19(c) and (f).

A forward-backward asymmetry is subsequently created from the corrected curves in Figs. 7.19(c) and (f) and is shown in Fig. 7.20. The shape of the A_{FB} is improved by the correction. The zero-crossing point is slightly affected by this procedure, but well within one standard deviation of the expectated value.

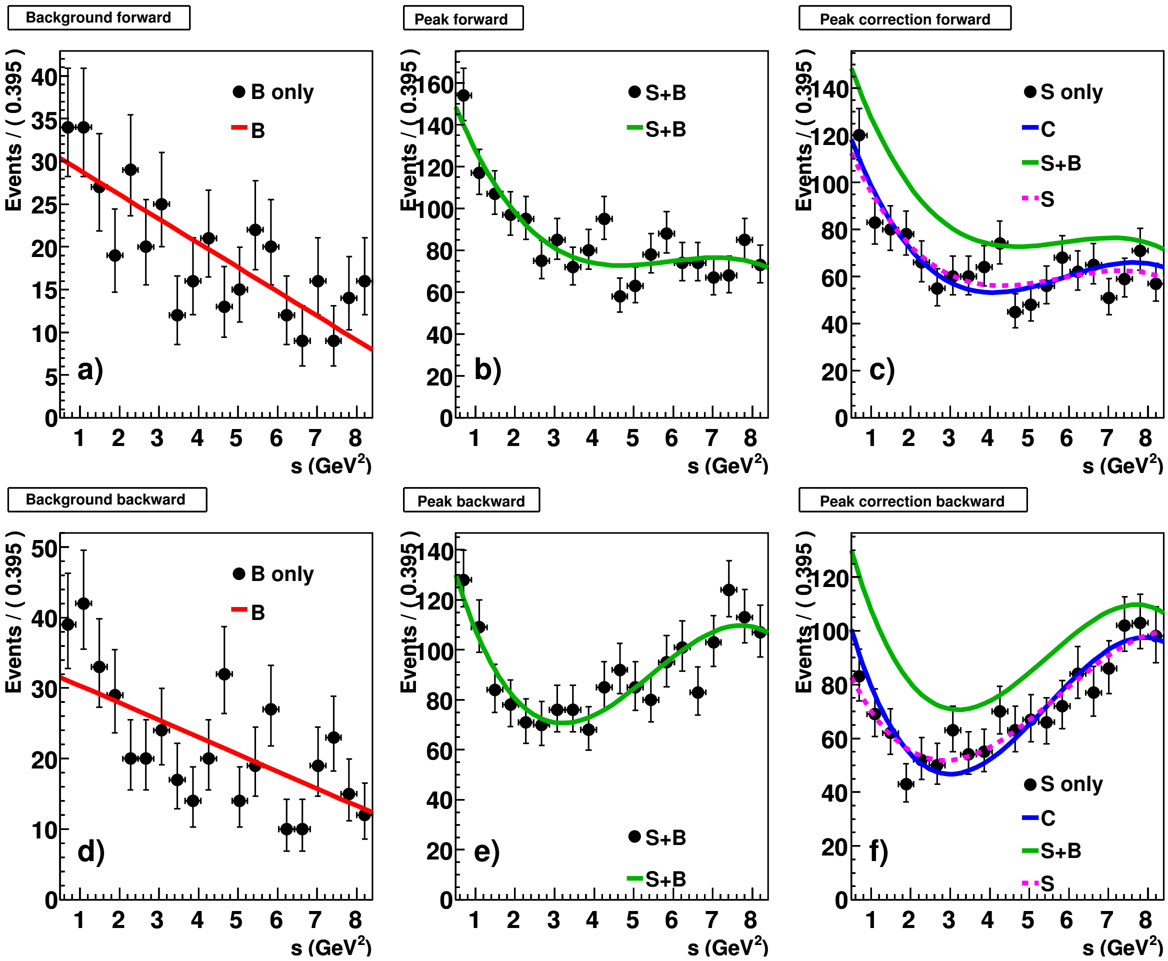

Figure 7.19: *(a) The background from the B^0 mass sidebands is used to determine the shape and size of the background in the peak region for forward events ($|\theta_l| > 0$). (b) The signal plus background ("S+B") in the peak region are fitted. (c) This enables a correction ("C") to be made which is close to the original signal data ("S"). Plots (d), (e) and (f) depict the same information for backward events.*

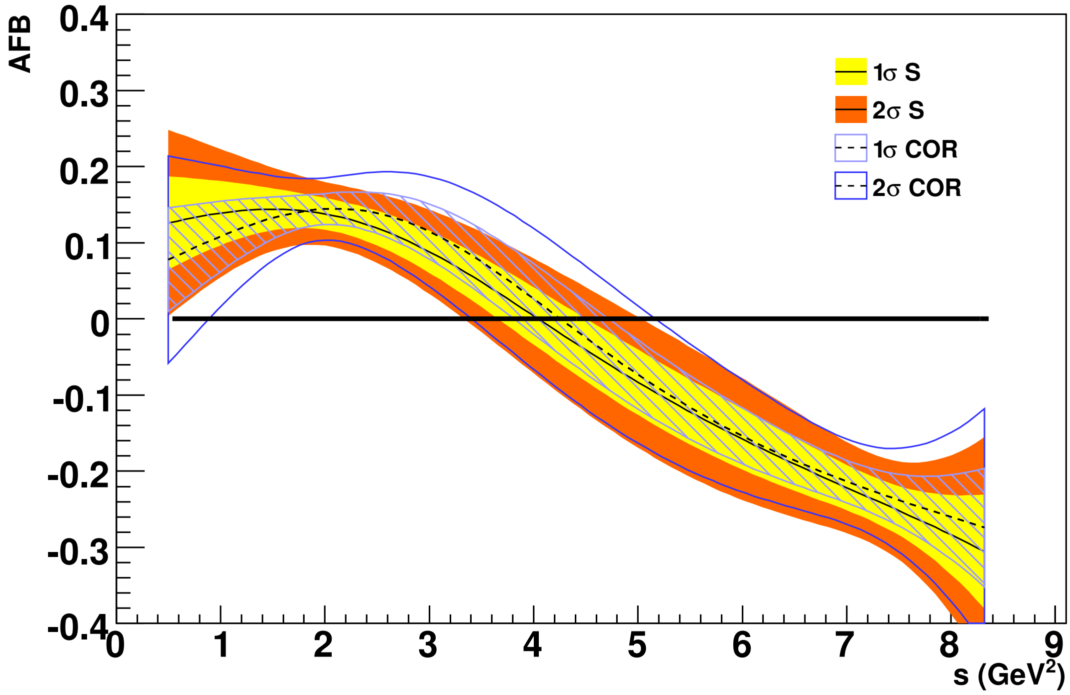

Figure 7.20: *A comparison between the original signal (solid) and after the background correction has been applied (open). (Estimated with 12 experiments of a size equivalent to 1 year nominal LHCb running.)*

7.6 Expectation for new physics models with reverse sign Wilson coefficient $C_{7\gamma}$

In the previous sections only models with a zero crossing point have been addressed. The models in which the Wilson coefficient $C_{7\gamma}$ is oppositely signed with respect to the standard model (sgn $C_{7\gamma} = -$sgn $C_{7\gamma,SM}$) display a forward-backward asymmetry that does not cross the zero for any value of s larger than zero below the resonance region. The currently available data on the asymmetry from the Belle experiment is displayed in Fig 7.21. Superimposed on this data is the standard model prediction and a prediction with a new physics model with a flipped sign $C_{7\gamma}$ coefficient. These measurements are still inconclusive with respect to the sign of $C_{7\gamma}$.

Two models from Sec. 1.7, SUSY2 and SUGRA2, have a reversed sign Wilson coefficient. The sign of the forward-backward asymmetry below the resonance regions is negative[5] for every value of the invariant dimuon mass, s. There is no zero crossing of the asymmetry.

Subsequently the potential of the unbinned method to distinguish such new physics models is examined for an equivalent amount of data of 2 fb^{-1}. The expectation in LHCb for measuring the asymmetries according to the standard model and according to the SUSY2 model are displayed in Fig. 7.22. To estimate the expectation, 20 independent samples, each of 2 fb^{-1} are used. A simulation based on the SUGRA2 model gives almost identical results.

From these simulations it is seen that LHCb will be able distinguish this model with a reverse sign Wilson coefficient $C_{7\gamma}$ after 1 year of nominal data taking.

[5]In the convention of the A_{FB} used in this thesis, Belle uses an opposite sign convention for their asymmetry.

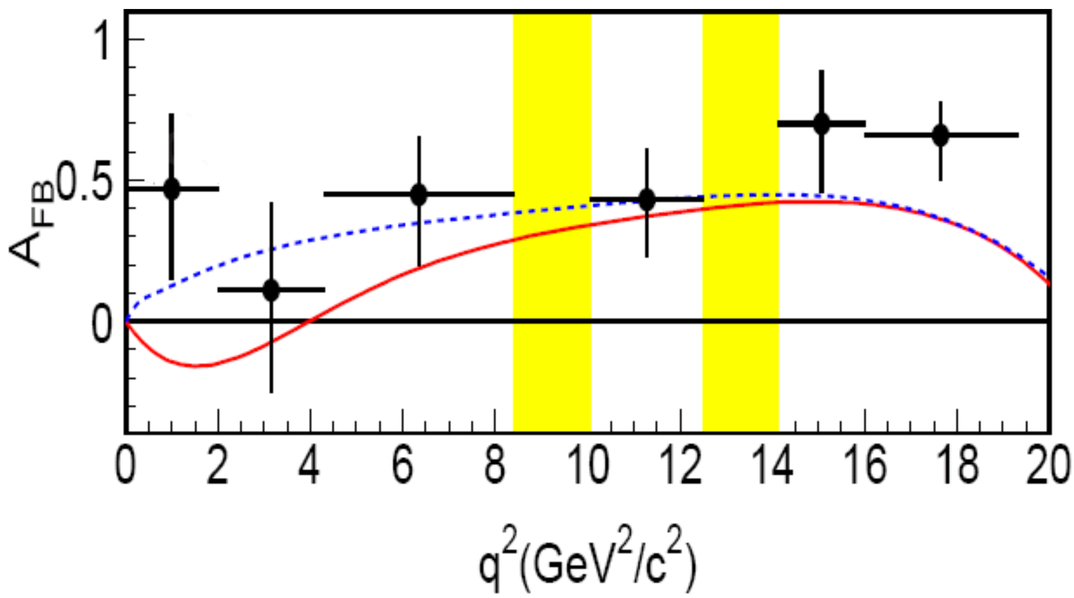

Figure 7.21: *Recent Belle measurements on the forward-backward asymmetry. Note that the definition of the asymmetry is opposite to the definition used in this thesis ($A_{FB,\,\mathrm{Belle}} = -A_{FB,\,\mathrm{LHCb}}$). The solid line represents the SM with $C_{7\gamma}$ negative ($C_{7\gamma} = -0.330$, $C_{9V} = 4.069$, $C_{10A} = -4.213$). The case where $C_{7\gamma}$ is positive ($C_{7\gamma} = 0.330$, $C_{9V} = 4.069$, $C_{10A} = -4.213$) is represented by the dotted line. The shaded regions are veto windows to reject $J/\psi(\psi')X$ events. The variable q^2 is the dimuon invariant mass squared, named s in this thesis. Figure taken from [80].*

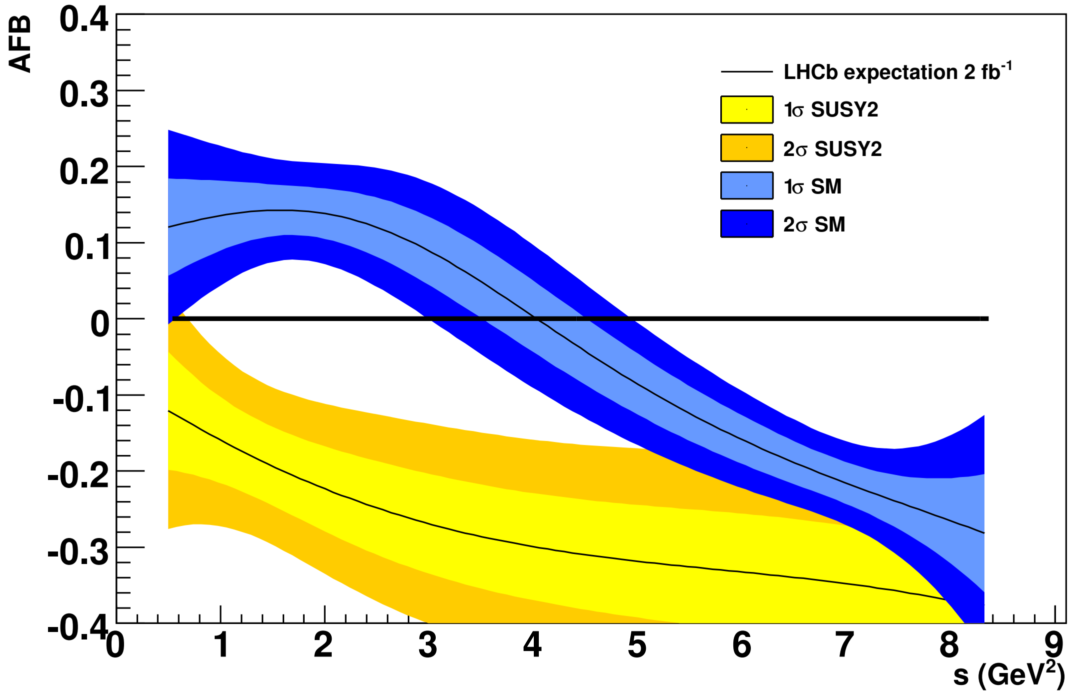

Figure 7.22: *LHCb sensitivity for A_{FB} with 1 and 2 standard deviation error bands after 1 year for the LHCb event generator with SM parameters and SUSY2 parameters data. (20 independent Monte Carlo samples of 2 fb^{-1} are used for this estimation.)*

7.7 Conclusions

Two methods of determining the forward backward asymmetry and its zero-crossing point are investigated. The first is a binned method that divides the forward backward asymmetry A_{FB} in bins of the invariant mass s. The second method was developed for this thesis and uses an unbinned fit of the invariant mass distributions of the forward and backward events separately.

The expectation value for the SM was estimated with 212 statistically independent experiments from the LHCb event generator with each 2 fb^{-1} of events. A method to determine the error on the ZCP is introduced. In addition the expected asymmetry and zero crossing point for two models with alternative Wilson coefficients (based on SUSY and SUGRA models) are investigated.

A method is described to determine the error on the zero crossing point given the uncertainties on the parameters of fitted the polynomial. The error on the zero crossing point after one nominal year of LHCb running is determined to be 0.44 GeV^2.

Subsequently the effects of several background contributions are determined. Background from a dimuon inclusive sample is added to a signal sample. From the sidebands of the B^0-meson mass distribution the shape and size of the s distribution of the background is estimated. The correction to the background results in an asymmetry that is within 1 standard deviation of the original signal.

The potential of the unbinned method to distinguish two new physics models with a reversed sign Wilson coefficient $C_{7\gamma}$ is examined.

7.8 Outlook

The unbinned technique described in this thesis is extendable in many ways. One can change the fit functions of both forward and backward distributions. In the case of polynomials the order of forward and backward functions could be allowed to differ. Other variables can be included in the fit. For example the theta distribution can also be subject to a unbinned fit[6].

As could be seen the acceptances in the decay can influence the expectation value of the asymmetry and the zero crossing. Control channels can be used to determine these acceptances, however one needs to be careful to disentangle any possible effects due to sources of new physics. Monte Carlo experiments will play a role in these studies[7].

[6] This is currently being investigated.
[7] Acceptance studies are also undergoing.

References

[1] C.S. Wu et al., *Experimental Test of Parity Conservation in Beta Decay*, Phys. Rev. **105**(4) (1957) 1413.

[2] AMS Collaboration, J. Alcaraz et al., *Search for antihelium in cosmic rays*, Phys. Lett. **B461** (1999) 387.

[3] G. Steigman, *Observational tests of antimatter cosmologies*, Annu. Rev. Astr. Ap. **14** (1976) 339.

[4] D. N. Spergel, L. Verde, H. V. Peiris, E. Komatsu, M. R. Nolta, C. L. Bennett, M. Halpern, G. Hinshaw, N. Jarosik, A. Kogut, M. Limon, S. S. Meyer, L. Page, G. S. Tucker, J. L. Weiland, E. Wollack, and E. L. Wright, *First Year Wilkinson Microwave Anisotropy Probe (WMAP) Observations: Determination of Cosmological Parameters*, The Astrophysical Journal **148** (2003) 175.

[5] S. Sarkar, *Measuring the baryon content of the universe: BBN vs CMB*, 2004.

[6] A.D. Sakharov, *Violation of CP Invariance, C Asymmetry, and Baryon Asymmetry of the Universe*, JETP Lett. **5** (1967) 24.

[7] A. Riotto and M. Trodden, *Recent Progress in Baryogenesis*, Annual Review of Nuclear and Particle Science **49** (1999) 35.

[8] N. Isgur and M.B. Wise, *Relationship between form factors in Semileptonic $\bar{B}$ and D decays and exclusive rare $\bar{B}$-meson decays*, Phys. Rev. D **42**(7) (1990) 2388.

[9] G. Burdman, *Short Distance Coefficients and the Vanishing of the Lepton Asymmetry in $B \to V\ell^+\ell^-$*, Physical Review D **57** (1998) 4254.

[10] K.G. Wilson, *Non-Lagrangian Models of Current Algebra*, Phys. Rev. **179**(5) (1969) 1499.

[11] G. Buchalla, A. J. Buras, and M. E. Lautenbacher, *Weak Decays Beyond Leading Logarithms*, Reviews of Modern Physics **68** (1996) 1125.

[12] W. Buchmüller and D. Wyler, *Effective lagrangian analysis of new interactions and flavour conservation*, Nuclear Physics B **268**(3-4) (1986) 621.

[13] A. J. Buras and R. Fleischer, *Quark mixing, CP violation and rare decays after the top quark discovery*, Heavy Flavours II, World Scientific (1997).

[14] T. Hurth, *Present Status of Inclusive Rare B Decays*, Reviews of Modern Physics **75** (2003) 1159.

[15] A. Buras and M. Münz, *Effective Hamiltonian for $B \to X_s e^+e^-$ beyond leading logarithms in the naive dimensional regularization and 't Hooft-Veltman schemes*, Phys. Rev. D **52**(1) (1995) 186.

[16] F. Krüger and E. Lunghi, *Looking for novel $CP-$violating effects in $\bar{B} \to K^* l^+ l^-$*, Phys. Rev. D **63**(1) (2000) 014013.

[17] A. Ali and G. Hiller, *A Theoretical Reappraisal of Branching Ratios and CP Asymmetries in the Decays $B \to (X_d, X_s)\ell^+\ell^-$ and Determination of the CKM Parameters*, European Physical Journal C **8** (1999) 619.

[18] C.S. Kim and Y.G. Kim and C.-D Lü and T. Morozumi, *Azimuthal angle distribution in $B \to K^*(\to K\pi)l^+l^-$ in the low invariant $m_{l^+l^-}$ region*, Phys. Rev. D **62**(3) (2000) 034013.

[19] L. Silvestrini, *Searching for New Physics in b to s Hadronic Penguin Decays*, 2007.

[20] Z. Xiao, C. Sheng Li, and K.-T. Chao, *Charm multiplicity and the branching ratios of inclusive charmless b quark decays in the general two-Higgs-doublet models*, Physical Review D **62** (2000) 094008.

[21] C. Lange and A. Ryd et al., *The EvtGen Event Generator Package Code*, in Proceedings of CHEP, 1998.

[22] U. Egede, *Angular correlations in the $\overline{B}_d \to \overline{K}^{*0}\mu^+\mu^-$ decay*, Technical Report LHCb-2007-057. CERN-LHCb-2007-057, 2007.

[23] F. Krüger and L. M. Sehgal, *Lepton polarization in the decays $B \to X_s\mu^+\mu^-$ and $B \to X_s\tau^+\tau^-$*, Physics Letters B **380**(1-2) (1996) 199.

[24] A. Ali, P. Ball, L.T. Handoko, and G. Hiller, *Comparative study of the decays $B \to (K, K^*)l^+l^-$ in the standard model and supersymmetric theories*, Phys. Rev. D **61**(7) (2000) 074024.

[25] D. Melikhov, N. Nikitin, and S. Simula, *Rare exclusive semileptonic $b \to s$ transitions in the standard model*, Phys. Rev. D **57**(11) (1998) 6814.

[26] G. Buchalla, G. Hiller, and G. Isidori, *Phenomenology of non-standard Z couplings in exclusive semileptonic $b \to s$ transitions*, Physical Review D **63** (2001) 014015.

[27] A. Ali, T. Mannel, and T. Morozumi, *Forward backward asymmetry of dilepton angular distribution in the decay $b \to sl^+l^-$*, Phys. Lett. **B273** (1991) 505.

[28] D. Liu, *Estimates for Forward-backward Asymmetry in $B \to K^*(892)l^+l^-$*, Physics Letters B **346** (1995) 355.

[29] A. Ali and A. Salim Safir, *Helicity analysis of the decays $B \to K^*\ell^+\ell^-$ and $B \to \rho\ell\nu_\ell$ in the large Energy Effective Theory*, European Physical Journal C **25** (2002) 583.

[30] E. Lunghi, *Improved Model-Independent Analysis of Semileptonic and Radiative Rare Decays*, talk given at the 10th International Conference on Supersymmetry and Unification of Fundamental Interactions, June 17-23, 2002, DESY Hamburg, 2002.

[31] D. Melikhov, N. Nikitin, and S. Simula, *Probing right-handed currents in $B \to K^*\ell^+\ell^-$ transitions*, Physics Letters B **442** (1998) 381.

[32] M. Misiak, *The $b \to se^+e^-$ and $b \to s\gamma$ decays with next-to-leading logarithmic QCD corrections*, Nucl. Phys. **B393** (1993) 23.

[33] M. Beneke, T. Feldmann, and D. Seidel, *Systematic approach to exclusive $B \to Vl^+l^-, V\gamma$ decays*, Nuclear Physics B **612** (2001) 25.

[34] T. Goto, Y. Okada, and Y. Shimizu, *Flavor changing neutral current processes in B and K decays in the supergravity model*, Phys. Rev. D **58**(9) (1998) 094006.

[35] T. Goto, Y. Okada, Y. Shimizu, and M. Tanaka, *$b \to sll$ in the minimal supergravity model*, Phys. Rev. D **55**(7) (1997) 4273.

[36] LHCb Collaboration, S. Amato et al., *LHCb technical proposal*, CERN-LHCC-98-04.

[37] L. Evans and S. Meyers eds., *LHC Design Report - The LHC Machine - Introduction*, CERN, 2004.

[38] P. Nason et al., *Bottom Production*, 1999 CERN Workshop on SM physics (and more) at the LHC (2000) .

[39] N. Tuning, *Private Communication.*

[40] CDF Collaboration, A. Abulencia et al., *Measurement of the $B_s^0 - \bar{B}_s^0$ Oscillation Frequency*, Physical Review Letters **97**(6) (2006) 062003.

[41] LHCb Collaboration, R. Antunes-Nobrega et al., *LHCb reoptimized detector design and performanceTechnical Design Report*, Technical Design Report LHCb. CERN, Geneva, 2003.

[42] LHCb Collaboration, P.R. Barbosa-Marinho et al., *LHCb VELO (VErtex LOcator) Technical Design Report*, Technical Design Report LHCb. CERN, Geneva, 2001.

[43] E.A. Papadelis, *Characterisation and commissioning of the LHCb VELO detector*, Ph.D. thesis, Vrije Universiteit Amsterdam, 2009.

[44] LHCb Collaboration, S. Amato et al., *LHCb magnet Technical Design Report*, Technical Design Report LHCb. CERN, Geneva, 1999.

[45] LHCb Collaboration, P.R. Barbosa-Marinho et al., *LHCb inner tracker Technical Design Report*, Technical Design Report LHCb. CERN, Geneva, 2002.

[46] G.W van Apeldoorn et al., *Beam Tests of Final Modules and Electronics of the LHCb Outer Tracker in 2005*, Technical Report LHCb-2005-076. CERN-LHCb-2005-076, 2005.

[47] T. Ruf, *Subdetector Occupancies for DC06*, LHCb reconstruction web page, 2006.

[48] LHCb Collaboration, P.R. Barbosa-Marinho et al., *LHCb outer tracker Technical Design Report*, Technical Design Report LHCb. CERN, Geneva, 2001.

[49] LHCb Collaboration, S. Amato et al., *LHCb RICH Technical Design Report*, Technical Design Report LHCb. CERN, Geneva, 2000.

[50] S. Barsuk, I. Belyaev, A. Goloutvin, and I. Korolko, *Optimization of cell sizes of electromagnetic calorimeter*, Technical Report LHCb-99-034, 1999.

[51] LHCb Collaboration, S. Amato et al., *LHCb calorimeters Technical Design Report*, Technical Design Report LHCb. CERN, Geneva, 2000.

[52] LHCb Collaboration, P.R. Barbosa-Marinho et al., *LHCb muon system Technical Design Report*, Technical Design Report LHCb. CERN, Geneva, 2001.

[53] LHCb Collaboration, *Addendum to the Muon Technical Design Report*, CERN-LHCC-2003-002. 2003.

[54] LHCb collaboration, *Second Addendum to the Muon Technical Design Report*, CERN-LHCC-2005-0012.

[55] LHCb Collaboration, P.R. Barbosa-Marinho et al., *LHCb online system, data acquisition and experiment control Technical Design Report*, Technical Design Report LHCb. CERN, Geneva, 2001.

[56] E. Rodrigues, *The LHCb Trigger System*, Nucl. Phys. B, Proc. Suppl. **170** (2007) 298.

[57] LHCb Collaboration, R. Antunes-Nobrega et al., *LHCb trigger system Technical Design Report*, Technical Design Report LHCb. CERN, Geneva, 2003.

[58] J. A. Hernando, *The LHCb Trigger*, Acta Physica Polonica B **38** (2007) 941.

[59] G. Raven, *HLT Lines TWiki pages*, CERN LHCb Twiki, 2009.

[60] LHCb Collaboration, R. Antunes-Nobrega et al., *LHCb computing Technical Design Report*, Technical Design Report LHCb. CERN, Geneva, 2005.

[61] T. Sjöstrand and S. Mrenna and P. Skands, *PYTHIA 6.4 physics and manual*, JHEP **05** (2006) 026.

[62] H.P. Wellisch, M. Maire, and L. Urban, *Geant4 Physics Reference Manual*, 2004.

[63] R.E. Kalman, *A New Approach to Linear Filtering and Prediction Problems*, Transactions of the ASME–Journal of Basic Engineering **82**(Series D) (1960) 35.

[64] B. Hommels, *The tracker in the trigger of LHCb*, Ph.D. thesis, Universiteit van Amsterdam, 2006.

[65] R. Mankel, *Pattern recognition and event reconstruction in particle physics experiments*, Rept. Prog. Phys. **67** (2004) 553.

[66] R.W. Forty and M. Needham, *Standalone Track Reconstruction in the T-stations*, Technical Report LHCb-2007-022. CERN-LHCb-2007-022, 2007.

[67] M. Needham, *The Tsa Reconstruction Framework*, Technical Report LHCb-2007-037. CERN-LHCb-2007-037, 2007.

[68] R.W. Forty, *Track Seeding*, Technical Report LHCb-2001-109, 2001.

[69] R. Forty, *A Seeding Algorithm for LHCb*, Fortran code in the LHCb software repository.

[70] R. van der Eijk, *Track reconstruction in the LHCb experiment*, Ph.D. thesis, Universiteit van Amsterdam, 2002.

[71] M. Needham, *Combined Long Tracking Performance*, Technical Report LHCb-2007-019. CERN-LHCb-2007-019, 2007.

[72] P. Koppenburg, *Contribution to the Development of the LHCb Vertex Locator and Study of Rare Semileptonic Decays*, Ph.D. thesis, Université de Lausanne, 2002.

[73] J.M. Dickens, *A Study of the RICH Detector Performance and Search for New Physics in $B \to K^*\mu^+\mu^-$ Decays with the LHCb Experiment*, Ph.D. thesis, University of Cambridge, 2008.

[74] T. Blake, *Ring Imaging Cherenkov Detectors and the Rare Decay $B \to K^*\mu^+\mu^-$ at LHCb*, Ph.D. thesis, Imperial college, London, 2008.

[75] A. K. Alok, A. Dighe, and S. Uma Sankar, *Large forward-backward asymmetry in $B \to K\mu^+\mu^-$ from new physics tensor operators*, Physical Review D **78** (2008) 114025.

[76] J. Dickens et al., *Selection of the decay $B_d \to K^*\mu^+\mu^-$ at LHCb*, CERN-LHCB-2007-038.

[77] Particle Data Group Collaboration, W.-M. Yao et al., *Review of particle physics*, J. Phys. **G33** (2006) 1.

[78] B. Grinstein and D. Pirjol, *The forward-backward asymmetry in $B \to K\pi\ell^+\ell^-$ decays*, Phys. Rev. **D73** (2006) 094027.

[79] W. Verkerke and D. Kirkby, *The RooFit toolkit for data modeling*, Talk from the 2003 Computing in High Energy and Nuclear Physics (CHEP03), La Jolla, Ca, USA, March 2003, 2003.

[80] Belle Collaboration, J.-T. Wei et al., *Measurement of the Differential Branching Fraction and Forward-Backward Asymmetry for $B \to K^{(*)}l^+l^-$*, Physical Review Letters **103**(17) (2009) 171801.

Summary

This thesis "Asymmetries in the decay of beauty" describes two main subjects for the LHCb experiment at the LHC accelerator. The first topic is a track pattern recognition algorithm for the tracking stations of the LHCb spectrometer. The second topic is an unbinned counting analysis of the muonic forward-backward asymmetry in the flavour changing neutral decay $B^0 \to K^*\mu^+\mu^-$. During the research use has been made of Monte Carlo events because the experiment and the accelerator were not yet operational.

The pattern recognition algorithm for the tracking stations that is described delivers tracks from an input of hits from the tracker stations (T stations) of LHCb. The algorithm is based on a global track finding approach, where hits in outer layers are interpolated to find more hits that belong together. The algorithm makes use of the residual magnetic field in the T stations to calculate a momentum estimate from the curvature. The quality of the tracks is calculated with a likelihood routine based on track prediction and actual hit position. The quality of the tracks, and hence the performance of the algorithm is tested against known Monte Carlo information. The ratio of correctly found MC particles to total MC particles available (*efficiency*) was found to be 85% while the ratio of wrongly reconstructed tracks to the total number of reconstructed tracks (*ghostrate*) was found to be 15% for a particular optimal tuning. Furthermore the momentum dependence of the efficiency and ghostrate were investigated as were the track parameters. With the tracks also a momentum resolution dependence on the reconstructed momentum was investigated. From the corrected distributions a multiple scattering term for the resolution can be extracted of $1.8\ 10^{-2}$. Also a co-ordinate resolution term is extracted of $6.8\ 10^{-4}\ \mathrm{GeV}^{-1}$.

The analysis of the flavour changeing neutral decays $B^0 \to K^*\mu^+\mu^-$ is treated in the second part. In this decay the muons have an angular distribution which is sensitive to effects of possible new physics. The positively charged muon in this decay has a polar angle that is either in a direction forward or backward with respect to the K^* direction in the rest frame of the B^0. The amount of forward or backward going muons depends on the dimuon mass, and as such an asymmetry of the amount of forward and backward traveling muons as a function of the dimuon invariant mass can be made. The invariant mass at which this asymmetry vanishes, is sensitive to new couplings.

Potential systematic effects are investigated for an event selection for $B^0 \to K^*\mu^+\mu^-$ for signal events. The effects on the forward-backward asymmetry and its zero-crossing are minimal for the given selection procedures. The combined restrictions on the muons have the largest influence on the shapes of the distributions of the invariant dimuon

mass s and the muon polar angle θ_l.

The selection effects for background events show that there is no preference for events with either forward or backward going muons. This will not cause any artificial effect in the zero-crossing of the forward-backward asymmetry.

The distributions of the invariant dimuon mass, s for the dimuon inclusive background shows a similar shape in the sideband regions and the peak region of the B^0 mass distribution. The shape of the distribution in the B^0 mass sidebands can therefore be used to estimate the shape and number of the background events in the peak region. The same holds for the distribution of the polar angle θ_l. This is exploited when the background fraction in the peak region is determined by interpolation.

An unbinned method for determining the asymmetry uses an unbinned polynomial fit of the invariant mass distributions of the forward and backward events separately. Subsequently the two fitted polynomials are subtracted and normalised to obtain an asymmetry. The zero crossing of the polynomial is obtained by using a Monte Carlo solution in which the error on the fit is propagated to the zero crossing by realising many curves with parameters that are smeared according to the decorrelated parameter errors.

The expectation value of the asymmetry for the SM is estimated with a Monte Carlo sample corresponding to an integrated luminosity of 2 fb^{-1}. In addition the expectation value for the zero crossing is estimated. The error on the zero crossing point after one nominal year of LHCb running is determined to be 0.44 GeV^2.

The effects of several background contributions are determined. Two artificially created types of background are added: First a background sample flat in the polar angle of the muon, θ_l and non-flat in invariant dimuon mass squared s do not alter the zero-crossing point, however the shape of the A_{FB} is changed. Second a background sample asymmetric in the angle θ_l and flat in the dimuon mass squared is added, and both the shape and the position of the zero-crossing point are changed.

Background events from a dimuon inclusive sample is added to a signal sample. From the sidebands of the B^0-meson mass distribution the shape and size of the s distribution of the background is estimated. The background contribution is subsequently fixed while fitting the signal plus background in the B^0-mass peak region. As a result the signal contribution of the s distribution is recovered and a correction of the background is made. The correction to the background results in an asymmetry which is within 1 standard deviation of the original signal.

The potential of the unbinned method to distinguish asymmetries from the SM and two new physics models with a reversed sign Wilson coefficient C_7 is examined. With the unbinned method it is possible to distinguish two new physics models from the standard model in the low invariant dimuon mass regions.

Samenvatting

Dit proefschrift getiteld “Asymmetrieën in het verval van schoonheid” beschrijft twee onderwerpen voor het LHCb experiment aan de LHC versneller. Het eerste onderwerp is een patroonherkennings-algoritme voor sporen in de 'T stations' in de LCHb spectrometer. Het tweede onderwerp is een ongebinde telanalyse van de muonische voorwaartse-achterwaartse asymmetrie in het smaakveranderende neutrale verval $B^0 \to K^*\mu^+\mu^-$. Tijdens het onderzoek werd er gebruik gemaakt van Monte Carlo gebeurtenissen omdat het experiment en de versneller nog niet operationeel waren.

Het patroonherkennings algoritme voor de 'T stations' dat wordt beschreven, levert sporen vanuit een verzameling van signalen in de 'T stations' in het LHCb experiment. Het algoritme is gebaseerd op een globale manier van het vinden van sporen, waarbij signalen in de buitenste lagen worden geïnterpoleerd om meer samenhangende signalen te vinden. Het algoritme maakt gebruik van het residuele magneetveld in de T stations om een schatting van de impuls te maken van de buiging. De kwaliteit van de sporen wordt berekend met een waarschijnlijkheids routine die is gebaseerd op het voorspellen van de positie van de sporen en de werkelijke signaalposities. De kwaliteit van de sporen, en zo de performance van het algoritme is getest tegen bekende Monte Carlo informatie. De verhouding van correct gevonden MC deeltjes en totale hoeveelheid MC deeltjes (*efficiëntie*) die werd gevonden was 85%, en het aantal foutief gevonden sporen in verhouding met het totale aantal gerecontrueerde sporen (*ghostrate*) was 15% voor een bepaalde optimale instelling. Verder werd de impulsafhankelijkheid van deze grootheden onderzocht samen met de parameters van de sporen. Ook werd de impulsresolutie van de sporen onderzoecht als functie van de impuls. Van de gereconstrueerde sporenwerd er een meervoudige verstrooiingsterm voor de resolutie gevonden van $1.8\ 10^{-2}$. Ook werd een coördinaatresolutieterm gevonden van $6.8\ 10^{-4}\ \text{GeV}^{-1}$.

De analyse van het smaakveranderende neutrale verval $B^0 \to K^*\mu^+\mu^-$ is beschreven in het tweede deel. In dit verval hebben de muonen een hoekverdeling die gevoelig is voor effecten van mogelijke nieuwe fysica. De positief geladen muonen hebben een polaire hoek die ofwel in een voorwaarste of achterwaartse richting ligt ten opzichte van de richting van de K^*, gezien vanuit het ruststelsel van de B^0. De hoeveelheid van de voorwaarts of achterwaarts gaande muonen hangt af van de invariante massa van het dimuonsysteem, en zodoende kan een asymmetrie van de hoeveelheid voorwaarts en achterwaarts gaande muonen als functie van de invariante dimuonmassa worden gemaakt. De invariante massa waarbij deze asymmetrie verdwijnt, is gevoelig voor nieuwe koppelingen.

Potentiële systematische effecten werden onderzocht voor een selectie van detector gebeurtenissen ('events'). Deze effecten op de voorwaarts-achterwaartse asymmetrie en haar nulpuntsdoorgang zijn minimaal voor de gegeven selectieprocedures. De gecombineerde restricties op de muonen hebben de grootste invloed op de vormen van de verdelingen van de invariante dimuonmassa s en de muonische poolhoek θ_l.

De effecten van de selectie op de achtergrond gebeurtenissen laten zien dat er geen voorkeur voor gebeurtenissen met een voorwaarts of achterwaarts muon bestaat. Dit zal geen kunstmatig effect veroorzaken in de nulpuntsdoorgang van de voorwaartse-achterwaartse asymmetrie.

De distrubuties van de invariante dimuon massa, s voor een achtergrond van inclusieve dimuonen, laat zien dat de vorm van de achtergrond gelijk is in de zijbanden van de B^0 massa verdeling en de achtergrond onder de massa piek. De vorm van de verdeling kan daarom gebruikt worden om een schatting te maken van de vorm en aantallen achtergrondgebeurtenissen op de plek van de B^0 piek. Hetzelfde geldt voor de verdeling van de poolhoek θ_l. Dit gegeven wordt gebruikt om de achtergrondfractie in de piek af te schatten door interpolatie.

Een ongebinde methode om de asymmetrie te bepalen maakt gebruikt van een ongebinde polynomische fit van de invariante massa distributies voor de voorwaartse en achterwaartse gebeurtenissen apart. Voorts worden de twee polynomen van elkaar afgetrokken en genormaliseerd om de asymmetry te verkrijgen. De nulpuntsdoorgang van de polynoom word verkregen door gebruik te maken van een Monte Carlo oplossing waarbij de fouten op de fit worden doorgerekend naar de nulpuntsdoorgang door vele curves te maken met parameters welke gevariëerd worden op basis van de gedecorreleerde founten op de fit parameters.

De verwachtingswaarde van de asymmetrie voor het Standaard Model (SM) werd afgeschat met een monster Monte Carlo gebeurtenissen dat overeenkomt met een geïntegreerde lumunositeit van 2 fb^{-1}. Als bijkomstigheid werd de verwachtingswaarde voor de nulpuntsdoorgang afgeschat. De fout op de nulpuntsdoorgang na het vergaren van gebeurtenissen in een nominaal jaar van LHCb werd bepaald op 0.44 GeV^2.

De effecten van verschillende soorten achtergrond contributies werden ook bepaald. Twee kunstmatig gemaakte types achtergrond werden toegevoegd: Ten eerste een monster achtergrondgebeurtenissen met een vlakke verdeling in de poolhoek θ_l van het muon en niet vlak in de verdeling van de gekwadrateerde invariante dimuonmassa, s, zal geen verandering geven in de nulpuntsdoorgang van de asymmetrie, echter de vorm van de asymmetrie verandert wel. Ten tweede een monster achtergrondgebeurtenissen met een asymmetrische verdeling in de poolhoek θ_l en een vlakke verdeling in de gekwadrateerde invariante dimuonmassa, waarbij zowel de vorm als de positie van de nulpuntsdoorgang veranderen.

Achtergrondgebeurtenissen van een monster inclusieve dimuonen werden toegevoegd aan de signaalgebeurtenissen. Van de zijbanden van de B^0 massa verdeling werden de vorm als het aantal gebeurtenissen van de achtergrond afgeschat. De bijdrage van de achtergrond werd vervolgens gefixeerd terwijl er een fit werd gemaakt van de de signaal plus de achtergrond in de B^0 piek. Het resultaat hiervan werd de signaal bijdrage in de piek teruggevonden en werd er een correctie van de achtergrond gemaakt. De correctie op de achtergrond resulteert in een asymmetrie welke binnen 1 standaard deviatie van het originele signaal ligt.

Het potentiëel van de ongebinde methode om een onderscheid te maken tussen asymmetrieën in het standaard model en twee nieuwe fysica modellen werd onderzocht. Met de ongebinde methode blijkt het mogelijk te zijn de modellen van het standaard model te onderscheiden in regionen met lage waarden van de invariante dimuon massa.

Epilogue

“Tutto sommato, la felicità è una picola cosa.” All things considered, happiness is something small, wrote Trilussa. This thesis is neither small, nor does it contain happiness, and it shouldn't. The happiness, however, is captured between the sentences and the chapters, within the days and evenings that have been spent with friends and colleagues. This last part is for them and about them. It is a small journey through time and thoughts along known and less well known things and along, mainly, happy events.

The week on Sardegna was for me the origin of the bfys group-spirit. With Jacopo, Peter, Bart, Antonio and Niels. On San Pietro where Antonio dove to find sea urchins and let us taste them; Where he introduced us to what would become the group greeting (vaff...); Where Bart ate fish, and Peter confessed to eat his favourite spaghetti with ketchup, something Antonio could not believe. In a small shop in Pula where I tasted the best ice cream in the world. I remember the cannonau served during dinners, the malloreddus with bottarga and the Mirto as digestif.

The period at CERN with “my” first postdoc Eduardo was exciting. Eddy, muitos agradecimentos pelo apoio. Besides a period of hard work, I will remember it as a fun time with sunny weekends in the parks and boulevards on Rive droite. In the spare time the walks in the Jura and surroundings were a nice change from the office and computer. The tracking workshops in Paris and Glasgow were instructive as well as a good opportunity to get to know people better.

Eenmaal terug in Amsterdam waren er de vele nieuwe collega's die we kregen. Zo gaat dat in het leven van een promovendus, jonge promovendi komen en oude gaan. Andreas, es war Mir ein vergnügen, die Weltmeisterschaft, der Tiefschnee im März, das Fahrrad! Tristan (“mijn favoriete office-mate”), veel succes met schrijven. Ik zal je verhalen missen die je vertelde in geuren en kleuren. Besma, je gaat een groter avontuur tegemoet, veel plezier! Hella bedankt voor de schouderklopjes, het heeft geholpen! Van VU tot VU, met wegen over WW. Bedankt voor het prettige gezelschap. Het was altijd erg gezellig in 't kantoor, bijvoorbeeld met Pasen.

Eduard, la tua Jag ha salvarsi fino ad Italia! Grazie per i viaggi che abbiamo fatto con Dorothea, Ernesta e tutti gli altri. Un ringraziamento enorme per tutto il sostegno! Salutami le tue amichette in Amsterdam ed Utrecht and I kill you more! Ci vediamo a CERN, sono certo. Aras, finishing a thesis is maybe the most work. I remember the nice discussions we had during the evenings at Nikhef. Skål and good luck with the family! Jacopo e Maaike, il vostro matrimonio a Castro era meraviglioso. The sacred brotherhood survived the trip from Napoli to Castro in one piece, although through some ruins.

Nel periodo in cui stavo lavorando alla mia analisi ho conoscuito Nicola, il “mio” secondo postdoc. Le molte serate di lavoro e spesso anche nel weekend in cui abbiamo mangiato le ‘pizze Olandese’, (piuttosto bislacche, direi). Eet smakelijk, Nicola! Il tuo entusiasmo è contagioso. Vorrei ringraziarti di cuore per tutto! Il tuo matrimonio in Sardegna era meraviglioso! Mi ho piaciuto molto di rivedere l’isola e suoi abitanti. C’è un grande piacere per averti nella mia commissione della tesi.

Circa nello stesso periodo Barbara veniva a Nikhef. Barbara, mi ricordo “la cena natale” ad Amsterdam con te e Sam. Il vostro matrimonio a Locate Varesino e Tradate mi ho fatto più impressione di quello che pensavo. Auguro a te, Sam e Justine uno splendido futuro. Grazie per il tuo ottimismo e per i ’cuori sotto la cintura’ nei miei tempi duri. Non perdere i ricordi (per i tuoi nipoti) come hai fatto con le chiavi.

Fabian, de discussies over HQET en OPE met jou waren erg leerzaam. Bovendien de Kstermumu discussies met jou, Niels en Nicola, waren buiten interessant ook erg leuk. Bedankt voor al de borrels, en succes met je proefschrift Faab! Jan Amoraal, zonder jou zouden de vrijdagen er anders uit hebben gezien; Dankie vir al die bier!

Jo, jij gaf me de kans om een promotie onderzoek te starten, bedankt voor het vertrouwen dat je me gaf. Henk Jan bedankt voor de vele ’coding-hours’. Marcel en Niels bedankt voor de kritische blikken die jullie geworpen hebben, zeker tijdens de periodes dat ik er een beetje doorheen zat. Marcel jij bent de beste “baas” die zich iemand kan wensen. Ik denk dat de bfys groep op ’t Nikhef echt een zeer speciale groep was, is en zal zijn, niet in de minste plaats door jouw manier van leidinggeven. Ik zal de bijzondere sfeer missen. Het doet mij genoegen jou als mijn promotor te mogen noemen. Niels, het was een plezier met je samen te werken, en ik ben blij je in de commissie te hebben. Ik zal met vreugde terugdenken aan grote hoeveelheden pasta die we zo nu en dan op het Nikhef bestelden en de lunches in het visrestaurant!

A warm hi to the people who do astronomy with a neutrino telescope and abyss environmental research and specially Gordon: Je bent er bijna man, maak dat proefschrift af en ga lekker naar California!

L’ultimo periodo della tesi era un periodo di scrivere, leggere, e scrivere. Però, non c’era sempre. Chiara, Giada, Serena grazie per i bei tempi che abbiamo avuto. Chiara (dobbiamo iniziare ancora una religione), sai che Jackie è sempre benvenuto. Mi piacevano le parole del giorno, hanno aiutate! (e grazie per Trilussa.) Carina Giada, sarò sempre Vale. Era molto divertente a Maastricht (’hoi hoi’) e non scorderò mai la pasquetta bellissima e il ferragosto con voi ad Amsterdam. Vorrei visitarti, passerò a Bologna o California(!) un giorno. Grazie per le correzioni della lingua, e credo ci sarà un giorno che parlerò senza vergogna. Sere, mi manchi il tuo suonando del pianoforte (Allevi) nelle serate ad astronomia. Mi ricordi la scoperta a ’De Melkweg’! De keukenhof era belissima. Grazie per l’aiuto in St. Genis, sai che yoyo non è completamente pazza ;). Gusta, Sere e Giada: Forza “the italian gang”. (e nun c’ne fott’ cchiù na minca i ppipponi). Non vi dimenticarò mai, vi voglio tanto bene! Mi mancherete tutti voi incredibile, spero a presto, dovunque, quandunque. Ik zal jullie allemaal vreselijk missen, hopelijk tot snel, ergens, ooit.